

**MODELING AND SIMULATION OF
CIRCULATING TUMOR CELLS IN FLOW**

**Part I - Low-dimensional deformation models for
circulating tumor cells in flow**

Part II - Procoagulant circulating tumor cells in flow

by

Angela Meeyoun Lee

A Dissertation Presented to the
FACULTY OF THE USC GRADUATE SCHOOL
UNIVERSITY OF SOUTHERN CALIFORNIA
In Partial Fulfillment of the
Requirements of the Degree
DOCTOR OF PHILOSOPHY
(AEROSPACE ENGINEERING)

May 16, 2014

ProQuest Number: 10799148

All rights reserved

INFORMATION TO ALL USERS

The quality of this reproduction is dependent upon the quality of the copy submitted.

In the unlikely event that the author did not send a complete manuscript and there are missing pages, these will be noted. Also, if material had to be removed, a note will indicate the deletion.



ProQuest 10799148

Published by ProQuest LLC (2018). Copyright of the Dissertation is held by the Author.

All rights reserved.

This work is protected against unauthorized copying under Title 17, United States Code
Microform Edition © ProQuest LLC.

ProQuest LLC.
789 East Eisenhower Parkway
P.O. Box 1346
Ann Arbor, MI 48106 – 1346

Dedication

*To my sons Elliott and Brandon,
for being my greatest sources of inspiration.*

Acknowledgements

The accomplishment of this dissertation would not have been possible without a whole host of people who have contributed to its completion in many ways. First, I would like to thank my advisor, Paul Newton, for his guidance and support throughout the entire thesis process. His wisdom and warmth have inspired me to achieve my academic and personal goals, and his humbleness is a truly a testament to his intelligence.

I would also like to acknowledge my thesis committee for their meaningful discussions and valuable feedback: Eva Kanso, for her wit and bright personality and for being a role model in how to enjoy academic success while raising two young boys; Paul Macklin, for his infectious enthusiasm for science and for giving me motivation to accomplish big things every time we talk; and a special thank you to Owen McCarty, for flying out from Portland to be a member of my committee. His energetic passion for the important things in life is inspiring, and I am grateful for our fruitful collaborations and his endless support of my work.

There are many whom I befriended during my time as a doctoral student at USC. I would like to thank Sam Graves for offering words of encouragement (and chocolate) whenever I visit her office, and for her constant support, both logistically and emotionally, through two pregnancies. I would like to thank my research group for sharing this experience of growth with me (in order of whom I met): Roxana Tiron, Fangxu Jing, Babak Oskouei,

Stephen Liao, Jeremy Mason, Andrew Tchieu, Prabu Sellappan, Kevin Phillips (OHSU), Garth Tormoen (OHSU), Brian Hurt, Jeffrey West, and Zaki Hasnain. I would also like to thank my few but valuable girlfriends in the AME department, Shanling Yang, Gauri Khanolkar, Okjoo Park, and Sydnie Lieb for our many enjoyable lunch dates. And I would like to acknowledge the ARCS Foundation for their generous financial support of my studies as an ARCS Scholar for the past three years.

My sincerest gratitude goes to my family for the constant love they poured upon me, especially my husband, Grant, for unconditionally loving me as I am; my two sons, Elliott and Brandon, for being a wonderful blessing and constantly giving me great joy; my parents, Young and Stella, for being there for me every single step of the way; my sister Diane and my brother Sam, for putting up with my idiosyncracies; my parents-in-law, Dong Ha and Kyung Ja, for their valuable academic advice throughout my graduate studies; my late grandfather, who showed me that the pursuit of knowledge and a career in education are fulfilling and rewarding; my best friends, Stella and Jane, for being my lifelong sisters in Christ; and my church family for their prayers for wisdom and strength that extend beyond my own abilities. Finally, all glory and honor and praise goes to the living God, who gives value to my work and a higher purpose to my life.

Table of Contents

Dedication	ii
Acknowledgements	iv
List of Figures	vii
List of Tables	x
Abstract	xi
Part I Low-dimensional deformation models for circulating cancer cells in flow	1
Chapter 1 Introduction	2
Chapter 2 The cell deformation and release experiment	7
2.1 MDA-MB-231 cell deformation and release experiment	7
2.2 Active shape model and principal components of deformation	8
Chapter 3 The low-dimensional deformation model and simulation results	12
3.1 The mathematical modeling assumptions	12
3.1.1 The cell surface model and constitutive assumption	12
3.1.2 Fluid flow computation	17
3.1.3 Numerical method	19
3.2 The cell deformation simulation	21
Part II Procoagulant circulating tumor cells in flow	31
Chapter 4 Introduction	32
4.1 Blood coagulation	33
4.2 Previous models	34
4.3 Description of the biology of thrombosis	36

Chapter 5	The clot formation model	43
5.1	Experimental methods	43
5.2	Experimental results	45
5.3	Mathematical infrastructure and Green's functions approach	47
5.3.1	Fluid dynamics and concentration field equations	47
5.3.2	The Green's function approach	48
5.3.3	Concentration field gradient tracking diagnostics	51
5.4	Simulation results	52
5.4.1	Two-dimensional concentration fields	52
5.4.2	Three-dimensional concentration fields	54
5.4.3	Gradient tracking results	57
Chapter 6	The fibrin formation model	63
6.1	Experimental methods and results	63
6.2	Model in a closed circular domain	64
Chapter 7	The computational fluid dynamics models	70
7.1	Development of the model from patient samples to computational simulation	71
7.2	Description of the mathematics and multiphysics used in COMSOL models .	72
7.2.1	Laminar two-phase flow with moving mesh	74
7.2.2	Transport of diluted species	76
7.2.3	Particle tracking for fluid flow	78
7.2.4	The implicit time-dependent solver algorithm	79
7.3	Modeling building process	80
7.4	Simulation results	84
7.4.1	Breast cancer single cell in a channel venule	84
7.4.2	Colon cancer single cell and cluster of two cells in a branching venule	87
7.4.3	Lung cancer cluster in a branching venule	94
Chapter 8	Discussion and future directions	99
8.1	Future work for deformation of cancer cells in flow (Part I)	99
8.2	Future work for procoagulant circulating tumor cells in flow (Part II)	101
Bibliography		106

List of Figures

1.1	Schematic of intravasation	4
2.1	Images of cell-release experiment	8
2.2	Adhesion by ligands	9
2.3	Principal components of deformation	11
3.1	Gaussian cell model	14
3.2	The training experiment	24
3.3	Cell surface parameters	25
3.4	x - z plane of the computational domain	26
3.5	Normal force on cell surface	27
3.6	Simulated forces acting on the cell surface	28
3.7	Pressure gradient	29
3.8	Cell surface parameters for simulated run	30
4.1	Schematic of coagulation reactions	34
4.2	Circulating tissue factor in blood vessel	35
4.3	Schematic of deep vein thrombosis	38
4.4	Schematic of artery vs. vein	39
5.1	Experimental setup for blood occlusion	44
5.2	Experimental results comparing CTC burden with occlusion time	46
5.3	Schematic for atmospheric dispersion modeling	50
5.4	Schematic of gradient tracker	52

5.5	2D simulation results for $n = 100$ cells	53
5.6	Long-time 2D simulation results for $n = 100$ cells	55
5.7	Computational domain for 3D model of diffusing cells	56
5.8	3D simulation results for $n = 4$ cells	59
5.9	Initial positions and concentration levels for 3D simulation	60
5.10	3D simulation results for $n = 100$ cells	61
5.11	Chemical field gradient tracking simulation	62
6.1	Single cell clotting assay experiment	64
6.2	2D simulation of CTCs in a circular blood vessel with no blood flow	66
6.3	Fibrinogen bridge simulation with two cells near center of vessel	68
6.4	Fibrinogen bridge simulation with two cells near circular wall of vessel	69
7.1	Development from patient sample to computational simulation	73
7.2	Model building: Step 1	80
7.3	Model building: Step 2	81
7.4	Model building: Step 3	81
7.5	Model building: Step 4	82
7.6	Model building: Step 5	82
7.7	Model building: Step 6	83
7.8	Simulation results for the breast cancer model	86
7.9	Colon cancer model development from image to mesh	88
7.10	Simulation results for the colon cancer model	89
7.11	Particle tracking simulation for the colon cancer model	91
7.12	Wake structure formation of the chemical thrombin field in the colon cancer model	93
7.13	Lung cancer model development from image to mesh	95

7.14	Simulation results for the lung cancer model	97
7.15	Particle tracking simulation for the lung cancer model	98
8.1	Flow diagram of modeling procedure for cell deformation model	100
8.2	Experimental setup of cancer cell passing through microfluidic channel . . .	105

List of Tables

7.1	Components in the bloodstream with their densities.	71
7.2	Velocities of vessels of different sizes in the venous system.	75
7.3	Coagulation factors with their respective diffusion coefficients, D	77

Abstract

In this thesis, we mathematically model and computationally simulate several aspects associated with the dynamics of circulating tumor cells in the bloodstream. We focus on physical processes that initiate cancer metastasis, such as intravasation and the subsequent diffusion of thrombin by the expression of tissue factor (TF) on the surface of the circulating tumor cells that are of epithelial origin.

In Part I, we develop a low-dimensional parametric deformation model of a cancer cell under shear flow. The surface deformation of MDA-MB-213 cells is imaged using DIC microscopy imaging techniques until the cell releases into the flow. We post-process the time sequence of images using an Active Shape Model (ASM) to obtain the principal components of deformation, which are then used as parameters in an empirical constitutive equation to model the cell deformations as a function of the fluid normal and shear forces imparted. The cell surface is modeled as a 2D Gaussian interface with three active parameters: H (height), σ_x (x-width), and σ_y (y-width). Fluid forces are calculated on the cell surface by discretizing the surface with regularized Stokeslets, and the flow is driven by a stochastically fluctuating pressure gradient. The Stokeslet strengths are obtained so that viscous boundary conditions are enforced on the surface of the cell and the surrounding plate. We show that the low-dimensional model is able to capture the principal deformations of the cell reasonably well and argue that Active Shape Models can be exploited further as a useful tool to bridge the gap between experiments, models, and numerical simulations in this biological setting.

In Part II, we describe a mathematical and computational model for diffusion-limited procoagulant circulating tumor cells (CTCs) in flow. We first build a model based on an exact formulation of Green's function solutions for domains with a blood vessel wall and for closed domains. Time-dependent gradient trackers are used to highlight the result that concentration fields build up near boundaries (vessel walls), in regions surrounding the diffusing particles, and in complex time-dependent regions of the flow where fields associated with different particles overlap. Then, as a next step to deal with more complex blood vessel geometries and actual CTC shapes obtained from DIC images of fluid biopsy samples, we use COMSOL Multiphysics and CellProfiler software to simulate initial configurations and various geometries relevant to venule sizes in the body. We develop CFD models based on finite element meshes of the imaged single cells and circulating tumor cell clusters. Our results indicate that the thrombin chemical fields diffuse to and collect at the blood vessel walls, and that the domain geometry combined with the spatial distribution of CTCs in flow determine local thrombin concentrations. The final chapter outlines what would be the next steps in the model developments of both Part I and Part II of the thesis.

Part I

Low-dimensional deformation models for circulating cancer cells in flow

Introduction

Portions of the work in Chapters 1, 2, and 3 were originally published by the American Institute of Physics in Physics of Fluids 2012; Volume 24, Article 081903.

Reprinted with kind permission

The ‘fluid phase’ of cancer begins when cancer cells making up the primary tumor mass are released into the bloodstream [48]. Some of these circulating tumor cells (CTCs) will become the future ‘seeds’ when they implant themselves at distant sites, and the deadly extravasation step in the metastatic cascade will commence [79]. The schematic associated with the main physical mechanisms involved in this early stage event is shown in Figure 1.1. Mechanical models for this intravasation step [41, 69] are important to develop, primarily for the purposes of gaining a fundamental understanding of the initiation of metastatic spread.

The reality of developing a high-fidelity model of circulating tumor cell and cell cluster deformation and release requires knowledge of (i) the competing forces acting on the cell surface from the incoming blood flow which act to potentiate the separation of the CTC

from the primary tumor, and the ligand-receptor bonds which hold the cell in place [10, 73]; (ii) knowledge of the constitutive equation associated with the cell membrane [73, 78] and a fine scale discretization of the deformable cell surface for a high fidelity numerical simulation; and (iii) modeling assumptions on the (blood) flow field, which is near the vessel wall, hence in the Stokes regime [22, 29, 46]. An example of free-standing computational models of cell deformation under flow are those of [42, 65] which focus on the ‘rolling’ regime of 3D deformable cells near vessel walls. A very comprehensive overview of the biomechanical properties of cancer cells is given in [73] along with references therein.

The primary goal of this thesis is not to develop and describe a free standing physics based model of circulating tumor cell deformation and release, but to show how a software tool called the ‘Active Shape Model’ (ASM) [19] can be exploited for use in bridging the gap that often exists between experiment and model development in the context of cancer cell deformation. In general terms, active shape models are statistical models that can track the shape of an object as it dynamically deforms. The models need to be trained on a sequence of images (the ‘training’ experiment) from which they learn the principal components of deformation of an object. In our context, we then use those trained principal components of deformation as inputs for a low-dimensional parametric deformation model of the cancer cell under flow. This allows us to compute the fluid forces on a model cell surface and calibrate/tune the parameters in an empirical constitutive equation relating forces to response, so that the response matches the trained principal components obtained from the experiment. Although ‘active shape models’, ‘active appearance models’ [18], and ‘active

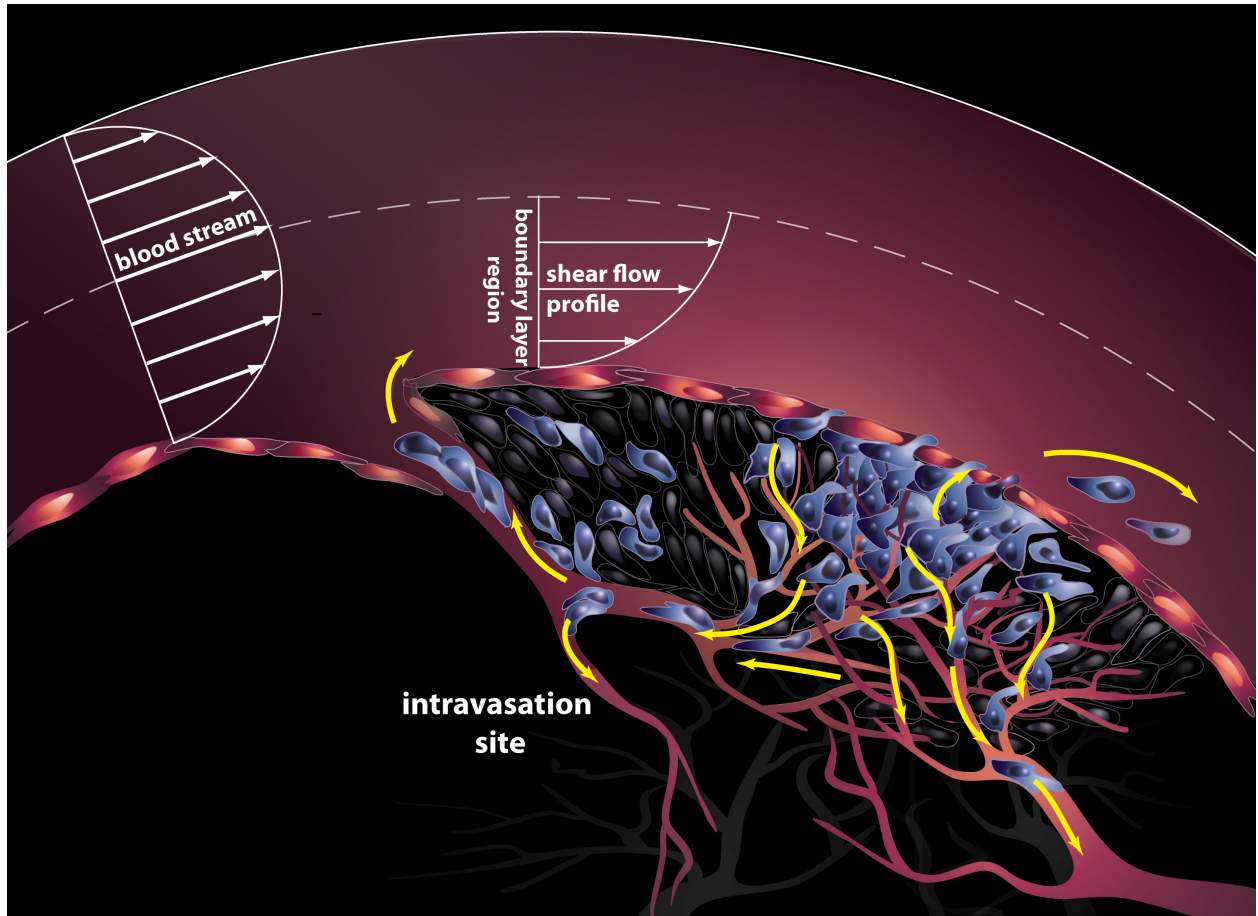


Figure 1.1: Schematic of intravasation

Schematic diagram showing the early stage of cancer progression, called the ‘intravasation’ stage. Primary tumor cells in contact with the bloodstream experience shear forces that can be strong enough to exceed the adhesion forces keeping them attached to the primary tumor. Upon release into the incoming flow, they become circulating tumor cells capable of spreading the disease to remote sites.

contour models’ [43] have been used in medical applications [20, 67], to our knowledge, their use in the context described here, i.e. to calibrate/tune parameters for use in an empirical constitutive equation, is new and potentially useful in situations where a first-principle constitutive equation is not known.

The main goals and steps of the procedures described in this thesis are laid out as follows:

1. In the physical experiment described, we cannot measure forces on the cell surface directly. We can only visualize the surface deformation/shape as a function of the external flow parameters and time (as shown in Figure 2.3).
2. For the numerical simulation, we do not have a good model for the constitutive equation for how the cell surface responds to forces, hence we cannot do a ‘stand-alone’ numerical simulation of the fluid-cell surface interaction and deformation.
3. Our goal is to obtain an ‘empirical’ constitutive law, trained from an experimental run. Once this is obtained, we can use the ‘trained’ model for Stokes flow numerical simulations in a more general setting.
4. To obtain the empirical constitutive force-response law, we make a ‘Hooke’s law’ (linear) constitutive assumption. Then, we use the sequence of shape changes obtained from the training experiment as inputs to our Gaussian surface model (some generic shapes are shown in Figure 3.1). This allows us to compute the fluid forces on the ‘low-dimensional’ deforming Gaussian surface using a Stokes flow simulation with distributed Stokeslets on the Gaussian surface. The outputs from the training run are shown in Figures 3.2 and 3.3.
5. We then use the ‘trained’ empirical constitutive equation to carry out a new flow simulation, both deterministic and stochastic. The flow simulation is driven by a deterministic and stochastic pressure gradient. The outputs from the flow simulation using the trained model is shown in Figures 3.7 and 3.6.

These highlight the main steps which we describe in more detail. We start by describing the experiment which we use to train the model.

The cell deformation and release experiment

2.1 MDA-MB-231 cell deformation and release experiment

The “training” experiment proceeds as follows. MDA-MB-231 cells (donated from Dr. Tlsty at the University of California, San Francisco, CA) were plated onto glass coverslips and incubated at 37°C and 5 CO₂ for 24 hours. Glass coverslips with plated MDA-MB-231 cells were assembled onto a flow chamber fitted with a silicon rubber gasket with a flow width of 0.25 cm and thickness of 0.005 in (Glycotech). See [7] for a general discussion of velocity fields for different flow chamber designs. The flow chamber was mounted on the stage of a Zeiss Axiovert 200M inverted microscope (Carl Zeiss). Dulbecco’s Modified Eagle Medium (DMEM, Invitrogen) with 10% fetal bovine serum (FBS, Invitrogen) was perfused over MDA-MB-231 cells at a fluid shear stress of 1 *dyne/cm*². The flow rate was doubled every 10 minutes to achieve shear stresses of 1, 2, 4, 8, 16, 32 *dynes/cm*². Real-time differential interference contrast (DIC) microscopy images were captured every 15 seconds

during perfusion with a $40\times, 0.75$ NA lens using Slidebook software (Intelligent Imaging Innovation).

A representative sequence of cell images under shear flow (obtained from 12 runs of the experiment) are shown in Figure 2.1. Flow is from left to right. At some point during each run, the cell releases and leaves behind the “ligand footprints” which kept it adhered to the slide. The ligand footprints are shown in Figure 2.2 in this case, 54 minutes into the run, 2 minutes after the cell releases.

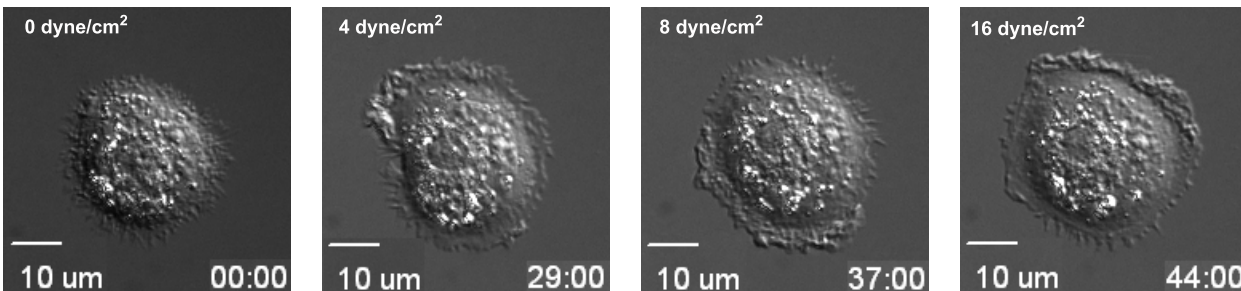


Figure 2.1: Images of cell-release experiment

DIC images of a MDA-MB-231 adherent cell subjected to increasing shear flow from 0 to 32 dynes/cm². The contact ring around the outer region of the cell ‘ruffles’ during the run. Flow is from left to right.

2.2 Active shape model and principal components of deformation

We post-process the sequence of images (roughly 200 images per run) using the open-source software tool ‘Active Shape Model’ (ASM). The ASM algorithm [19] is trained from a time sequence of manually drawn contours used as training images. We use the DIC images from

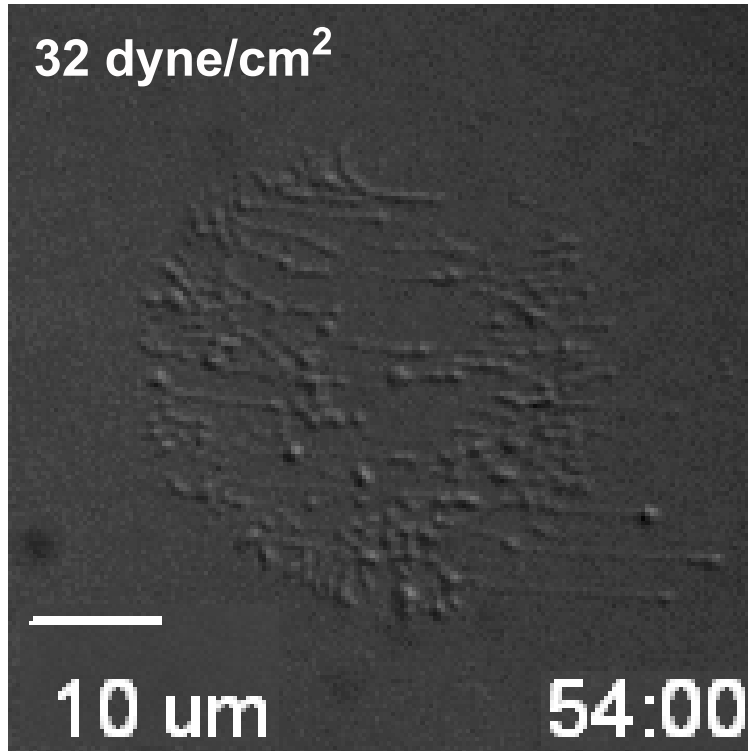


Figure 2.2: Adhesion by ligands

Ligand ‘footprints’ immediately after cell release into the flow. Adhesion force of cell ligands to slide must be overcome by shear force from the fluid-cell-surface contact for transition from tumor cell to circulating tumor cell to occur.

the experiment. With each image in the time sequence, we manually mouse-click the outline of the outer contour of the cell. This process could easily be automated for use in a larger setting, using an ‘active contour’ type of model [43], for example. The ASM algorithm then finds the main variations in the training data using Principal Component Analysis (PCA), which enables the model to automatically recognize if a contour is a possible or good object contour. For our purposes, we only use the two largest singular values that the model produces (in each frame) to obtain the elliptical shape of the outer contour as a function of time. The experiment was run 12 times and sequences of images for each run were retained.

We show an example of one of our post-processed sequences in Figure 2.3. In each case, the semi-major and semi-minor axes (λ_x, λ_y) , which the ASM produces, are shown. Also shown is the average cell shape (in white) produced by the ASM algorithm (averaged over 10 frames spanning 2 minutes) during each of the 10 minute windows in which the pressure gradient is held fixed. The black elliptical curves are the contours of the cell surface model described next. These sequences give rise to experimentally produced values for (λ_x, λ_y) in a time sequence. The cell height is not directly imaged/measured in these runs, hence, we make the assumption that cell volume is held constant which enables us to calculate height once we have the other two deformation parameters in the model.

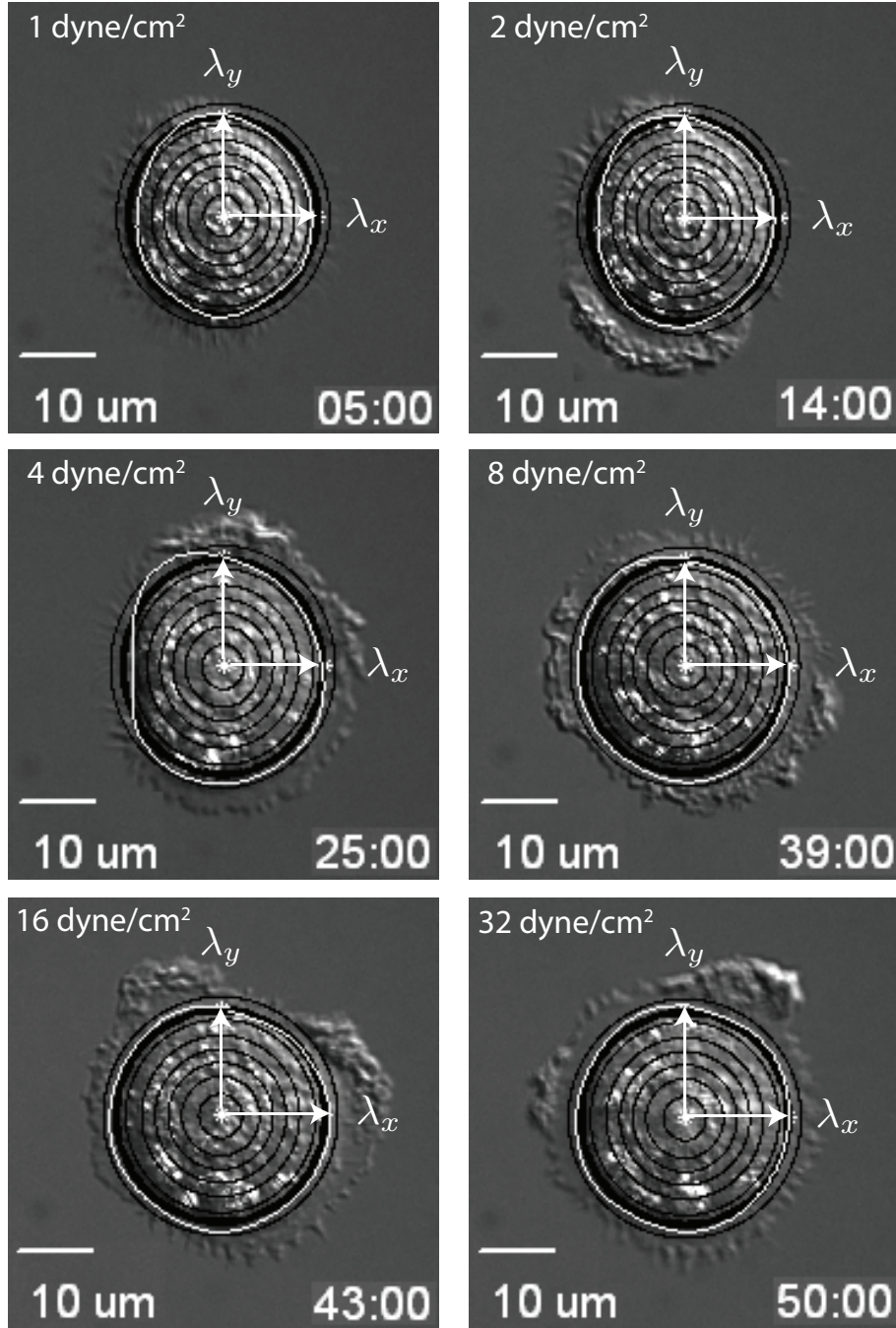


Figure 2.3: Principal components of deformation

Principal components of deformation (λ_x , λ_y) for 6 representative frames in a 52 min run. Time sequence shown: 5 min, 14 min, 25 min, 39 min, 43 min, 50 min. Cell releases into flow at 52 min. The white curve is the average cell shape obtained from the ASM algorithm during the 10 minute window in which the flow rate is fixed. The black curves are the contours of the Gaussian cell surface model. Thick black curve is the closest elliptical contour to the white curve. Cell width is roughly $20 \mu m$ across. Flow is from left to right.

The low-dimensional deformation model and simulation results

3.1 The mathematical modeling assumptions

We next describe how this experiment is used to tune the parameters in our low-dimensional model.

3.1.1 The cell surface model and constitutive assumption

In light of the fact that the cell deformations, as shown in Figure 2.1, are relatively small (compared with the cell size), we use a parametrically deformable surface model for the cell which is of Gaussian shape [81]:

$$h(x, y) = H \exp[-(a(x - x_0)^2 + 2b(x - x_0)(y - y_0) + c(y - y_0)^2)], \quad (3.1)$$

with parameters:

$$a = \frac{\cos^2 \theta}{2\sigma_x^2} + \frac{\sin^2 \theta}{2\sigma_y^2}, \quad (3.2)$$

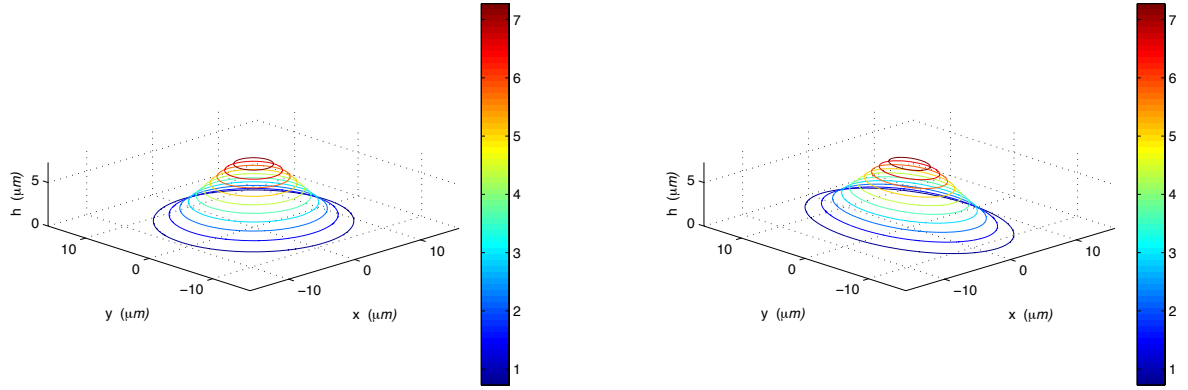
$$b = -\frac{\sin 2\theta}{4\sigma_x^2} + \frac{\sin 2\theta}{4\sigma_y^2}, \quad (3.3)$$

$$c = \frac{\sin^2 \theta}{2\sigma_x^2} + \frac{\cos^2 \theta}{2\sigma_y^2}. \quad (3.4)$$

Here, the cell surface height is given by $h(x, y)$, with peak cell height H , x -width σ_x , y -width σ_y , and the center of the cell marked by the coordinates (x_0, y_0) . The cell orientation parameter θ is held fixed during the simulation, although for more complex cell tracking experiments, both (x_0, y_0) and θ could vary.

Contours of the cell surface are shown in Figure 2.3. Since the cell height is not directly available, we use the (approximately correct) assumption that the volume enclosed by the cell (above the plate) is constant as the cell deforms, which provides a constraint on the three parameters (H, σ_x, σ_y) . Examples of the cell surface model in ‘z-stack’ form (contour slices of the surface at various heights), with two representative parameter values are shown in Figure 3.1. In general terms, the 2D Gaussian surface we generate this way closely contours the 2D shape of the cell surface, but we do not yet know how to vary the parameters of the model (H, σ_x, σ_y) as a function of the fluid forces produced on the cell surface.

To link the parametric cell deformation model with the fluid flow forces produced, we start with the constitutive assumptions $\sigma_x(f_x, f_y)$, $\sigma_y(f_x, f_y)$ relating cell deformation (response) to forces imparted in each of the x (streamwise) and y (spanwise) directions. In the experiment,



(a) $\theta = 0, \sigma_x = 5, \sigma_y = 5, H = 8;$

(b) $\theta = 0, \sigma_x = 4, \sigma_y = 6.25, H = 8;$

Figure 3.1: Gaussian cell model

Cell model with two different parameterizations shown in ‘z-stack’ form. The parameters σ_x , σ_y , and H vary, but are constrained so that the total volume above the glass slide inside the cell is held constant.

the flow is nearly unidirectional (along the x -direction) so the deformation response is much stronger in this direction than in the cross-flow (y) direction. For this reason, $\partial\sigma_x/\partial f_y \approx 0$, and $\partial\sigma_y/\partial f_x \approx 0$, so we can use a simpler assumption $\sigma_x(f_x), \sigma_y(f_y)$. The pressure gradient driving the flow is increased in steps, hence the corresponding forces imparted increase in steps as well. We therefore Taylor expand the deformation functions:

$$\sigma_x(f_x) = \sigma_x(0) + \sigma'_x(0)(f_x) + \dots, \quad (3.5)$$

$$\sigma_y(f_y) = \sigma_y(0) + \sigma'_y(0)(f_y) + \dots, \quad (3.6)$$

truncating the expansions after the linear terms in (f_x, f_y) . This is what we call our ‘linear constitutive’ assumption. Based on these equations, we set up an iterative scheme of the form:

$$\sigma_x^{(n+1)} = \sigma_x^{(n)} + \alpha_x f_x \quad (3.7)$$

$$\sigma_y^{(n+1)} = \sigma_y^{(n)} + \alpha_y f_y, \quad (3.8)$$

where $\alpha_x \equiv \sigma'_x(0)$, $\alpha_y \equiv \sigma'_y(0)$, and $\sigma_x^{(n)} \equiv \sigma_x(0)$, $\sigma_y^{(n)} \equiv \sigma_y(0)$. We call these equations the ‘linear force-response’ equations. We then iterate these equations (from frame to frame) throughout the flow run. The variables $\sigma_x^{(n+1)}$ and $\sigma_y^{(n+1)}$ are the width variables (in frame $n + 1$) that we use in our Gaussian surface model, while $\sigma_x^{(n)}$ and $\sigma_y^{(n)}$ are the corresponding values before the iteration step (in frame n). We obtain these from the principal components of deformation (λ_x, λ_y) from the flow experiment. The variables f_x and f_y are the x -component and y -component of the surface normal force on the cell that we numerically compute. From these equations, we obtain the linear parameters α_x and α_y at each iteration (the data points in Figure 3.2), which we then average over each 10 minute window (shown in Figure 3.2) while the deterministic component of the pressure difference driving the flow is held at a fixed nominal value. Since the flow is coming entirely from the x direction, and not the y direction, the magnitudes of the forces in these two directions are of different orders. Hence, the coefficients α_x and α_y are of different orders of magnitude, which is what we expect. In addition, due to the uni-directional nature of the incoming flow (approximately

one-dimensional), our simple form for the constitutive equation captures the deformations reasonably well.

The deformations of the cell surface parameters are shown in Figure 3.3, which depict how the cell height H varies throughout the experimental run. We have divided the time regime into a region to the left of the vertical dashed line (i.e. $T < 15$), and a region to the right (i.e. $T > 15$). The horizontal lines in these two regions depict the average cell height. Note the change in this height in these two regimes, the first being fairly constant, followed by an abrupt flattening out of the cell. Roughly speaking, this change in height follows from the fact that both σ_x and σ_y both increase, and the volume under the cell is held constant. In the first regime ($T < 15$), the cell seems to be responding in a mechanically passive way to the flow forces. In the second regime ($T > 15$), the cell response seems to become active, as it is actively attempting to flatten itself to the incoming flow. Various types of active responses have been discussed, documented, and modeled in the literature. For example, [38] discuss a cell's propensity to orient in such a way as to reduce the total force on its nucleus. Active nucleus movement in response to shear has also been reported in [49], while active cytoplasmic response to shear is reported in [50]. Whether or not the transition we see at $T \sim 15$ is due to any of these effects is hard to pin down from these particular sets of experiments without more detailed nucleus and cytoplasmic visualization.

3.1.2 Fluid flow computation

To obtain the forces on the cell surface (which are not measured directly in the experiment), we perform a stochastic fluid flow simulation. Since the flow relevant to the cell release experiment is very near the glass plate, on which we assume viscous boundary conditions, the Reynolds number is small ($Re = UL/\nu \ll 1$), where U is a representative flow velocity, L is taken to be the flow chamber length, and ν is the fluid kinematic viscosity of blood plasma. Therefore, as in [29], we assume the flow is governed by the Stokes equations and the continuity equation:

$$\mu \Delta^* \vec{u}^* = \nabla^* p^* \quad (3.9)$$

$$\nabla^* \cdot \vec{u}^* = 0, \quad (3.10)$$

where $\nabla^* p^*$ is the pressure gradient driving the flow in the chamber, μ is the viscosity of the surrounding fluid, whose value we take as that for blood plasma, and $\vec{u}^* = (u^*, v^*)$ is the convective velocity of the fluid. The $*$ denotes quantities that are dimensional, and unstarred quantities will denote dimensionless variables.

Our first task is to scale the dimensional variables in a way that is consistent with the experiment. We use the following scalings: $x^* = lx$, $y^* = ly$, $p^* = \Delta P p$, and $u^* = Uu = \frac{\Delta P h^2}{8\mu L} u$. $l = 10\mu\text{m}$ is a representative length of the cell, $h = 0.0127\text{ cm}$ and $L = 5\text{ cm}$ are the height and length of the flow chamber, $\Delta P = 10\text{ dyne/cm}^2$ is a representative pressure drop which drives the flow down the chamber across the cell surface, and $\mu = 0.9cP$, which is the

value for the HBSS media used in the experiment (viscosity of blood is roughly $\mu = 3.2cP$).

If we assume a parabolic flow profile [7]:

$$u(y) = \frac{\Delta P}{2\mu}y(h - y), \quad (3.11)$$

then the maximum velocity occurs at the centerline $y = h/2$ from which we take our velocity scale to be $U = \Delta Ph^2/8\mu L$.

The dimensionless equations then become:

$$\frac{\beta^2}{8}\Delta\vec{u} = \nabla p \quad (3.12)$$

$$\nabla \cdot \vec{u} = 0. \quad (3.13)$$

The pressure conditions are then normalized to 1 (incoming) and 0 (outgoing), and the fluid velocity at the plate $y = 0$ is $\vec{u}(x, y = 0) = 0$. $\beta = h/l$ is the dimensionless parameter relating the chamber height to the length of the cell, which in our experiment is roughly $\beta = 1.27$. To compute the forces on the cell surface, we follow the approach described in [21], namely, we consider the dimensionless system (3.12), (3.13) augmented with an external force \vec{F} which accounts for the interaction between the fluid flow and the cell membrane.

Hence we use:

$$\frac{\beta^2}{8}\Delta\vec{u} = \nabla p - \vec{F} \quad (3.14)$$

$$\nabla \cdot \vec{u} = 0. \quad (3.15)$$

3.1.3 Numerical method

We use the method of regularized Stokeslets described in [21] to simulate the flow in a chamber with one cell attached to the plate. A Stokeslet is a fundamental solution to the steady Stokes equations, and it represents the velocity due to a concentrated external force at a point in the fluid. Smoothing the force over a small ball, instead of concentrated at a point as a Dirac delta function, produces regularized Stokeslets, and this resolves many of the numerical issues that arise from singularities in the Stokes equations.

We discretize the force \vec{F} on the cell surface with a distribution of regularized Stokeslets [21, 36] located at the grid points \vec{x}_i , $i = 1, \dots, N$, where:

$$\vec{F}(\vec{x}) = \sum_{i=1}^N \vec{f}_i \phi_\epsilon^{(i)}(\vec{x} - \vec{x}_i), \quad (3.16)$$

where \vec{f}_i is the strength of the i th Stokeslet, \vec{x}_i is its location, and $\phi_\epsilon^{(i)}$ is a regularizing function which has the property:

$$\lim_{\epsilon \rightarrow 0} \phi_\epsilon(\vec{x}) = \delta(\vec{x}), \quad (3.17)$$

where $\delta(\vec{x})$ is the usual Dirac delta function. We use the function:

$$\phi_\epsilon(\vec{x}) = \frac{2r^2 + 5\epsilon^2}{(r^2 + \epsilon^2)^{5/2}}, \quad (3.18)$$

$r^2 = \|\vec{x}\|^2$, which is a standard regularization discussed in [21]. The Stokeslet ‘blob’ velocity field in R^3 is then given by:

$$\frac{\beta^2}{8}\vec{u}(\vec{x}) = (\vec{f}_i \cdot \nabla)\nabla B_\epsilon(\vec{x} - \vec{x}_i) - \vec{f}_i G_\epsilon(\vec{x} - \vec{x}_i), \quad (3.19)$$

where $G_\epsilon(\vec{x})$ is the solution to:

$$\Delta G_\epsilon = \phi_\epsilon(\vec{x}), \quad (3.20)$$

and $B_\epsilon(\vec{x})$ is the solution to:

$$\Delta B_\epsilon = G_\epsilon(\vec{x}) \quad (3.21)$$

in infinite space. G_ϵ can be thought of as the regularized Green’s function for the problem.

More specifically, we want to determine the forces along the plate and the surface of the cell. A two-dimensional slice of the computational domain is shown in Figure 3.4. The flow (left to right) is driven by a constant pressure gradient that has reached a steady state. The inflow and outflow velocity conditions are set to be the parabolic Poiseuille flow profile, and viscous no-slip boundary conditions are enforced at the walls of the chamber and along the bottom plate, including the cell surface.

In the 3-D numerical model, the computational domain is set to be: $-L < x < L, -L < y < L, 0 < z < W$, where $L = 40$ is the length of the domain in the x and y directions.

$W = 10$ is the length of the domain in z direction. The grid spacing is determined by $dx = 1$. $N = 81 \times 81 \times 11 = 72,171$ are the total number of Stokeslets used in the simulation. The regularization parameter, ϵ , that we use is one-fourth of the grid spacing. For the simulation, Stokeslets are placed at every grid point in the computational domain, and the grid spacing is uniform in all three dimensions. Figure 3.4 shows the $x - z$ slice of the computational domain. The parameters of the cell surface are: H , the maximum height of the cell; σ_x , the width in the x -direction. We set the plate, which cuts off the Gaussian at the base, at $a = 0.005 \times H$. The Stokeslets above the plane $z = a$ represent the cell surface while those below represent the plate. The rest of the Stokeslets (not pictured in the schematic) lying above the Gaussian surface, represent the fluid.

To simulate the flow induced by the constant pressure gradient, a constant force $(\Delta P, 0, 0)$ is imposed on the grid covering the interior of the chamber. The velocity due to this force is computed on the channel walls using the regularized Stokeslets solution for velocity. Then, the forces along the plate and along the cell surface are computed so that the boundary conditions are enforced. The forces on the cell surface, which we are more interested in, are plotted in Figure 3.5 and Figure 3.6. Details of how to use the regularized Stokeslets to compute forces on surfaces can be found in [1, 21].

3.2 The cell deformation simulation

The cell deformation simulation using the trained model proceeds as follows. We carry out both a deterministic and a stochastic simulation. For the stochastic simulation, we obtain

a nominal value of the pressure gradient chosen to match the experiment, then we add a random fluctuation with amplitude taken to be 10% of the base value for the deterministic pressure. The random fluctuation is taken to be a uniformly distributed random variable. This is shown in Figure 3.7. The forces on the model cell surface are computed throughout a flow simulation in which we double the pressure gradient in each 10 minute interval of time. The forces on the cell surface are computed using the regularized Stokeslet method, and the parameters α_x and α_y in the empirical constitutive equations (3.7), (3.8) are averaged across 10 minute intervals, taking a moving average in which a window of 20 minutes is used to perform the averages. The forces on the cell surface and the parametric deformations are shown in Figures 3.6 and 3.8, respectively.

Figure 3.8 is particularly instructive and interesting with respect to how the cell height H varies throughout the run. We have divided the time regime into a region to the left of the vertical dashed line (i.e. $T < 15$), and a region to the right (i.e. $T > 15$). The horizontal lines in these two regions depict the average cell height. Note the change in this height in these two regimes, the first being fairly constant, followed by an abrupt flattening out of the cell. Roughly speaking, this change in height follows from the fact that both σ_x and σ_y both increase, and the volume under the cell is held constant. In the first regime ($T < 15$), the cell seems to be responding in a mechanically passive way to the flow forces. In the second regime ($T > 15$), the cell response seems to become active, as it is actively attempting to flatten itself to the incoming flow. Various types of active responses have been discussed, documented, and modeled in the literature. For example, [38] discuss a cell's propensity to

orient in such a way as to reduce the total force on its nucleus. Active nucleus movement in response to shear has also been reported in [49], while active cytoplasmic response to shear is reported in [50]. Whether or not the transition we see at $T \sim 15$ minutes is due to any of these effects is hard to pin down from these particular sets of experiments without more detailed nucleus and cytoplasmic visualization.

Figure 3.6 shows the simulated forces acting on the cell surface from both deterministic and stochastic runs. This figure should be compared with Figure 3.2(b), which are the forces from the training experiment. The force plots are qualitatively similar. Figure 3.8 shows the simulated parameter deformations through the flow simulation. In this figure, we show a deterministic simulation and a stochastic simulation, where the stochastic fluctuations are taken to be 10% of the deterministic base flow. Comparisons of Figures 3.3 and 3.8 show that the parametric deformation of σ_x , σ_y , and H between the experiment and the low-dimensional model are trending in the same direction and are qualitatively similar, although quantitative details differ, due presumably to the stochastic component to our flow field and the low-dimensionality of our model.

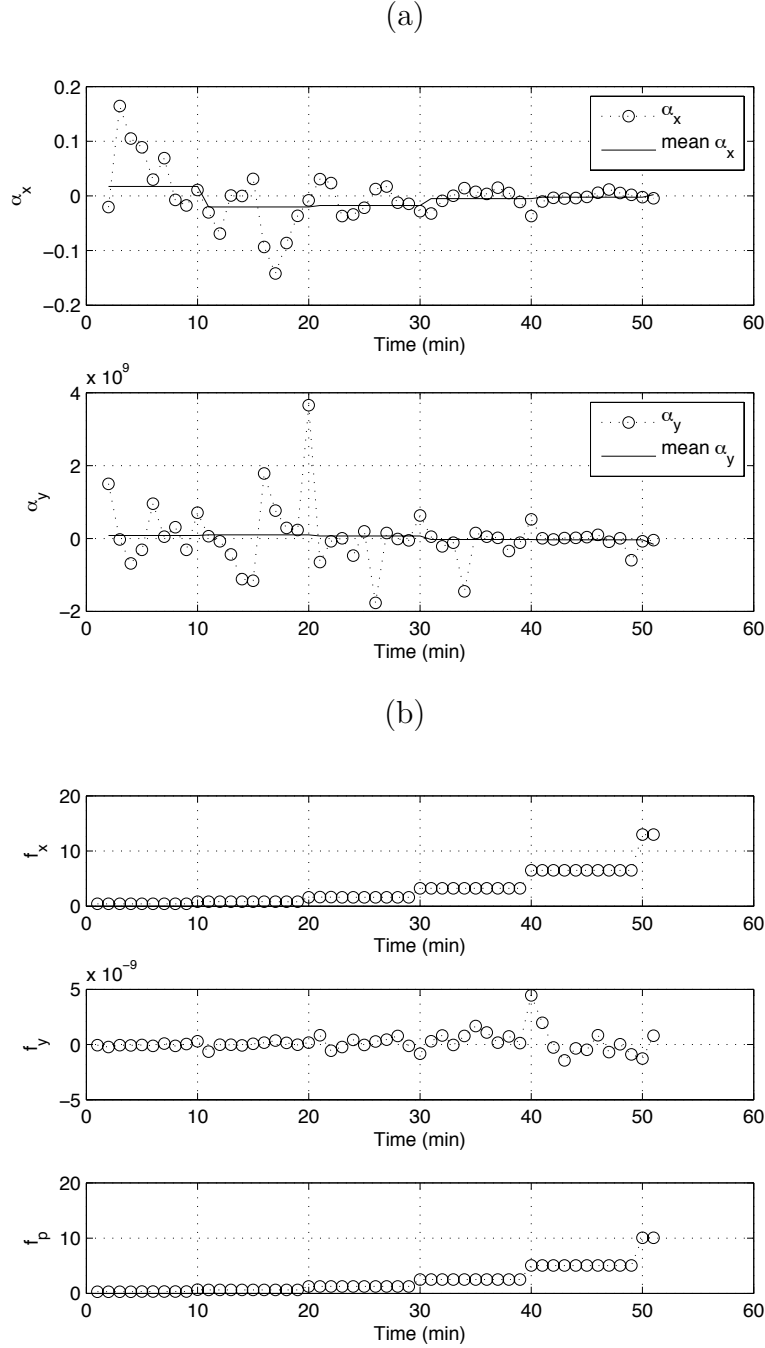


Figure 3.2: The training experiment

(a) Force-response parameters α_x , α_y as a function of time. The orders of magnitude are different because the flow is incoming in the x -direction, hence forces are much larger in this direction compared to the cross-flow y -direction. (b) Forces acting on the cell surface. Force in x -direction: f_x ; Force in y -direction: f_y ; Peak normal force: f_p . Note the difference in magnitude of the forces in the x and y directions, due to the fact that the flow is incoming and outgoing along the x -direction. Force units are in *dynes*.

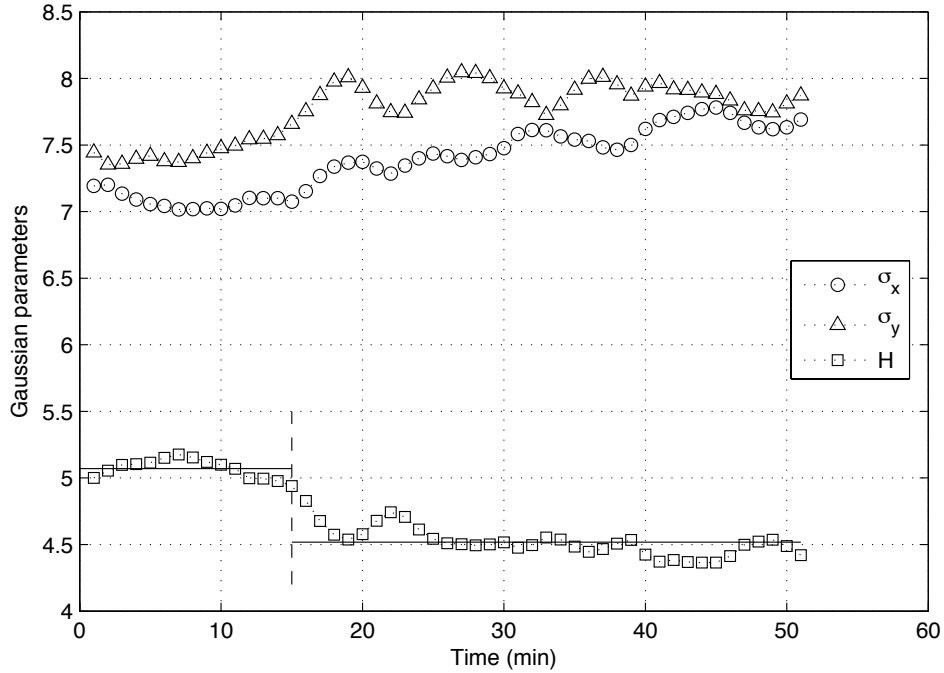


Figure 3.3: Cell surface parameters

Deformation of the cell surface parameters σ_x , σ_y , H , as a function of time. To the left of the dashed line ($T < 15$), H remains relatively constant (horizontal lines denote the average height in the two regimes). To the right of the dashed line ($T > 15$), H abruptly flattens out. Since there is no corresponding abrupt change in the flow, we view the regime $T < 15$ as a ‘passive mechanical response’ regime, whereas for $T > 15$, the cell seems to be actively responding to the flow.

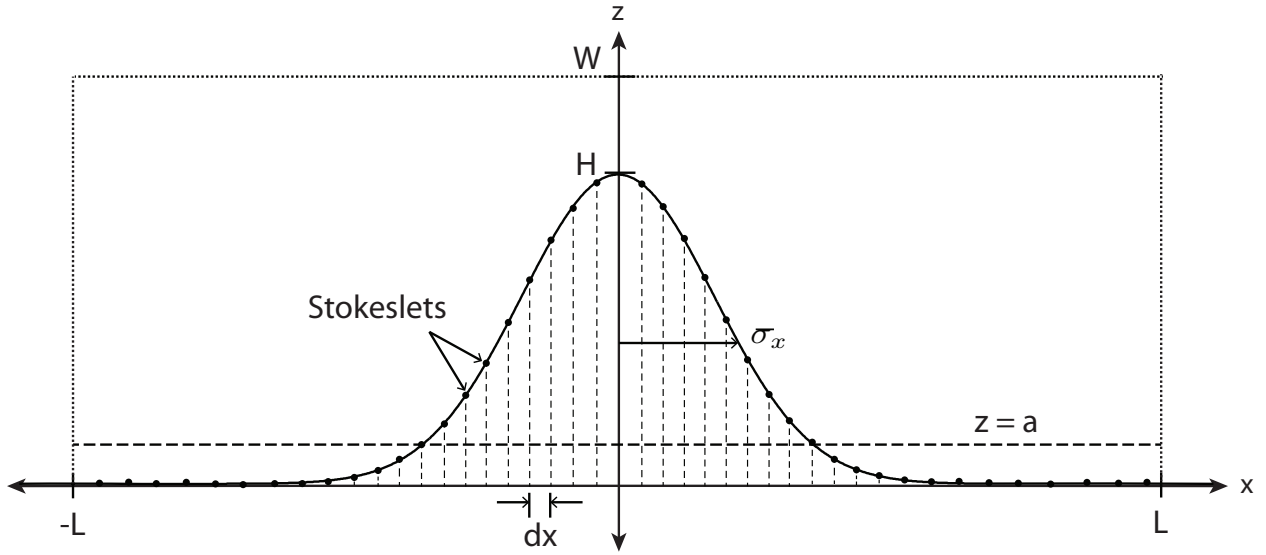


Figure 3.4: x - z plane of the computational domain

The 3D computational domain for our cell deformation model is $-L < x < L$, $-L < y < L$, and $0 < z < W$, where $L = 40$, $W = 10$, $dx = 1$, and $a = 0.005 * H$. H is the maximum height of the cell surface, and σ_x is the x -width parameter in the Gaussian cell surface shape. Regularized Stokeslets are placed at every grid point on the cell surface and in the fluid domain. The Stokeslets above the plane $z = a$ represent the cell surface, while those below the plane represent the plate.

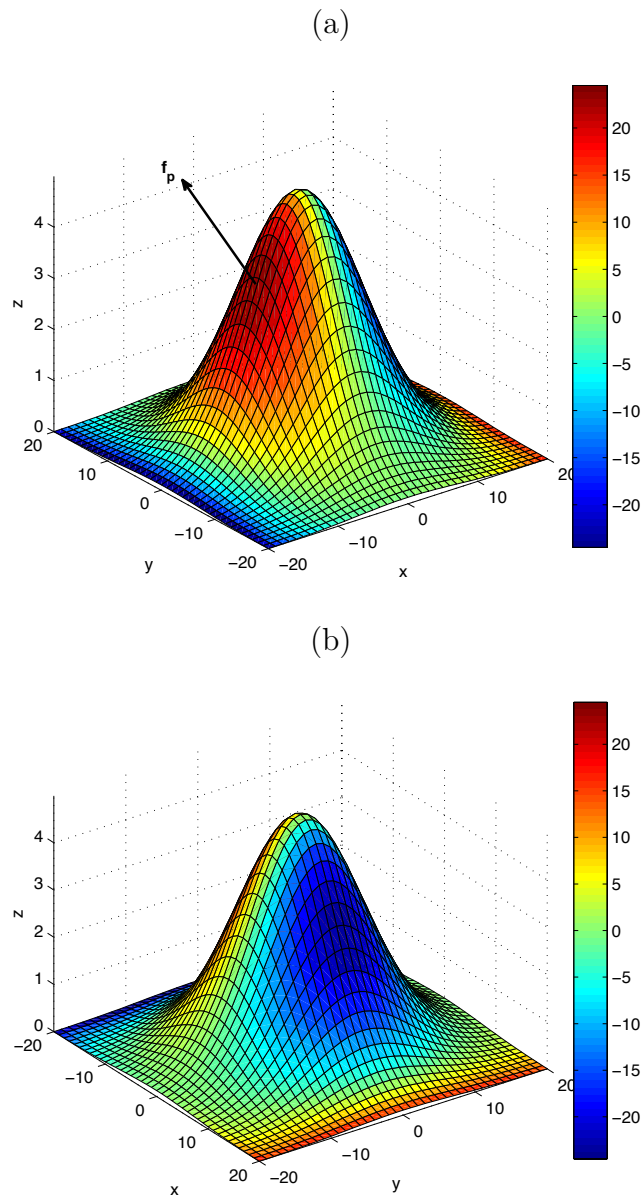


Figure 3.5: Normal force on cell surface

Normal force on cell surface computed by discretizing the surface with regularized Stokeslets whose strengths are chosen to enforce the viscous boundary conditions. (a) Front of cell (with respect to incoming flow). f_p is the maximum normal force on the cell surface.; (b) Back of cell (with respect to incoming flow). Force units are in *dynes*.

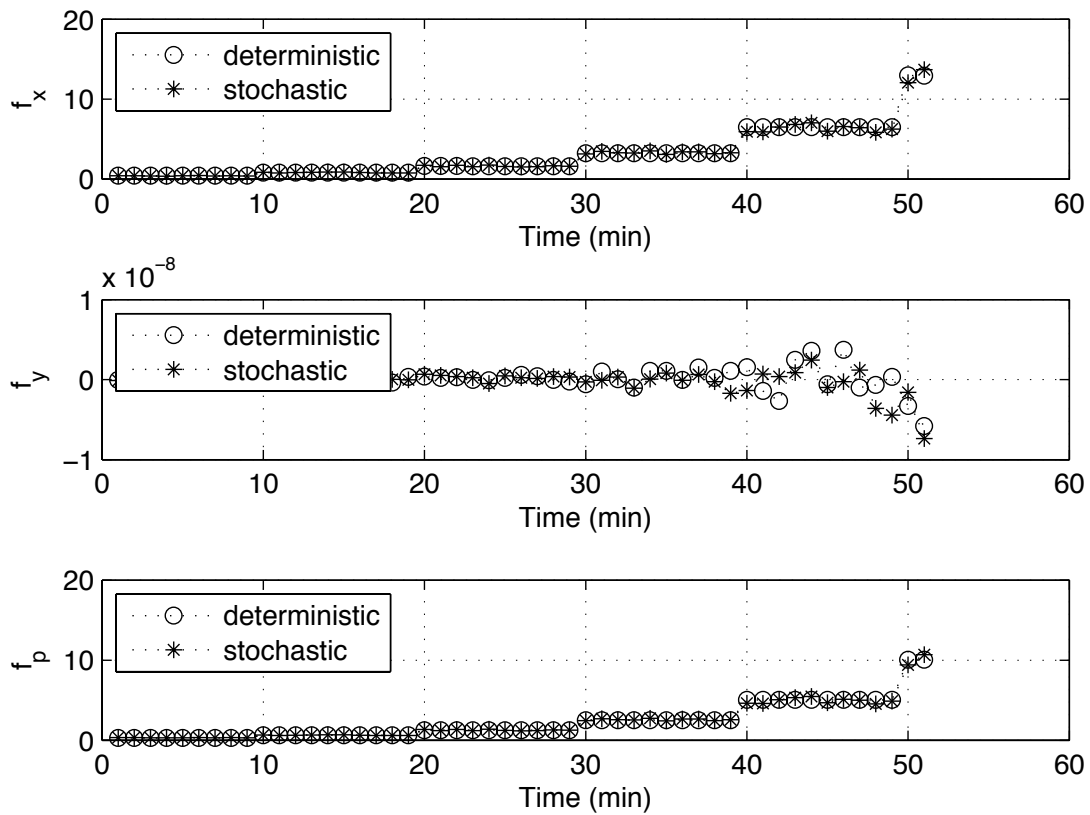


Figure 3.6: Simulated forces acting on the cell surface

Force in x -direction: f_x ; Force in y -direction: f_y ; Peak normal force: f_p . Note the difference in magnitude of the forces in the x and y directions, due to the fact that the flow is incoming and outgoing along the x -direction. Force units are in *dynes*. Plot should be compared with Figure 3.2(b).

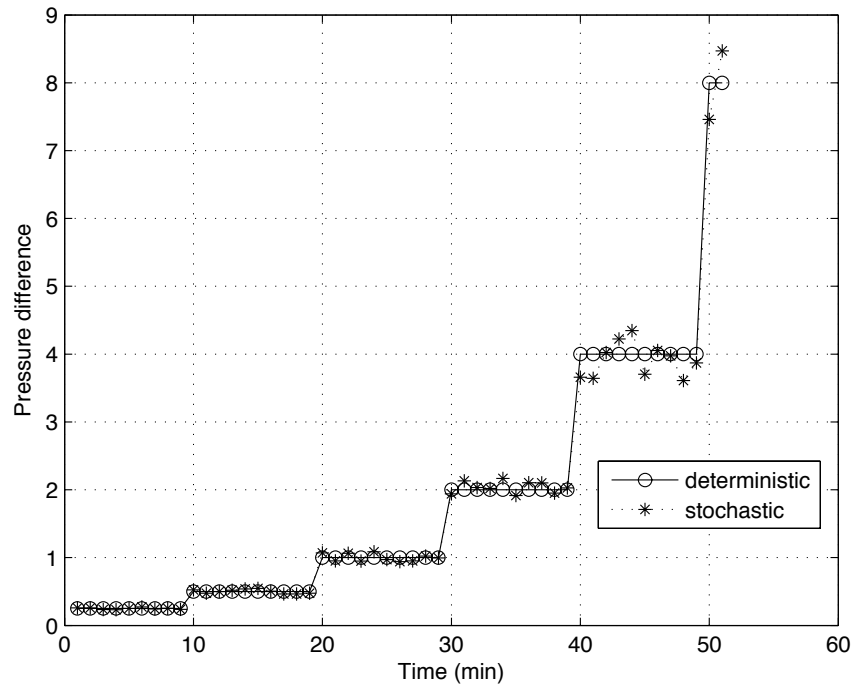


Figure 3.7: Pressure gradient

Pressure difference (inflow minus outflow) driving the flow as a function of time in the numerical simulation. Pressure difference doubles every 10 minute interval of time. Stochastic fluctuation is taken to be 10% of the base value. Units are in dynes/cm^2 .

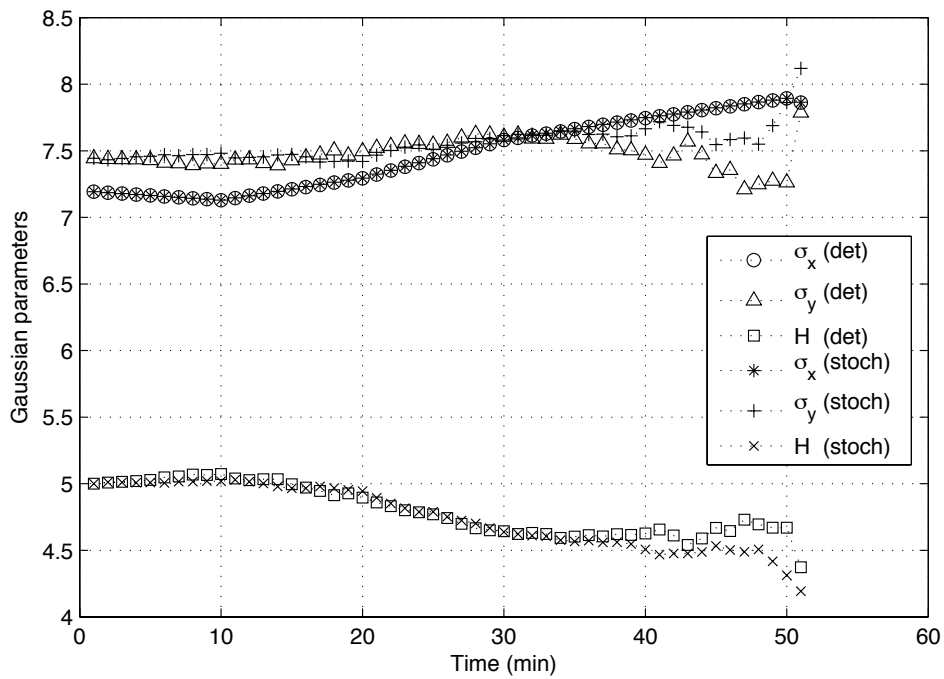


Figure 3.8: Cell surface parameters for simulated run

Deformation of the cell surface parameters σ_x , σ_y , H , as a function of time as obtained from the numerical simulation. Stochastic fluctuations are taken to be 10% of the deterministic base flow. The plot should be compared with the experimental run shown in Figure 3.3.

Part II

Procoagulant circulating tumor cells in flow

Introduction

Portions of the work in Chapters 4 and 5 were originally published by

Frontiers in Oncology 2012; Volume 2, Article 108.

Reprinted with kind permission

Blood clotting, or thromboembolism, is the second highest cause of death in cancer patients [45]. Unregulated coagulation is dangerous because blood clots that occur in the brain can lead to stroke, and clotting in the lungs can lead to pulmonary embolisms. Circulating tumor cells express tissue factor, which circulates in flow and initiates a coagulation cascade often seen in metastatic cancer patients [57]. Metastatic cancer is associated with increased levels of intravascular tissue factor and a high risk of venous thromboembolism [30]. Concentration fields of serine proteases, enzymes generated following the exposure of tissue factor, diffuse to and from CTCs as they propagate through the bloodstream [16]. Our goal is to model and computationally simulate this process in simple settings. At this stage, chemical

reactions are not included in the model, and only the diffusion of different species under flow is examined.

4.1 Blood coagulation

Blood coagulation is a process of the hemostatic system, which also includes platelet aggregation and fibrinolysis. The main functions of the hemostatic system are to heal injured blood vessels and to prevent bleeding. The clotting interactions are extremely complex and require a delicate balance of hemostasis. If this balance is disrupted, the results can be very dangerous and even fatal, with one side of the imbalance resulting in persistent bleeding and hemorrhage and the other side giving rise to thrombosis (intravascular blood clotting) and possible vessel occlusion due to the thrombi (intravascular clots). Cancer metastasis and the circulating tumor cells that are the vehicles of metastasis can be a cause of thrombosis [62, 76].

Coagulation involves a network of tightly-regulated reactions of enzymes in the blood (Figure 4.1) [28, 32]. The initiation of coagulation by circulating tissue factor occurs on the surfaces of procoagulant cells (Figure 4.2) [34]. The kinetics of tissue-factor initiated enzyme activation are dependent on the physiological and chemical properties of TF-bearing surface and its interface with blood. Coagulation occurs in the presence of flowing blood, and therefore it is strongly influenced by the fluid dynamics [56]. We aim to model and study the effects of flow on the diffusion of tissue factor expressed by CTCs.

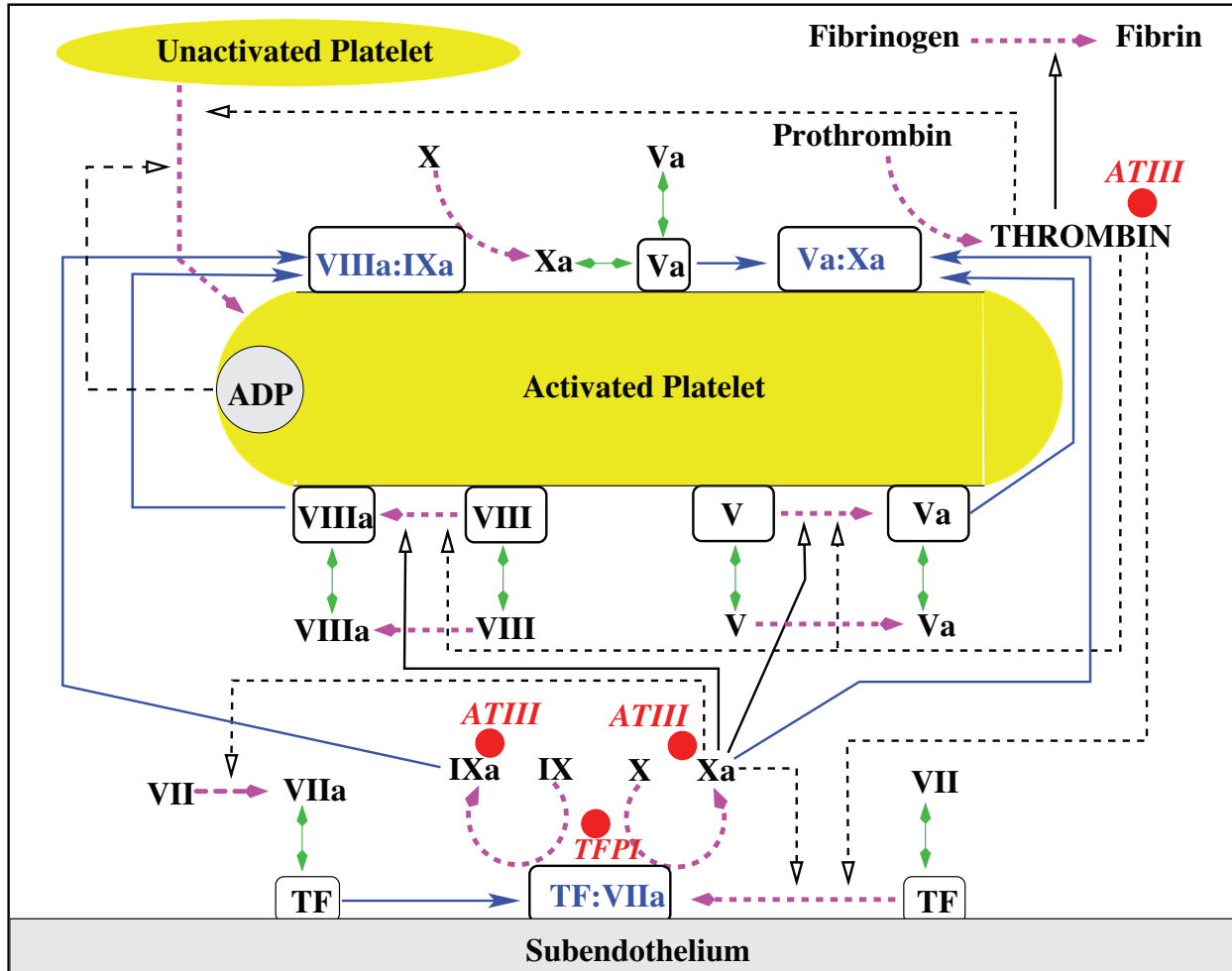


Figure 4.1: Schematic of coagulation reactions

Schematic of coagulation reactions. Dashed magenta arrows show cellular or chemical activation processes. Blue arrows indicate chemical transport in the fluid or on a surface. Green segments with two arrowheads depict binding and unbinding from a surface. Rectangular boxes indicate surface-bound species. Solid black lines with open arrows show enzyme action in a forward direction, while dashed black lines with open arrows show feedback action of enzymes. Red disks indicate chemical inhibitors.

4.2 Previous models

There have been numerous models that have examined parts of the hemostatic system. The previous models loosely fall under two categories: hydrodynamic modeling of the mechanics

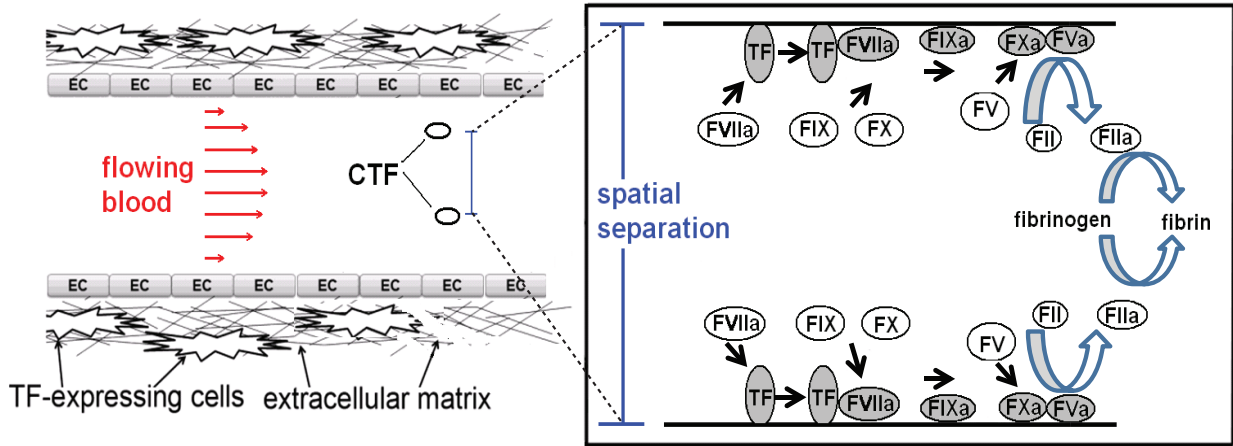


Figure 4.2: Circulating tissue factor in blood vessel

Circulating tissue factor (CTF) is expressed from the circulating tumor cells (CTCs). Endothelial cells (EC) form the lining of the blood vessel. Blood flow is shown as a shear Poiseuille profile. Extracellular matrix and other TF-factor expressing cells lie outside of the blood vessel. The inset shows the spatial separation between the surface of two CTCs, and TF is one of the initial enzymes that starts the cascade of biochemical reactions. The end product, fibrin, forms the fibers of the blood clot.

of blood flow during coagulation, and the kinetics of coagulation biochemistry. In the former category, Dzwiniel et al. used a discrete-particle model of blood dynamics in capillary blood vessels and concluded that aggregation of red blood cells in capillary vessels can be stimulated by depletion forces and hydrodynamic interactions [25]. Anand et al. incorporated the mechanics of flow with a growing blood clot by modeling both blood and clots as shear-thinning viscoelastic fluids [3]. The model included reaction equations of prothrombinase and tenase, but they did not represent all of the reactions in the coagulation system. Bodnar and Sequira used a simplified version of Anand's model, in which the physical domain is one-dimensional, to simulate blood clotting in three dimensions [11].

In the latter category, the Hockin-Mann reaction network model, which is a homogenous ordinary differential equation (ODE) reaction scheme, accurately predicts the initiation times of blood coagulation at various levels of tissue factor [39]. Building upon the Hockin-Mann model, Chatterjee et al. modeled the kinetics of coagulation initiation, specifically platelet activators [15]. Surprisingly, human blood was found to clot *in vitro* due to the activity of Factors XIIIa and XIa, which proceeds in the absence of tissue factor.

Fogelson et al. has developed an extensive model with both platelet aggregation under flow with coagulation biochemistry [26, 27]. His comprehensive model is the first to couple the interactions of both phenomena, and it shows the importance of platelet interaction with surface-bound chemicals and competition for binding sites during the maintenance and regulation of the coagulation cascade. Gregg further improved upon this model by accounting for the significant growth of a thrombus, or blood clot, and the physical effects of this growth on local flow and transport of chemical enzymes [33, 51]. The previous models examine coagulation at a site of injury or a cut in the blood vessel, not the coagulation that is activated by circulating tumor cells in metastatic cancer patients. The model we propose focuses on the chemical concentration fields of tissue factor expressed from procoagulant cancer cells in blood flow, but it does not yet include chemical reaction equations.

4.3 Description of the biology of thrombosis

Metastatic cancer accounts for the majority of deaths caused by cancer. Metastasis is believed to result from tumor cells from a primary site, migrating towards and intravasating

into a blood vessel, navigating the blood circulation to arrive at a distant site whereby it arrests from the blood flow, extravasates and establishes a metastatic tumor site. The process of metastasis thereby exposes a tumor cell to a variety of new environments, and poses significant physical challenges the tumor cell must overcome if it is to successfully metastasize.

Deep vein thrombosis, or deep venous thrombosis (DVT), is the formation of a blood clot in a deep vein, predominantly in the legs (refer to Figure 4.3). The detachment of a large clot that travels to the lungs can result in a pulmonary embolism, which is a life-threatening medical condition. Metastatic cancer patients are especially at risk of developing this potential complication, since circulating tumor cells are known to increase the occurrence of clotting in blood vessels. Large blood clots in the lower extremities caused by circulating tumor cells typically occur in the venous system of the circulatory system (shown in Figure 4.4), as opposed to the arterial system, because veins are low-pressure vessels that carry deoxygenated blood back to the heart, creating conditions that favor the formation of DVTs. Therefore, in the following chapters, we create models based on physiological blood parameters found in the venous system, such as blood vessel diameter and flow rate.

The interactions between circulating tumor cells and blood coagulation proteins have not been fully characterized. Activation of the bloods coagulation system has been associated with cancer, particularly metastatic cancer, for centuries [30]. The exact mechanism(s) underlying the activation of blood coagulation in cancer remain ill-defined [30, 45]. Tumor cell expression of tissue factor (TF) has been associated with advancing stages of cancer

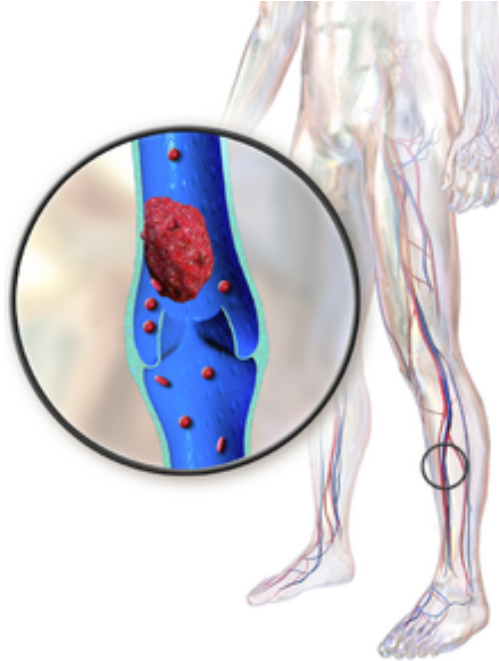


Figure 4.3: Schematic of deep vein thrombosis

Deep vein thrombosis is the medical condition where a blood clot has been formed in a large vein, typically in the legs. Symptoms include pain and swelling as blood builds up behind the clot.

progression, and has been shown to correlate with metastatic potential in vivo [2, 58, 59].

TF is a transmembrane glycoprotein that is normally expressed by cells outside of the blood vasculature. The exposure of blood to TF, as occurs in the event of a blood vessel injury, is a physiological initiator of coagulation [34, 61]. TF serves as the cell membrane receptor for and enzyme cofactor of coagulation factor VIIa (FVIIa). In complex, TF-FVIIa activates the extrinsic pathway of coagulation leading to the formation of thrombin which can then convert fibrinogen to fibrin in order to form a plug that stops bleeding at the injury site in order to maintain blood flow and volume.

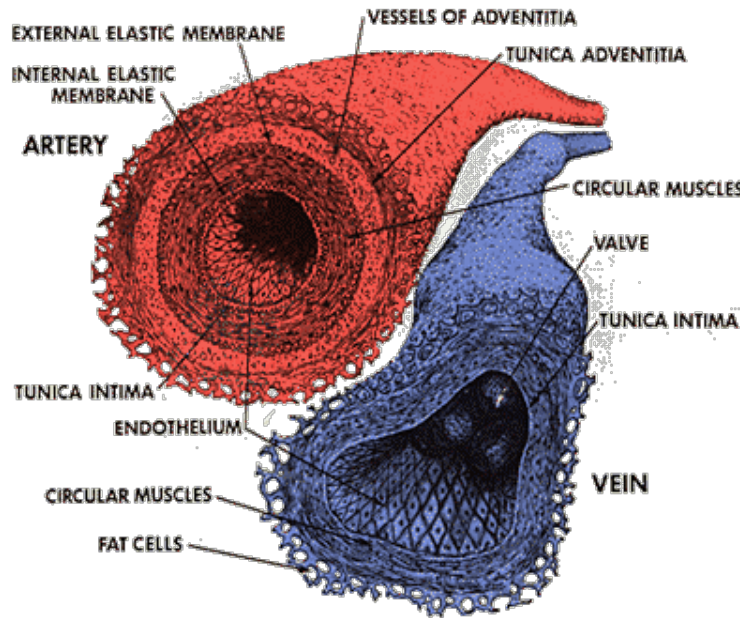


Figure 4.4: Schematic of artery vs. vein

Arteries and veins have different functions and different structures. Arteries carry oxygenated blood to various organs in the body, whereas veins carry deoxygenated blood back to the heart. Deep vein thrombosis occurs in the venous system, as opposed to the arterial system.

In the context of a metastasizing tumor cell, a TF-expressing circulating tumor cell (CTC) may expose blood within an uninjured blood vessel to TF [8, 45, 62, 74, 76]. Levels of intravascular TF correlate with cancer progression and to some extent with the formation of pathological clots or thrombi in the veins of patients with cancer. Thrombosis, the formation of pathological thrombi, accounts for the second leading cause of death for patients with cancer and constitutes a significant source of morbidity in these patients [76]. Anticoagulant measures taken after a thrombotic event are effective at reducing the formation of subsequent thrombi, but no current laboratory assay is capable of predicting which patients are at risk to develop thrombosis. The incidence of thrombosis is known to correlate with cancer type and

tissue of origin, suggesting that the cancerous cells themselves have a role in the formation of pathological thrombi [9]. In vitro, cancer cells are capable of independently initiating coagulation and clotting blood plasma. Similarly, functionally blocking TF on cancer cells prevents the cells ability to clot blood plasma. Therefore, mounting evidence suggests that cancer cell expressed TF is a likely culprit for the initiation of blood coagulation associated with cancer [8, 53, 54, 70, 80, 83].

The ability of TF to activate blood coagulation is dependent upon the presence of phospholipids, suggesting that only cell surface-expressed TF or cell membrane-derived TF bearing microvesicles are capable of activating coagulation [60]. This also indicates that the activation of coagulation by TF is essentially a surface phenomenon, requiring coagulation factors to transport from the blood to the surface-expressed TF in order to participate in coagulation. In vitro, the trafficking of soluble coagulation factors from bulk to a TF-expressing phospholipid surface is rate-limiting with respect to enzyme activation [31, 35, 56]. Further, TF activity is augmented in the presence of blood flow where convective transport supplants diffusive transport as the dominant mode of transport for coagulation factors to TF. Taken together, the ability for a TF-expressing CTC to activate blood coagulation is likely dependent upon its spatio-temporal relationship with the blood. In vitro, the coagulation kinetics for cancer cells in suspension is dependent upon the number of cells added to plasma [8, 74, 80, 83]. Further work has suggested that TF-expressing cells in suspension show synergistic effects on their ability to initiate and propagate coagulation, with the time to initiate coagulation enzymes and the rate at which these enzymes are generated correlating with the

average separation distance between cells rather than the overall cell count [74]. The effects of spatial separation on coagulation kinetics are consistent in assays that utilize closed systems under well-mixed conditions as well as open systems under laminar flow. However, a CTC would experience different flow regimes if it were circulating on the arterial side versus the venous side or if it were free-flowing or adherent to the cell wall, and the effects that these different conditions have on coagulation kinetics have not been established.

We model the concentration of thrombin generated by dispersed CTCs under laminar flow. Our model is based upon exact solutions used in the atmospheric dispersion community [72] whereby a source of pollution near the ground (i.e. a smokestack) emits a pollutant which enters the atmosphere and is dispersed and diffused downstream as a ‘Gaussian plume or a ‘Gaussian puff [72]. We adapt and use the solutions, which are based on a Greens function formulation for the concentration field equations [44], to model the dispersing and diffusing thrombin concentration field entering the blood. Since the concentration field equations are linear, we can superpose as many fields from each of the CTCs as needed. We assume that the transport of coagulation factors is diffusion-limited as viscous forces dominate inertial forces of the cells. Our results suggest that thrombin generated by a CTC collects at the blood vessel wall and correlates with the number and spatial distribution of CTCs in the blood, supporting a role for the CTC count in predicting risk for developing thrombosis. Modeling and simulation of coagulation processes has been performed [11, 15, 26, 27, 33, 51], but to

our knowledge, our work is the first to model the physiologically relevant scenario of a TF-expressing cell entering into and circulating within the bloodstream and simulate its effects on coagulation processes.

The clot formation model

5.1 Experimental methods

The set of experiments performed in the McCarty lab at Oregon Health Sciences University, Portland, were aimed at characterizing how the phenotype of tissue-factor carriers is related to procoagulant and prothrombotic activity, and specifically, how it is dependent on the carrier number, or density, of circulating tissue factor [8, 74]. The experimental setup is shown in Figure 5.1. Blood is placed in the upper chamber, and then it is allowed to flow through a collagen-lined capillary tube into the bottom chamber. When various concentrations of cells coated with tissue factor are introduced into the upper chamber, a blood clot forms within the order of minutes, and flow into the bottom chamber is occluded. The time for the blood solutions to occlude flow was recorded as the time to occlusion.

The experiment was performed with three different types of cells, otherwise known as TF carriers: TF-coated microspheres, a model cell line for lymphoma called U937 cells, and a metastatic breast cancer cell line called MDA-MB-231 cells. The cancer cells naturally

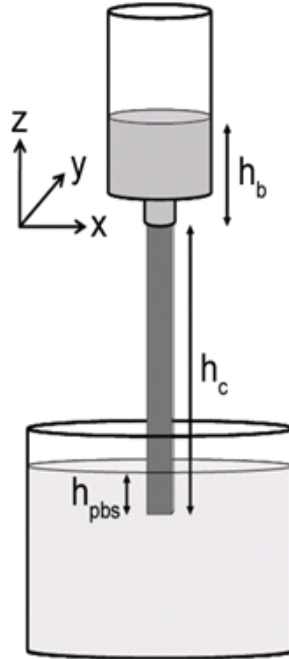


Figure 5.1: Experimental setup for blood occlusion

Blood in the upper chamber is allowed to flow into the bottom chamber. Once TF-carriers are introduced, a blood clot will form that occludes the flow of blood. h_b is the height of the blood in the upper chamber, h_c is the height of the capillary tube, and h_{pbs} is the height of the capillary tube submerged in the bottom chamber filled with phosphate buffered saline (PBS).

express tissue factor. The microspheres, however, were dipped into a tissue factor coating solution to allow for coating for 60 minutes at room temperature. The TF carriers were then analyzed on a FACSCaliber flow cytometer for carrier density before being placed into the experimental chamber.

Human monocytic U937 cells were purchased from ATCC (Manassas, VA). The metastatic adenocarcinoma cells, MDA-MB-231, were obtained from Dr. Tlsty (University of California, San Francisco, CA). Polymeric microspheres with a diameter of 9.86 micrometers (the size of human monocytes is approximately 7-10 micrometers in diameter) were purchased

from Bangs Laboratories (Fishers, IN). All blood donations from healthy human subjects were obtained in accordance with Oregon Health Sciences University's IRB approval.

The spatial separation, or the average distance between TF carriers in suspension, was obtained by calculating the cubic root of the volume of liquid divided by the number of TF carriers added. This approach assumes that TF carriers are uniformly distributed in suspension. The reported values represent the average value for a minimum of three experiments, and the data are reported as mean \pm standard error.

5.2 Experimental results

The three types of TF carriers: synthetic TF microspheres, U937 cells, and MDA-MB-231 cells, were found to be procoagulant in a carrier number- and TF-dependent manner. The experiments determined that the time to occlusion is linearly correlated with the spatial separation of TF carriers, as in Figure 5.2, and therefore, the addition of TF-expressing cells to blood plasma results in shortened clotting times in a cell concentration manner. The spatial separation of TF surfaces strongly correlates with procoagulant and prothrombotic activity. These results suggest that coagulation initiated by circulating tissue factor is kinetically limited by the mass transport of TF to the surfaces of cells, where the biochemical enzymes reactions occur. Also, the experimental results suggest the potential for circulating tissue factor to increase prothrombotic activity based solely on changes in spatial separation.

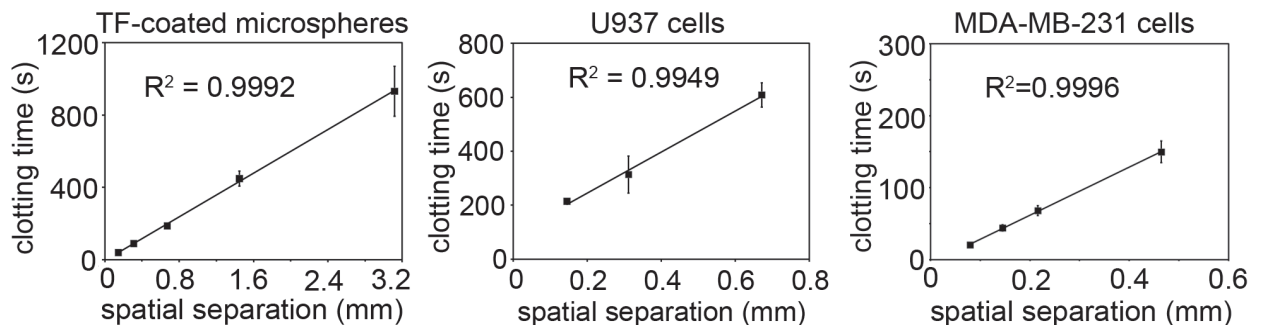


Figure 5.2: Experimental results comparing CTC burden with occlusion time. The three plots show a linear relationship between clotting time and the spatial separation of cells. R^2 is the coefficient of determination that provides a measure of the goodness of the linear fit. As R^2 approaches 1, the regression line perfectly fits the data. These plots show the results for experiments done with microspheres coated in tissue factor, a cell line for lymphoma, and a cell line for breast cancer.

5.3 Mathematical infrastructure and Green's functions approach

5.3.1 Fluid dynamics and concentration field equations

The computational model is based on the partial differential equations for the diffusing concentration field, coupled with the equations for incompressible fluid flow [44, 66]:

$$\frac{\partial \vec{C}^{(i)}}{\partial t} + \vec{u} \cdot \nabla \vec{C}^{(i)} = \alpha_i \Delta \vec{C}^{(i)} + \delta(\vec{x} - \vec{x}_i) \quad (5.1)$$

$$\dot{\vec{x}}_i = \vec{u} \quad (5.2)$$

$$\nabla \cdot \vec{u} = 0 \quad (5.3)$$

$$\rho \left(\frac{\partial \vec{u}}{\partial t} + \vec{u} \cdot \nabla \vec{u} \right) = -\nabla p + \mu \Delta \vec{u} \quad (5.4)$$

$$\vec{u}(\vec{x}, 0) = \vec{f}(\vec{x}) \quad (5.5)$$

Here, the concentration field associated with the i th species is denoted $\vec{C}^{(i)}(x, y, z; t)$, with diffusion coefficient α_i . The fluid (blood) velocity field is denoted by $\vec{u}(\vec{x}, t)$, blood pressure denoted p , density ρ , and each of the ' i ' CTCs ($i = 1, \dots, n$) are located at $\vec{x}_i(t)$, their time derivatives are denoted by the 'dot' superscript. δ in Equation 5.1 is the Dirac-delta function which is zero everywhere but where the argument is zero, which in this case are the locations of each of the CTCs. The initial locations of the CTCs are given by the function $f(x)$. The diffusion coefficient in Equation 5.4 is denoted by μ . Equation 5.4 are the Navier-Stokes equations representing the background plasma, which at this level of model

approximation we treat as an incompressible Newtonian fluid. The flow takes place in the upper-half space, above a solid wall which models the vessel wall, hence boundary conditions for the concentration field and blood velocity at the wall are:

$$\left. \frac{\partial \vec{C}}{\partial n} \right|_{wall} = 0 \quad (5.6)$$

$$\vec{u}|_{wall} = 0 \quad (5.7)$$

The first is a no penetration condition for the concentration field, while the second is the viscous no slip boundary condition at the wall.

5.3.2 The Green's function approach

In our models, the concentration fields are diffusing away from the CTCs, which are modeled as point particles propagating with the flow. The initial concentration that is emitted from the CTCs at initial time $t = 0$ is described by a Delta function. Therefore, we use the Green's functions solution to the advection-diffusion equation, (5.1). The Green's function, also called the fundamental solution, is the solution of a differential equation corresponding to the initial condition of an initial point source at a known position. More details on the derivation of Green's functions can be found in book by Duffy [24].

In this chapter, we focus on the simple geometry associated with the upper-half plane in 2D and upper-half space in 3D, making it possible to use an analytical Green's function

formulation to form solutions that satisfy exact boundary conditions. In 2D, with no flow ($u = 0$), we use the standard Green's function associated with the 2D diffusion equation [44]:

$$C^{(i)}(x, y; t) = \frac{\Gamma}{\sqrt{4\pi\nu t}} \exp\left(\frac{-(x - x_i)^2 - (y - y_i)^2}{4\nu t}\right) \quad (5.8)$$

$$C_{image}^{(i)}(x, y; t) = \frac{\Gamma}{\sqrt{4\pi\nu t}} \exp\left(\frac{-(x - x_i)^2 - (y + y_i)^2}{4\nu t}\right) \quad (5.9)$$

Here, each particle is placed in the upper-half plane ($y > 0$), at positions (x_i, y_i) for $i = 1, \dots, n$, and image particles are placed at $(x_i, -y_i)$. The no penetration condition Equation 5.6 for the concentration field at the wall is enforced exactly, with no other explicit boundary conditions needed.

For our three-dimensional model, we used an adapted form of the Gaussian plume model developed by Stockie [72]. Although the application he used is different from cancer cells in flow, atmospheric dispersion modeling is very useful for our purposes. Figure 5.3 shows a schematic of the Gaussian plume model, which models a contaminant plume emitted from a continuous point source. In our model, the CTCs are not continuously emitting tissue factor and are not in a stationary position like the chimney stack shown in Figure 5.3. Therefore, we use the Gaussian puff model, which takes into account these differences and more closely follows our model conditions, as opposed to the Gaussian plume model.

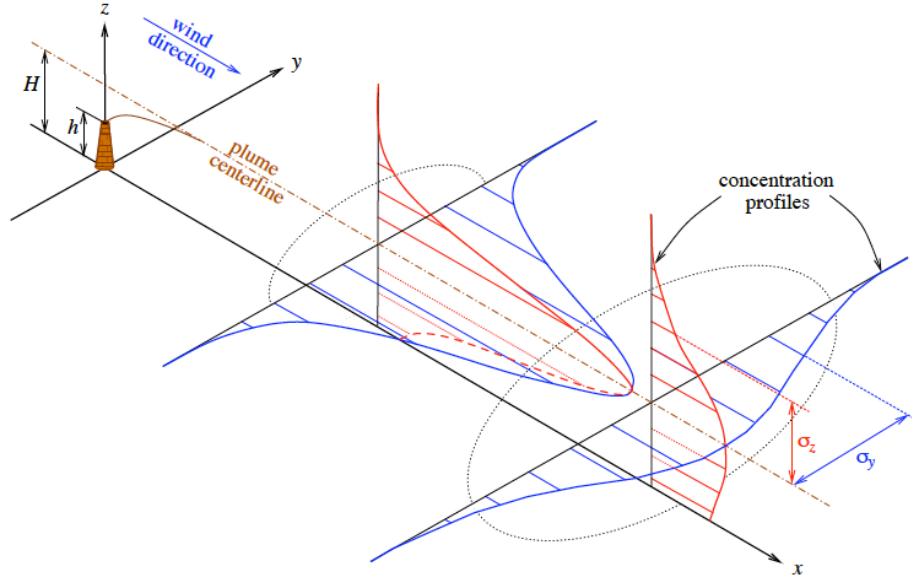


Figure 5.3: Schematic for atmospheric dispersion modeling

A contaminant plume emitted from a continuous point source, with the wind direction aligned with the x-axis. The Gaussian shapes of the plume cross-sections are shown.

In 3D, with flow $u = \text{constant}$, the corresponding Green's function is given by [44, 72]:

$$C(r, x_i, y_i, z_i; t) = \frac{Q_T}{8(\pi r)^{\frac{3}{2}}} \exp\left(-\frac{(x_i - ut)^2 + y_i^2}{4r}\right) \left[\exp\left(-\frac{(z_i - H)^2}{4r}\right) + \exp\left(-\frac{(z_i + H)^2}{4r}\right) \right] \quad (5.10)$$

Here, $r = \alpha x_i/u$ is a new scaled independent variable. The symbol Q_T expresses the total amount of thrombin expressed by the CTC. Using these solutions as the basic building blocks for flow simulations based on Equations 5.1 through 5.7, we are able to perform highly resolved concentration-flow simulations described in Section 'Results.'

5.3.3 Concentration field gradient tracking diagnostics

Since the concentration field is fairly complex, we need a diagnostic tool to help with visualization during a simulated run. It is useful to use what we call ‘passive gradient trackers,’ which are diagnostic particles placed in the flow. The gradient trackers do not disturb the flow, but move toward regions of high TF concentration and low TF concentration in time, as the simulation proceeds. A schematic of one of these trackers is shown in Figure 5.4. If the tracker is placed at position (x, y, z) at time ‘t,’ the concentration field at that point is given by $\vec{C}(x, y, z; t)$. The tracker then measures the concentration field at six neighboring points in the field: $\vec{C}(x \pm \epsilon, y \pm \epsilon, z \pm \epsilon)$, $0 < \epsilon \ll 1$, and measures the differences in concentration at these six points compared to the concentration at $\vec{C}(x, y, z; t)$. Thus, it measures the quantities $(\vec{C}(x + \epsilon, y, z; t) - \vec{C}(x, y, z; t))$, $(\vec{C}(x - \epsilon, y, z; t) - \vec{C}(x, y, z; t))$, $(\vec{C}(x, y + \epsilon, z; t) - \vec{C}(x, y, z; t))$, $(\vec{C}(x, y - \epsilon, z; t) - \vec{C}(x, y, z; t))$, $(\vec{C}(x, y, z + \epsilon; t) - \vec{C}(x, y, z; t))$, $(\vec{C}(x, y, z - \epsilon; t) - \vec{C}(x, y, z; t))$, and if it is seeking high concentration regions, it moves to the point yielding the largest increase in concentration. If it seeks low concentrations, it moves to the point yielding the largest decrease. Thus, it tracks ‘gradients’ in the concentration field at each time step, and as time evolves, the particles will gather in high or low TF concentration regions giving a useful visual diagnostic tool. For our simulations, we use ‘red’ trackers to follow increases in gradient, and ‘blue’ trackers to follow decreases. We note that there is an inherent timescale associated with the tracking, which is essentially governed by the size of ϵ . In the limit as this parameter goes to zero, the discrete trackers approximate derivatives in concentrations, hence gradients.

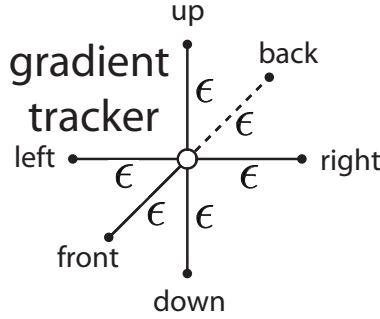


Figure 5.4: Schematic of gradient tracker

The gradient tracker ‘polls’ the chemical field concentrations in six directions, and then updates its position according to the greatest increase or decrease in concentration.

5.4 Simulation results

5.4.1 Two-dimensional concentration fields

A two-dimensional simulation of developing concentration gradients for 100 diffusing CTCs with no flow ($u = 0$) is shown in Figure 5.5. The top row in Figure 5.5 shows the concentration field at times $T = 1, 5, 15$ with $u = 0$ in Equation 5.1. The CTCs are randomly placed in the upper-half plane ($y > 0$), with the vessel wall at $y = 0$. On the vessel wall, we use the no penetration condition Equation 5.6 for the concentration field. No other explicit boundary conditions are needed when using the Green’s functions formulas. The middle row of Figure 5.5 shows the concentration profiles at $y = 0, 150, 300$, while the bottom row shows the 3D surface plots of the concentration fields in the (x, y) plane. The CTCs are placed in the region $y > 0$, while their images are placed appropriately at $y < 0$ (see Equations 5.8 and 5.9) so that boundary conditions are enforced. The (dimensionless) diffusion coefficient

for each particle is taken to be $\alpha_i = 1.5$. We note that here, and in all of the following simulations, equations, and parameters are to be interpreted non-dimensionally since explicit comparisons with *in vivo* experiments are not described in this dissertation.

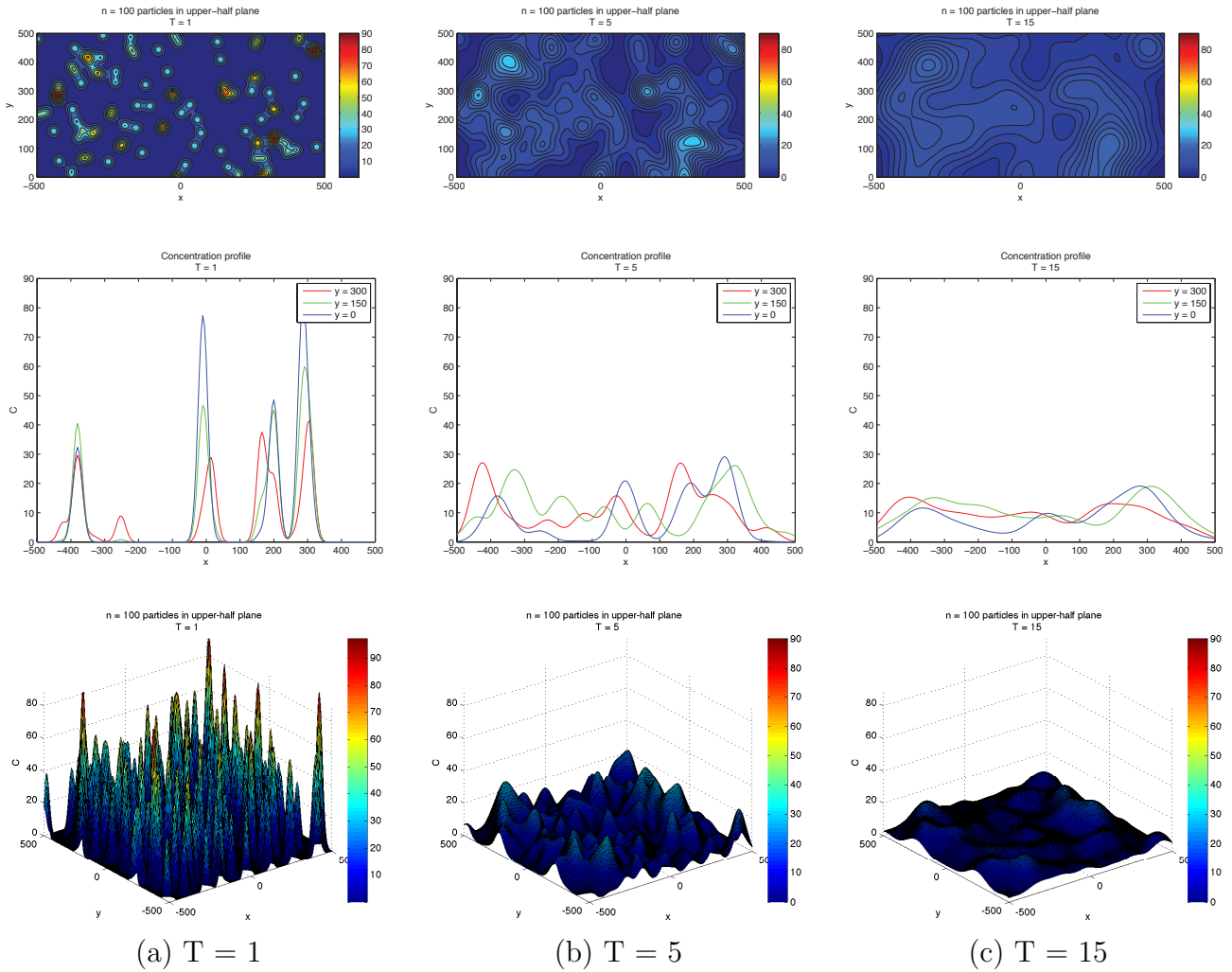


Figure 5.5: 2D simulation results for $n = 100$ cells
 2D results for 100 cells with no flow, $\vec{u} = 0$, at three times in the simulation. The first row shows the evolving concentration fields at times $T = 1, 5$, and 15 . The second row shows the concentration profile at different slices along the y -direction, at $y = 0, 150$, and 300 . Note that the blood vessel wall is at $y = 0$. The third row shows the 3D contour plot of the concentration fields and gives a sense of how much the concentration diffuses away as time progresses.

The 2D simulations with no flow clearly show the diffusing fields from each particle merging and smoothing over time, with concentration persisting at the vessel wall because of the no penetration boundary condition. This is seen most clearly in Figure 5.6 which shows the concentration profile for $T = 500$ at $y = 0, 150, 300$. Figure 5.6(a) shows the persistence of the highest concentration at the wall ($y = 0$). Figure 5.6(b) shows the peak concentration at $y = 0, 150, 300$ as time progresses. The vertical line in this figure separates two distinct temporal regimes: (i) $0 < T < 3$; (ii) $T > 3$. The first early regime represents a ‘rapid mixing’ regime where the concentration fields quickly merge to form a complex combined overlap domain of fields associated with the different sources merging together. The ‘long-time’ regime ($T > 3$) shows that the peak combined concentration field continues to decay, but rather slowly, with the peak wall concentration ($y = 0$) dominating.

5.4.2 Three-dimensional concentration fields

We next performed a high resolution (exact, since we are using the Green’s function formulation) simulation of CTCs in three- dimensions with a constant flow velocity profile ($u = \text{constant}$). Figure 5.7 shows the general schematic diagram with flow only in the direction of x , with diffusing CTCs initially placed in the domain at random heights $z = H_1, H_2, H_3$. The vessel wall in these simulations is located at $z = 0$. Because the concentration fields are spatially complex and time-dependent, we build in particle gradient tracking capability in our code, also shown schematically in Figure 5.7.

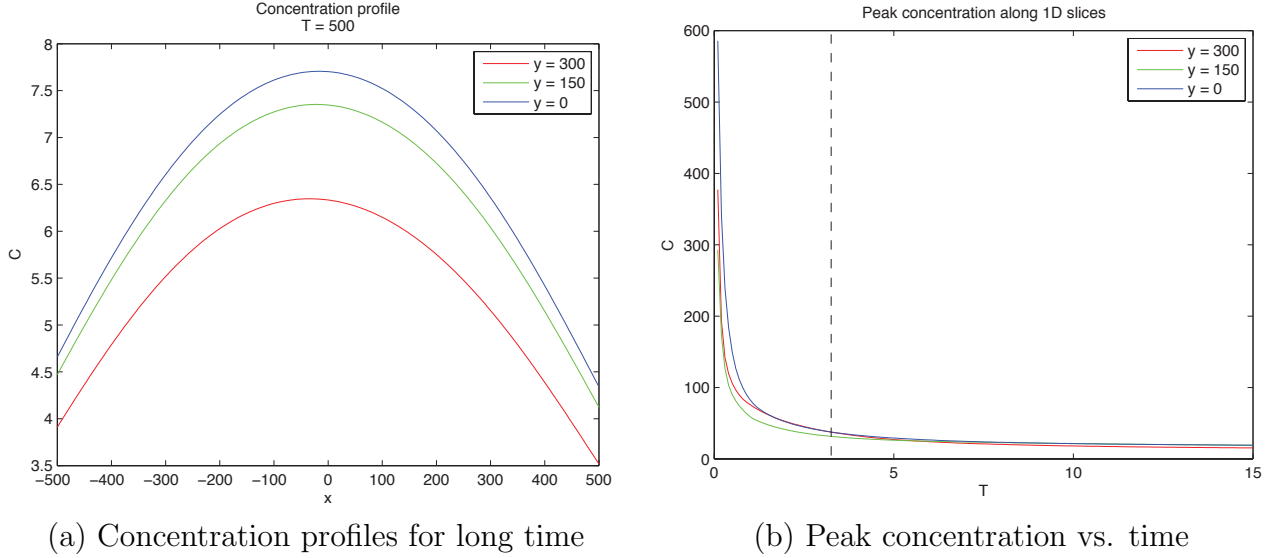


Figure 5.6: Long-time 2D simulation results for $n = 100$ cells

(a) Concentration profiles at various y -slices. After a long time, the concentration at the wall is greater than anywhere else in the semi-infinite plane. (b) Peak concentration vs. time. There are two time regimes involved in this simulation. First, a short time region up to about $T = 3$ represents the fast mixing period of the concentration fields. Then, after the vertical dashed line, the concentration fields decrease much slower and decay very slowly, showing that in the long time region, the fields of TF have mixed and are slowly diffusing away.

Next, we performed a 3D concentration field simulation (without gradient trackers) using four CTCs, where we show a top down z -projection view of the (x, y) plane for values $z = 0$ (wall), $z = 45$, and $z = 90$, progressively in time $T = 1, 10, 40, 75$ in Figure 5.8. In order to compare with the 2D simulations, we have chosen the same dimensionless diffusion coefficient values $\alpha_i = 1.5$. For these simulations, the initial locations of the four CTCs are $(x_i, y_i, z_i) = (300, 300, 45); (180, 400, 30); (300, 100, 30); (275, 200, 60)$, as shown in Figure 5.9. Careful examination of the coloring of the fields indicates (i) the persistence of the strongest concentration region near the wall, (ii) strong concentrations in overlap domains from different CTCs, and (iii) strong concentrations near each of the CTCs which express

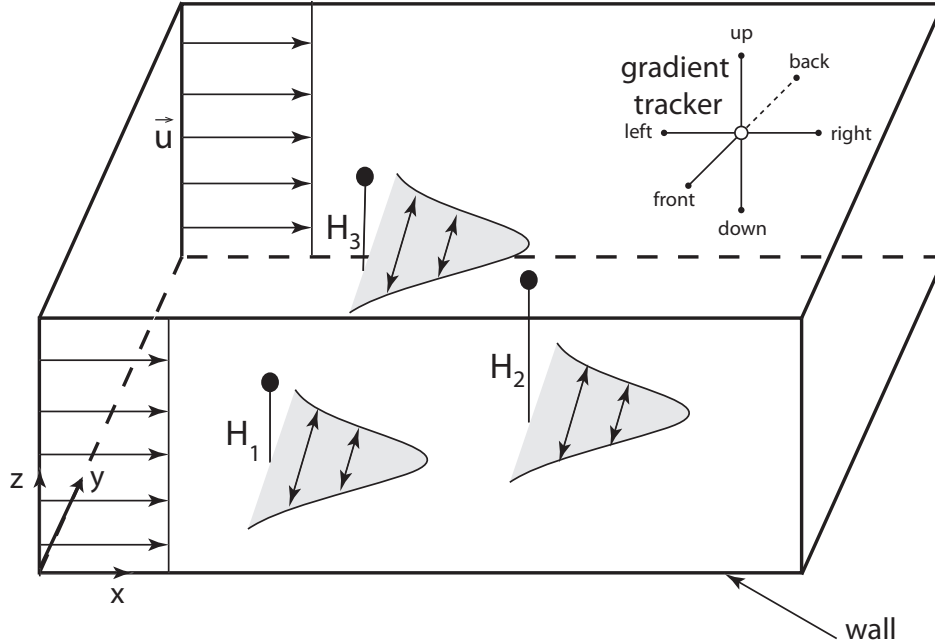


Figure 5.7: Computational domain for 3D model of diffusing cells
 3D computation domain with a bottom blood vessel wall. CTCs are placed at random initial positions and travel with the fluid flow, which is constant in the x -direction. The concentration fields diffuse away as ‘puffs’, not plumes, according to the experiment with synthetic TF microspheres. In the upper right-hand corner of the domain, we indicate the six directions that the gradient is ‘polled’ for the gradient tracker calculations.

TF. These numbers and results are consistent with the experiment described in [74] in which small numbers of TF-coated micro-spheres were placed in blood solution and clotting time was carefully measured. Typically, in metastatic patients, measured numbers of CTCs would be in the range of 1 – 100 CTCs/ml.

For a direct comparison with the 2D results, we show in Figure 5.10 the 3D concentration field simulations using 100 CTCs placed randomly (initially). The overall concentration field again persists near the wall, but the overall concentration field level is higher, roughly increasing linearly with the number of CTCs in the flow, also in agreement with results

from [74]. As the flow progresses in time, flow visualization tools become crucial to help understand the field patterns that develop.

5.4.3 Gradient tracking results

Circulating tumor cells and other biological cells in the body have the capability to follow chemical gradients in the blood or other fluid environment. This phenomenon, called chemotaxis, is an especially important ability that allows cancer cells to detect certain biochemical agents or enzymes in the blood and direct their movements toward or away from them [68]. To track developing TF concentration gradient patterns, we include gradient tracking capability to our simulation. Figure 5.11 illustrates different time points ($T = 8 - 220$ s) as the flow progresses. The red particles move toward regions of high CTC concentration, whereas the blue move to regions of low CTC concentration. The patterns that develop with the red and blue particles depend on the comparison of relative timescales as determined by the concentration field diffusion rates, α_i , as well as the timescales on which the gradient trackers move. The first three panels in the figure clearly show the red gradient trackers gathering in highly concentrated regions near each of the CTCs, lining up in elongated columnar strands. The timescale in which these trackers locate the diffusing CTCs is short compared with the timescales on which the diffusion fields spread. The last two figures in the panel show the particles then moving toward the vessel wall where concentration fields persist. This movement of the trackers to the vessel walls takes place on a longer timescale, well after the CTCs have been located in the flow.

Gradient tracking confirms our simulation result of the diffusion of tissue factor collecting at the vessel wall, which is also supported by experiments and numerical models performed by Haynes et al. [37]. Prothrombin species were generated at increasing shear rates, and they examined the dilutional effects of variations with shear rate. Their model results validate that there is little diffusion away from the wall region. The hypothesis that clot formation can only occur in a relatively small region close to the vessel walls has been previously suggested by Fogelson's numerical modeling studies of coagulation under flow, and it is also supported by our computational model.

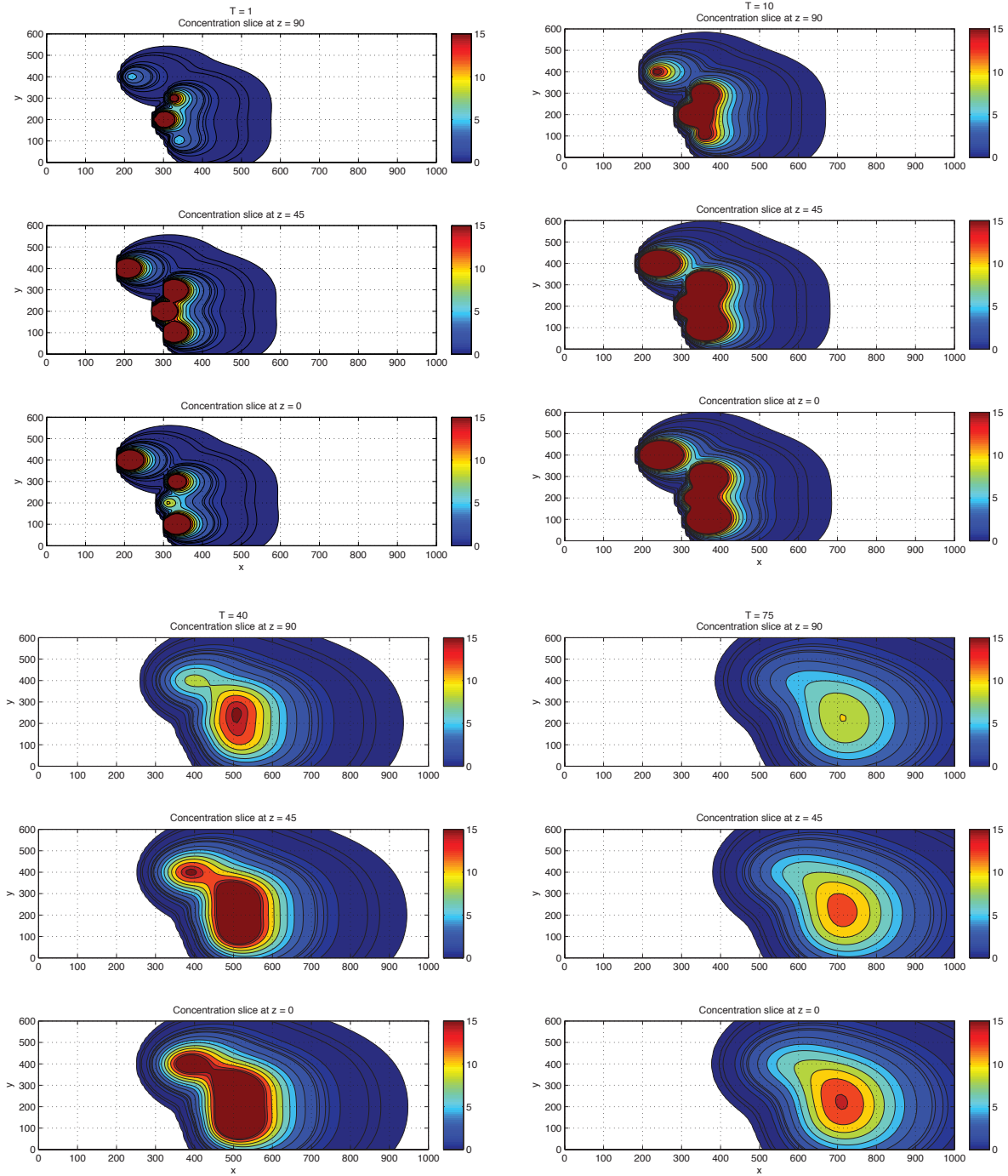


Figure 5.8: 3D simulation results for $n = 4$ cells

Top-down view of the x - y plane, with four CTCs randomly placed and in flow with the blood. There are three different z -slices at $z = 0$ (the wall), $z = 45$ (the source height), and $z = 90$ (above the source). The concentration builds up near the wall and is highest near the wall and in the complex over-lap regions where the concentration fields have mixed together.

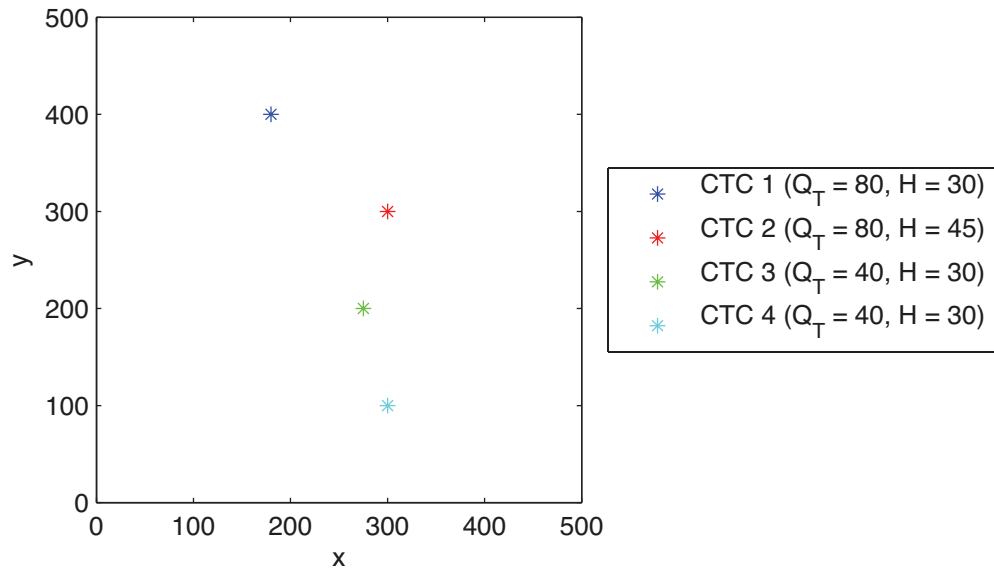


Figure 5.9: Initial positions and concentration levels for 3D simulation
 Top-down view of the x - y plane, with four CTCs randomly placed. The initial positions, $(x_i, y_i, z_i = H)$, and the total concentration emitted, Q_T , are as follows:

- CTC 1: $(180, 400, 30)$, $Q_T = 80$;
- CTC 2: $(300, 300, 45)$, $Q_T = 80$;
- CTC 3: $(275, 200, 30)$, $Q_T = 40$;
- CTC 4: $(300, 100, 30)$, $Q_T = 40$.

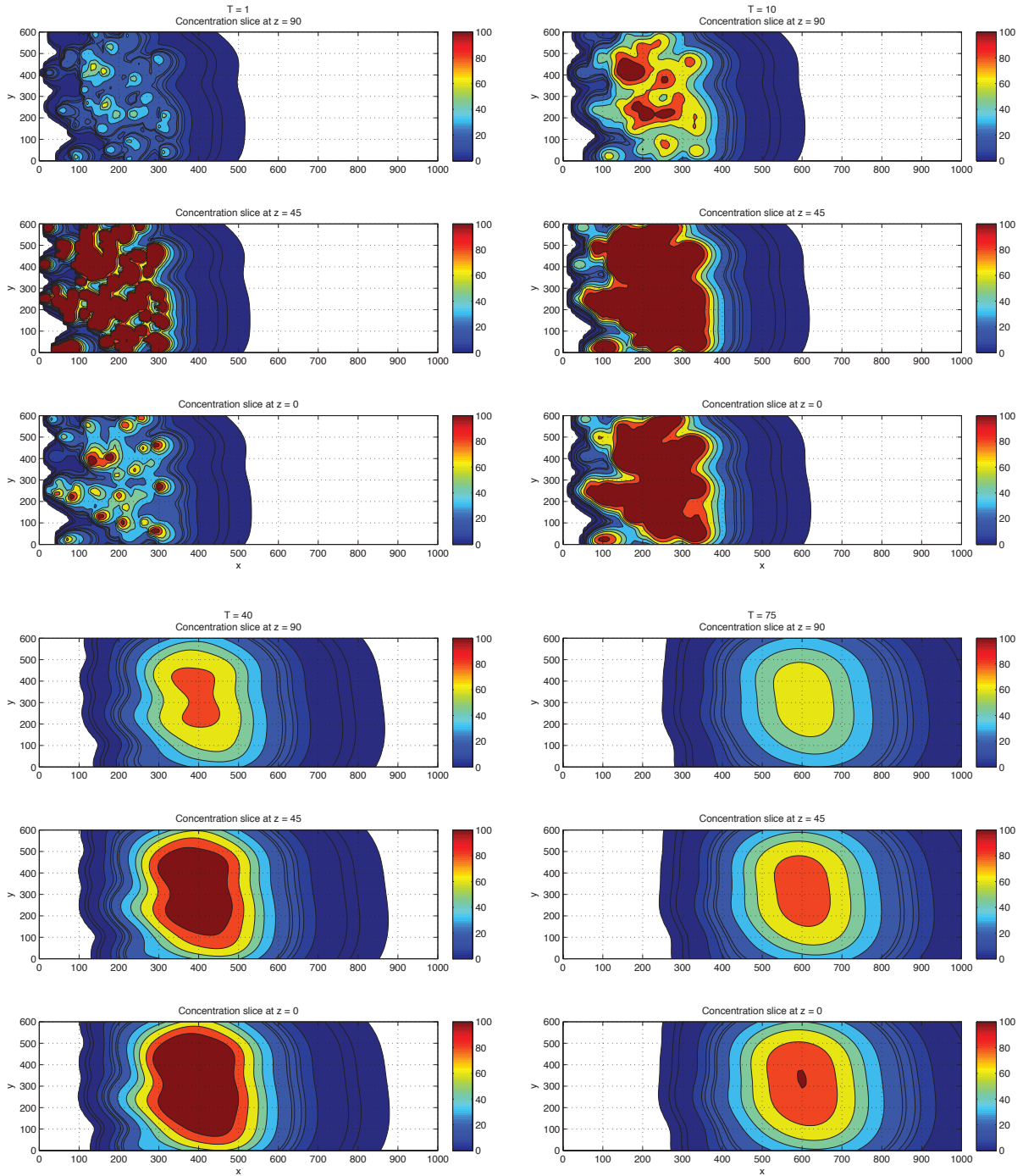


Figure 5.10: 3D simulation results for $n = 100$ cells

Top-down view of the x - y plane, with 100 CTCs randomly placed and in flow with the blood. There are three different z -slices at $z = 0$ (the wall), $z = 45$ (the source height), and $z = 90$ (above the source). The concentration builds up near the wall and is highest near the wall and in the complex over-lap regions where the concentration fields have mixed together.

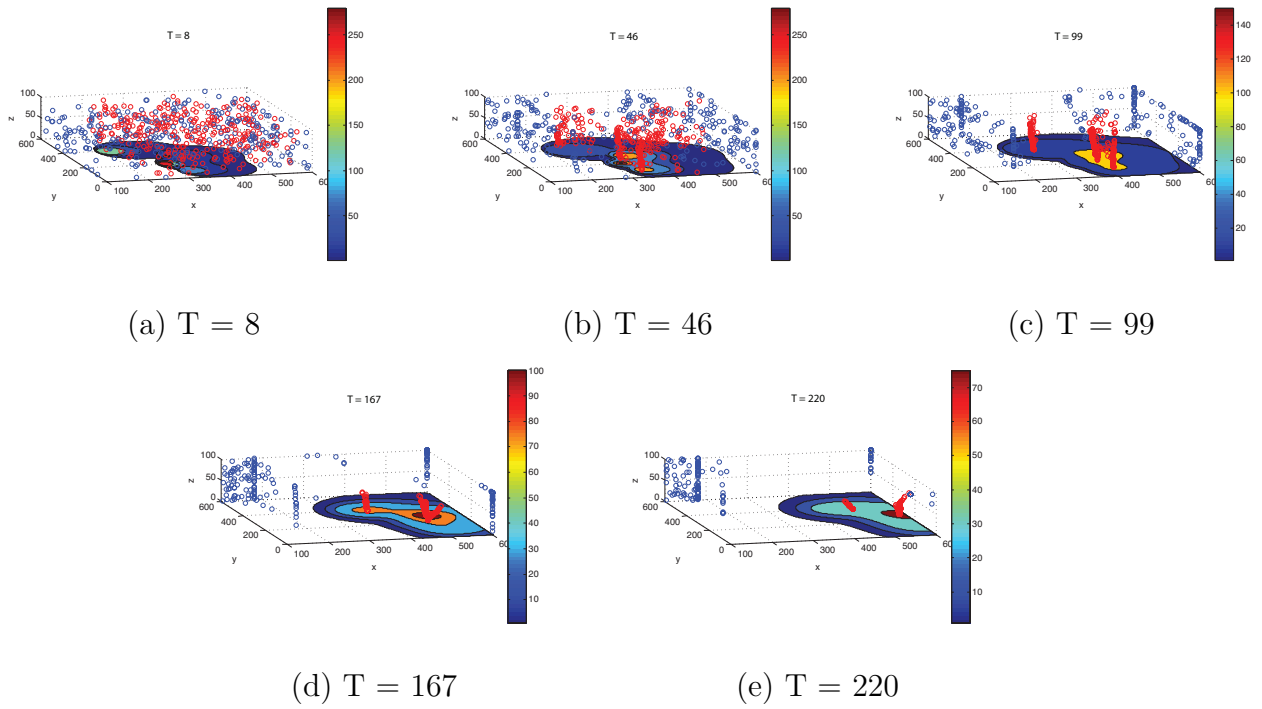


Figure 5.11: Chemical field gradient tracking simulation

This simulation takes the 3D results from Figure 5.8 and displays a 3D view with red and blue gradient trackers that track increasing and decreasing concentration fields, respectively. The five panels show the simulation at times $T = 8, 46, 99, 167,$ and 220 s.

The fibrin formation model

6.1 Experimental methods and results

A novel experiment was developed to observe fibrin formation by a colon cancer cell line, SW480. The cancer cell(s) were allowed to attach to a substrate in a glass chamber, and then coagulation factors were introduced in the chamber. As the coagulation reactions occurred, the end product of clot fibers, or fibrin, are visible. A fibrin front can be observed, as the fibrin strands propagate radially outwards from the cancer cell, and the fibers get denser as the experiment progresses. It is important to note that the experiment is performed under no flow conditions. Figure 6.1 shows an experimental run of one colon cancer cell at several time points. This single cell clotting assay reveals that cancer cells nucleate blood clots. The cell is approximately 12 microns in diameter, and the experimental images are produced with DIC microscopy imaging techniques. Both the experiments and microscopy are performed by the McCarty Lab at Oregon Health and Science University.

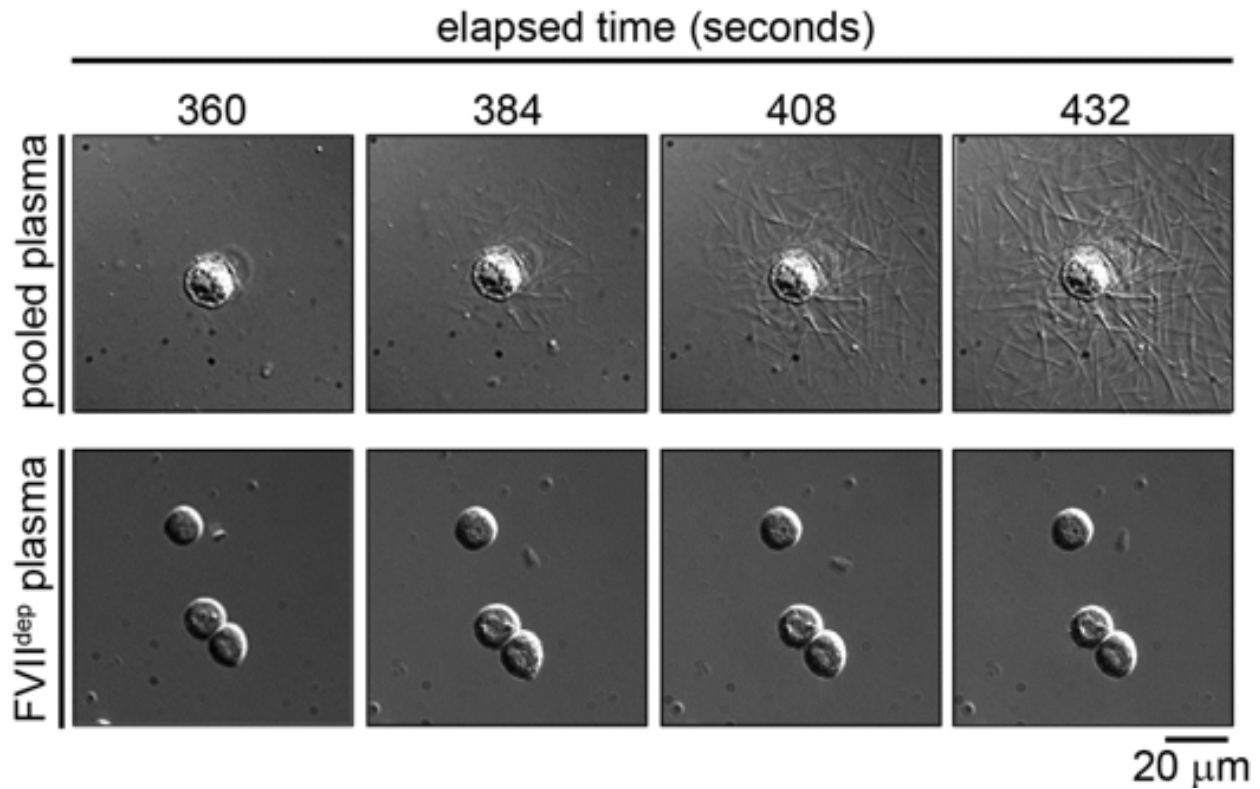


Figure 6.1: Single cell clotting assay experiment

Time lapse microscopy of fibrin formation by SW480 colon adenocarcinoma cells immobilized onto a silanized glass surface, immersed in plasma under conditions of coagulation for (top row) pooled plasma and (bottom row) coagulation factor VII-depleted plasma.

6.2 Model in a closed circular domain

This series of experiments set the stage for the development of a model of fibrin formation in a closed circular domain, in which there is no flow. Our model was based on the experiments described above. Again, the cancer cell is modeled as a point source, with a concentration field of thrombin diffusing out from the initial position of the cell. This time, the concentration field builds up more quickly at the circular vessel wall and persists for a longer period of time than in the semi-infinite domain. Our mathematical model is based on

the exact solutions found using the Green's function formulation, this time however, in polar coordinates. The advection-diffusion equation in polar coordinates with no flow is written as the two dimensional heat equation:

$$\frac{\partial g}{\partial t} - \kappa \left(\frac{\partial^2 g}{\partial r^2} + \frac{1}{r} \frac{\partial g}{\partial r} + \frac{1}{r^2} \frac{\partial^2 g}{\partial \theta^2} \right) = \frac{\delta(r - \rho)\delta(\theta - \theta')\delta(t)}{2\pi r} \quad (6.1)$$

with g representing the Green's function, κ is the diffusion constant, ρ is the initial position along the radius r , θ' is the initial angle where $\theta = 0$ is along the positive x axis, and t is time for the region inside the circle $0 \leq r < a$. The boundary conditions are the Neumann boundary conditions at the circular wall (no penetration condition), and the Green's function solution is a series of Fourier-Bessel functions, also known as Dini series:

$$g = \frac{1}{\pi a^2} \sum_{m=-\infty}^{m=\infty} \sum_{n=1}^{n=\infty} \frac{J_m(\alpha_n r) J_m(\alpha_n \rho)}{\left(1 - \frac{m^2}{\alpha_n a^2}\right) J_m^2(\alpha_n a) + J_m'^2(\alpha_n a)} \cos[m(\theta - \theta')] e^{-\kappa \alpha_n^2 t} \quad (6.2)$$

where α_n is the n th positive root of $J_m'(\alpha_n a) = 0$. Some identities which are useful in simplifying the Green's function solution are as follows:

$$J_m'(z) = \frac{1}{2} [J_{m-1}(z) - J_{m+1}(z)] \quad (6.3)$$

$$J_0'(z) = -J_1(z) \quad (6.4)$$

Figure 6.2 shows a 2D simulation with five randomly placed CTCs in a circular domain in no flow conditions, showing the surface plots and contour plots at 3 different times ($T =$

0.4, 1.5, 3 s). The five CTCs have different diffusion constants, and one can see that the concentration field of thrombin is highest at the source locations, in complicated overlap regions, and persists for longer times at the wall. This simulation is significant in showing what the concentration of thrombin fields may look like in parts of the circulatory system where thrombin fields may build up due to minimized blood flow, for example, in situations where blood flow is restricted by a growing clot or a cluster of cells.

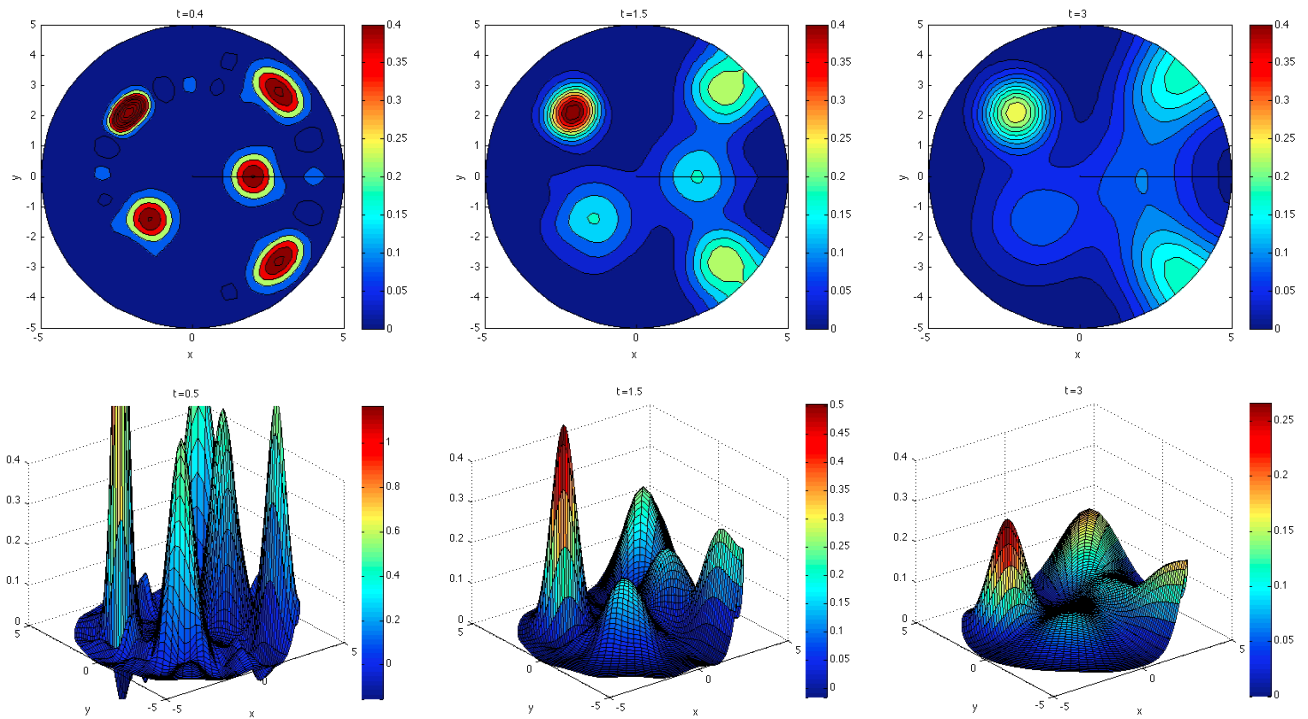


Figure 6.2: 2D simulation of CTCs in a circular blood vessel with no blood flow. Five cancer cells that are represented as point particles are placed randomly in a closed circular domain. The concentration field is shown as a contour plot in the top row and also as a surface plot in the bottom row. The frames shown are at $T = 0.4, 1.5,$ and 3 s.

The next two sets of figures (Figure 6.3 and Figure 6.4) show the evolving thrombin fields with two CTCs having the same diffusion constant. Figure 6.3 has two CTCs placed near the

center of the circular domain, and Figure 6.4 has two CTCs placed near the wall of the circular domain. We included a propagating radial diffusion front based on a constant concentration assumption inside the growing ring, which leads to the approximation of Equation 6.5

$$r(t) \sim \sqrt{\kappa t} \tag{6.5}$$

where r is the radius of the growing ring, κ is the diffusion constant, and t is time. We also placed white gradient trackers that follow high concentration fields of thrombin, as in Chapter 5, using the nearest neighbor polling technique. The white trackers are randomly placed initially near the location of the two CTCs. For the CTCs in the center, they are placed in a smaller co-centric circle with a radius that is half of that of the circular domain, and for the CTCs near the wall, the trackers are placed in a wedge-like manner of the circular domain that spans an angle of $\pi/2$. As the white gradient trackers move to high concentration zones, they effectively build fibrinogen bridges, which are composed of the fibrins displayed in the experiments of fibrin formation described earlier in this chapter.

Upon performing these simulations based on exact analytical Green's functions solutions for the concentration field of point particles in a closed domain, we then developed finite element models that employ nonlinear time difference schemes to solve more complex flow conditions and blood vessel geometries, even including a deformable boundary for the CTCs. We use the exact thrombin field results obtained in this chapter as test models, as a tool for comparison, for the finite element CFD models discussed in the following chapter.

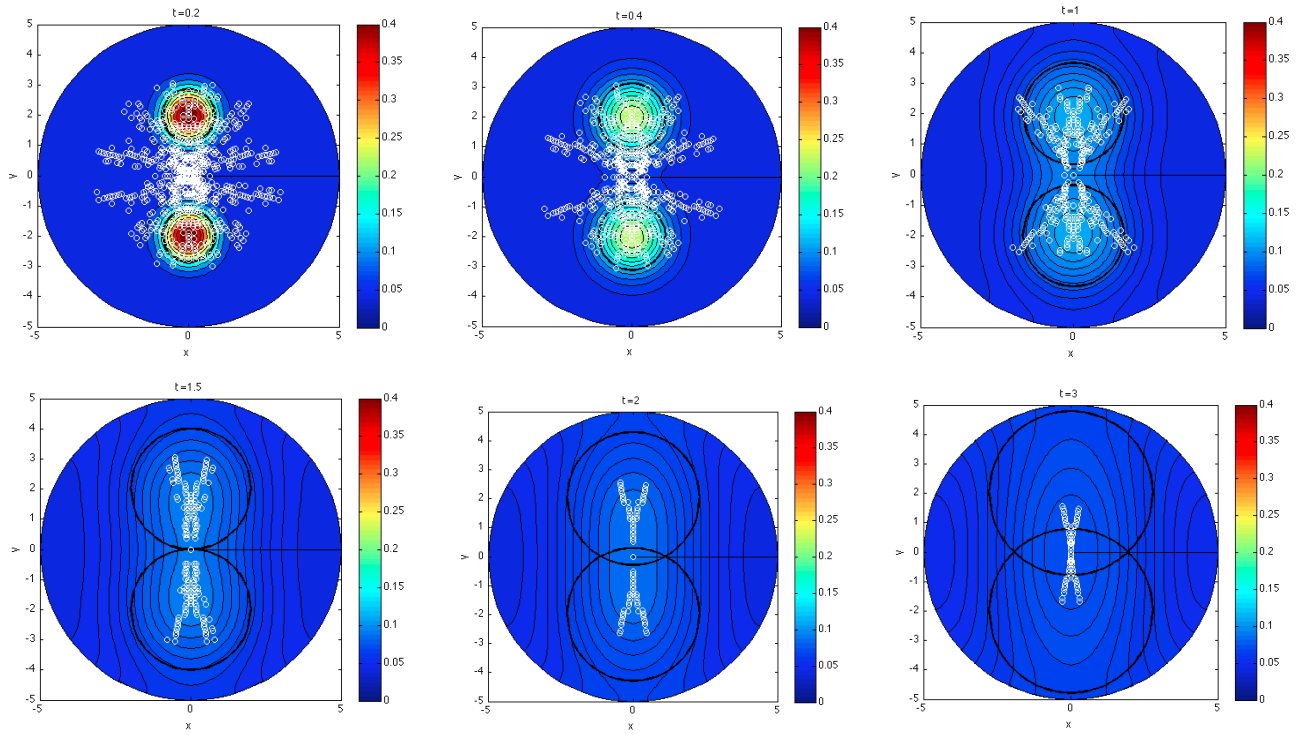


Figure 6.3: Fibrinogen bridge simulation with two cells near center of vessel
 Two cancer cells that are represented as point particles are placed near the center of a closed circular domain. The concentration field is shown with the diffusion front demarcated by a thick black line. White gradient trackers highlight the fibrinogen bridge formation as time progresses. The frames shown are at $T = 0.2, 0.4, 1, 1.5, 2,$ and 3 s.

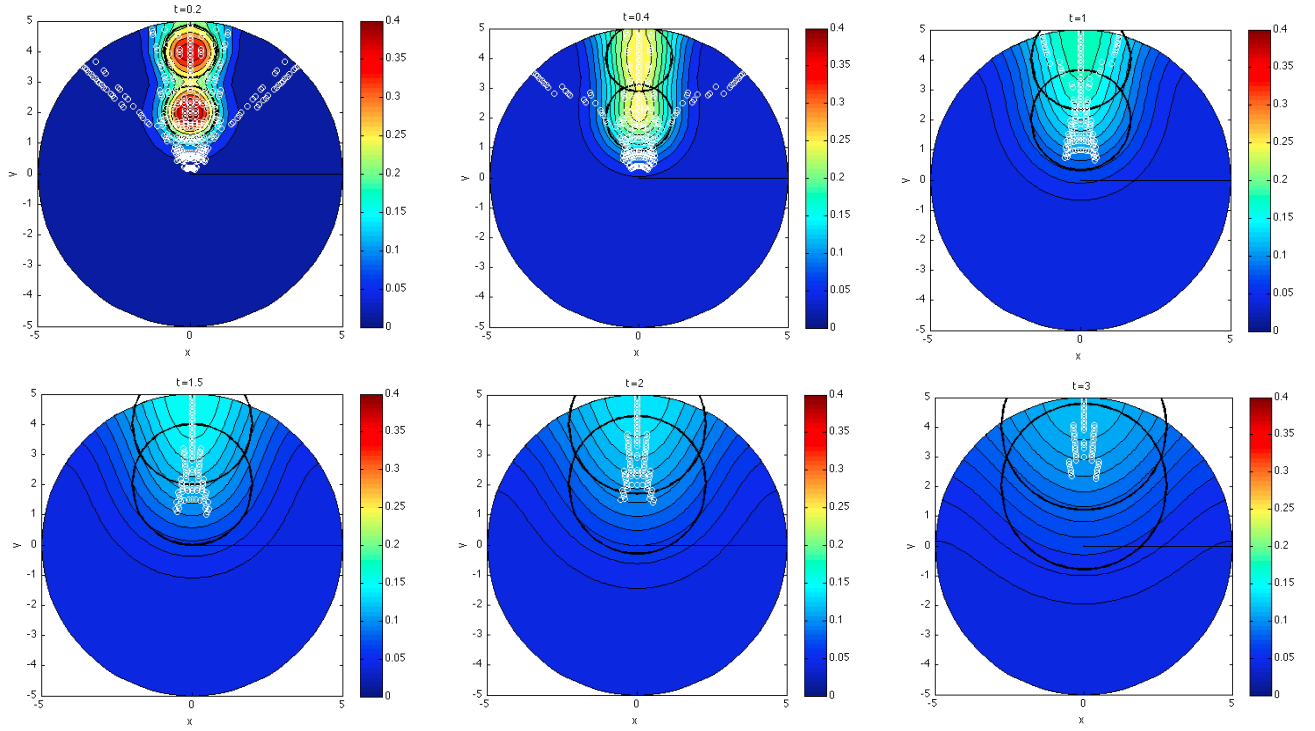


Figure 6.4: Fibrinogen bridge simulation with two cells near circular wall of vessel
 Two cancer cells that are represented as point particles are placed near the vessel wall of a closed circular domain. The concentration field is shown with the diffusion front demarcated by a thick black line. White gradient trackers highlight the fibrinogen bridge formation as time progresses. The frames shown are at $T = 0.2, 0.4, 1, 1.5, 2,$ and 3 s.

The computational fluid dynamics models

Our mathematical models of CTCs and their respective thrombin fields involving both non-constant blood flow and more complicated geometries than the simple cases of a semi-infinite plane and circular domain, as we examined earlier, require computational tools such as finite element analysis and computational fluid dynamics techniques. This is due to the fact that analytical solutions do not exist for the advection-diffusion equation in these complex problems. Therefore, to create flow models where the dynamics of the CTCs and the chemical gradient fields are acting in response to the flow in addition to one another in the flow, we build computational models using COMSOL Multiphysics (Version 4.3b), which is a finite element analysis (FEA) software package. The CFD (computational fluid dynamics) model is developed using finite element analysis to solve the partial differential equations (Equation 7.6) and to maintain boundary conditions on the cell surface and the blood vessel walls.

Components in blood	Density
Platelets	150 – 400 million /mL
Red blood cells	4 – 5 million /mL
White blood cells	4,500 – 10,000 /mL
CTCs	2 – 100 /mL

Table 7.1: Components in the bloodstream with their densities.

7.1 Development of the model from patient samples to computational simulation

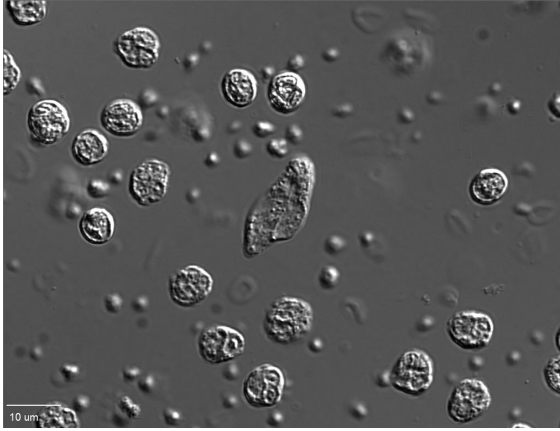
Fluid biopsy samples are drawn from patients diagnosed with cancers of the breast, lung and colon at the Scripps Medical Hospital in La Jolla, California. Dr. Peter Kuhn’s Lab at The Scripps Research Institute processes these blood samples, and the HD-CTCs (high definition circulating tumor cells) are run through cell assays, stained and cultured, so that they can be processed through the system identification modules in the Kuhn Lab [17, 47, 55]. CTCs are deemed an extremely rare event, even in highly metastatic patients, as the number of CTCs found in the blood is in the range of 2 – 200/mL. As a point of reference, the number of platelets is 150 – 400 million/mL. Table 7.1 gives the average counts of the various particles found in the bloodstream of a cancer patient.

Once the CTCs are identified, the blood samples are then sent to be imaged and characterized at OHSU by Dr. Owen McCarty’s Lab. These samples are imaged using DIC

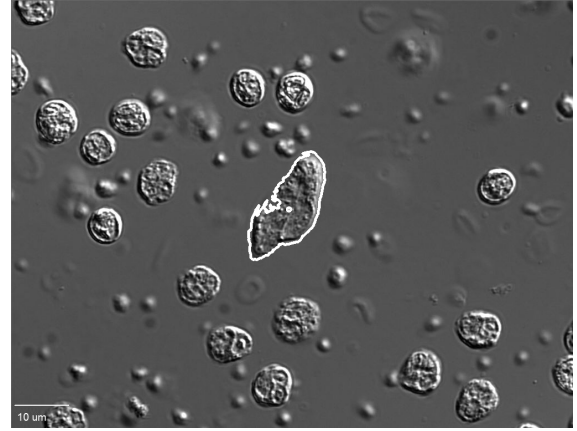
microscopy as shown in Figure 7.1(a), and various cell parameters were determined, which include cell density, mass, volume, and area. We then take the DIC images and the cell metrics as inputs into our computational models. In order to accurately demarcate the boundary of the cancer cells and clusters of cells, we use a program called CellProfiler, which obtains the outline of the cell in white and also identifies the center of the outline as a white dot, both shown in Figure 7.1(b). CellProfiler is widely used as an image processing tool to identify and characterize images of biological cells and organisms. The shape of the cell or cluster from CellProfiler is then generated in our computational domain created in COMSOL Multiphysics, shown in Figure 7.1(c). The inside of the cell and the surrounding fluid outside the cell are discretized into triangular mesh elements, where the fluid physics are solved at the grid points. Lastly, the cell or cluster is placed in a blood vessel, either a channel flow blood vessel or a branching blood vessel, as in Figure 7.1(d).

7.2 Description of the mathematics and multiphysics used in COMSOL models

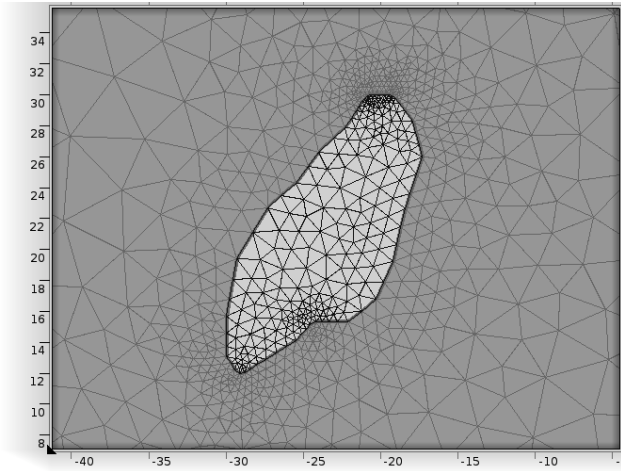
COMSOL Multiphysics is a finite element analysis solver and simulation package for various engineering and physics applications, particularly for coupled phenomena, otherwise known as multiphysics. The specific modules within COMSOL that we utilized for our models include the Microfluidics Module and the Particle Tracing Module. The physics that are



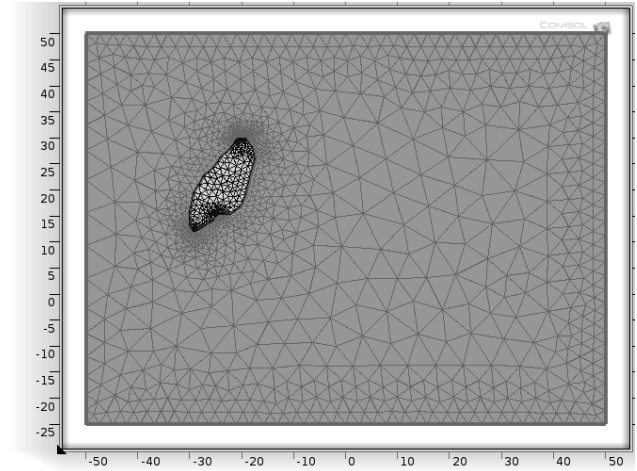
(a) DIC image of cancer cell



(b) Outline of cell from Cell Profiler



(c) Shape of cell generated in mesh



(d) Cell placed in a channel venule

Figure 7.1: Development from patient sample to computational simulation

The fluid biopsy is sampled from patient, in this case a breast cancer patient, and then (a) imaged using DIC microscopy. CellProfiler (b) outlines the shape of the cell, which is (c) generated as a mesh using COMSOL. Lastly, (d) the cell is placed in the computational domain, which in this simulation, is a channel venule.

coupled in our model include fluid flow, chemical species transport, and particle tracing, which will be described in detail below.

7.2.1 Laminar two-phase flow with moving mesh

The blood flow velocity field is described by the full Navier-Stokes equations

$$\rho\left(\frac{\partial \vec{u}}{\partial t} + \vec{u} \cdot \nabla \vec{u}\right) = -\nabla p + \mu \Delta \vec{u} \quad (7.1)$$

$$\nabla \cdot \vec{u} = 0 \quad (7.2)$$

$$\vec{u}(\vec{x}, 0) = \vec{f}(\vec{x}), \quad (7.3)$$

where u is the blood velocity, p is the pressure, ρ is the blood density, and μ is the dynamic viscosity. We use the values of density and dynamic viscosity found in literature of whole blood at body temperature of $37^\circ\text{C} = 310\text{K}$, which are $\rho = 1060 \text{ kg/m}^3$ and $\mu = 3 \times 10^{-3} \text{ Pa} \cdot \text{s}$. We also assume the blood is Newtonian and incompressible, which is theoretically valid at the flow conditions we are modeling in the venous system of the circulatory system. The blood flow assumes a parabolic flow profile (Poiseuille flow) at the inlet. The flow profile is set up by a pressure gradient between the inflow and the outflow. The boundary conditions at the blood vessel walls are the viscous no-slip conditions, and at the cell wall, the velocity of the blood is equal to the velocity of the cell boundary.

$$\vec{u}|_{\text{wall}} = 0 \quad (7.4)$$

$$\vec{u}|_{\text{cell}} = \text{velocity of cell boundary} \quad (7.5)$$

Vessel	Diameter	Velocity (cm s ⁻¹)
Vena cava	~ 1 cm	~ 10 ¹
Veins	2 – 9 mm	~ 10 ⁰
Venules	7 – 50 μm	~ 10 ⁻¹
Capillaries	~ 1 μm	~ 10 ⁻²

Table 7.2: Velocities of vessels of different sizes in the venous system.

As stated in the Introduction to Part II, we are studying the incidence of blood clotting in cancer patients that occur in the venous system, as opposed to the arterial system. Table 7.2 gives a list of the different types of blood vessels in the venous system, with the vena cava having the largest diameter size and capillaries having the smallest. The typical velocities (listed as an order of magnitude in cm/s) are also given, with the vena cava having the fastest velocity and capillaries the slowest. In our models and simulations, we use diameters that are typically found in venules, and therefore, the blood velocity is also on the order of 10⁻¹ cm/s, in order to be as physiologically relevant as possible.

The fluid flow physics we specify in our model is a laminar two-phase flow, which models the laminar flow of two immiscible fluids. The velocity field, pressure, and mesh deformation are solved for, and a moving triangular mesh is used to track the position of the fluid-fluid interface. Therefore, we are modeling the interaction of two fluids: the fluid outside the cell represents blood, and the fluid inside the cell represents the internal mechanics of the cell, which also has a specified density and dynamic viscosity. The density of the

cell is characterized by the McCarty lab as the DIC images are produced by calculating the density as a function of the mass and volume of the cells that are being imaged. The dynamic viscosity is set as $\mu_{cell} = 1.36 \text{ Pa} \cdot \text{s}$, which is three orders of magnitude greater than that of blood. This is to simulate the cancer cells as having a much greater viscosity than blood, in order to exhibit behavior related to a thicker fluid, as deformable cells do have an internal viscosity.

The deformability of the cell is enabled by the surface tension criteria, which creates an interface between the two fluids. The surface tension is inversely proportional to the deformability of the cell, meaning that a lower surface tension results in a more deformable cell interface. The surface tension values in our models range from 7×10^{-2} to 5×10^{-7} N/m. Also the fluid flow profile is determined by a pressure gradient between the inlet and the outlet, with pressure differences in our model ranging from 0.1 to 1.5 Pa.

7.2.2 Transport of diluted species

The concentration fields of thrombin associated with each CTC is given by the advection-diffusion equation

$$\frac{\partial C^{(i)}}{\partial t} + \vec{u} \cdot \nabla C^{(i)} = D_i \Delta C^{(i)} \quad (7.6)$$

$$\left. \frac{\partial C}{\partial n} \right|_{\text{wall,cell}} = 0, \quad (7.7)$$

Coagulation Factor	D (10^{-7} cm ² s ⁻¹)
VII	5.1
IX	4.4
VIII	2
X	5
V	1.9
II	4.4

Table 7.3: Coagulation factors with their respective diffusion coefficients, D .

where C is the concentration field, and D_i is the diffusion constant associated with coagulation factors. In our simulations, we currently model one coagulation factor, but in theory, we can include more than one factor in the coagulation cascade. We use the diffusion coefficients for coagulation factors in the blood, tabulated in Table 7.3. All of our simulations use diffusion coefficients in the range from approximately $D = 2 - 5 \times 10^{-7}$ cm²/s. The boundary conditions of the concentration field at the vessel walls and at the cell walls are the no penetration conditions (Neumann boundary conditions). Equation 7.6 is slightly different from the advection-diffusion equation given in Equation 5.1 because of the omission of the delta term. This is because the CTCs are no longer represented as point particles, since they now have a distinct shape and a deformable cell boundary, as seen in Figure 7.1(c).

To model the concentration fields of thrombin, we use the transport of diluted species physics, which models the transport of diluted species by solving for the species concentration. The transport mechanisms include diffusion and convection in the fluid representing the blood only, not inside the cell, since the thrombin fields diffuse out from the surface of the cancer cell into the surrounding blood environment. As stated earlier, the diffusion coefficients used in our model are in the range specified by Table 7.3.

7.2.3 Particle tracking for fluid flow

We incorporate a particle tracking mechanism, where thousands of particles follow increasing gradients of thrombin concentrations. Instead of the nearest neighbor polling technique used in Chapters 5 and 6, we let the particles follow the dynamics of the concentration field according to Equation 7.8

$$\frac{\partial \vec{q}}{\partial t} = \frac{1}{c_0(C + \epsilon)} \left(\frac{\nabla C}{\|\nabla C + \epsilon\|} \right) \quad (7.8)$$

where q is the location of the particle, c_o is a velocity scaling coefficient, and ϵ is a small number that prevents issues arising from singularities when C is equal to zero. The particles are massless and only in the blood flow, not inside the cell. When they make contact with either the boundary of the cell or the blood vessel boundaries, they are set to disappear.

7.2.4 The implicit time-dependent solver algorithm

The finite element discretization of our time-dependent PDE problem is solved by the generalized- α time stepping method, which is one of the nonlinear solver options provided within COMSOL. The generalized- α method is an implicit, second-order accurate method with a parameter α to control the damping of solutions with sharp gradients. We set the error tolerance used for each time step to be 1×10^{-5} .

The other nonlinear solver option is the BDF (backwards differentiation formula) solver, which is also implicit but uses a variable-order, variable step-size implementation. The BDF solver is known for its stability, but it can have severe damping effects, which results in a loss of accuracy due to the smoothing of solutions with sharp gradients. Therefore, we chose to use the generalized- α solver, which causes much less damping and is more accurate. For the same reason, it is also less stable, but for our models, this solver has sufficient stability properties.

COMSOL also builds adaptive finite element meshes, with continual remeshing respecting error tolerance inputs. The automatic remeshing, together with the moving mesh in our two-phase fluid flow, assures a satisfactory mesh quality throughout the simulation. After each remeshing, the time integration is restarted using the generalized- α nonlinear solver, again with an error tolerance of 1×10^{-5} .

7.3 Modeling building process

In this section, we describe the step-by-step modeling building/development we used in COMSOL. In order to ascertain that the models were accurately solving for the results we desired, we started with the simplest settings and added complexities one step at a time.

1. Begin with channel blood vessel with no cells, only blood flow

Figure 7.2 gives the blood velocity field for a simple channel geometry, with a parabolic profile set up by a pressure gradient between the inlet and outlet. The boundary conditions at the top and bottom walls are the viscous boundary conditions.

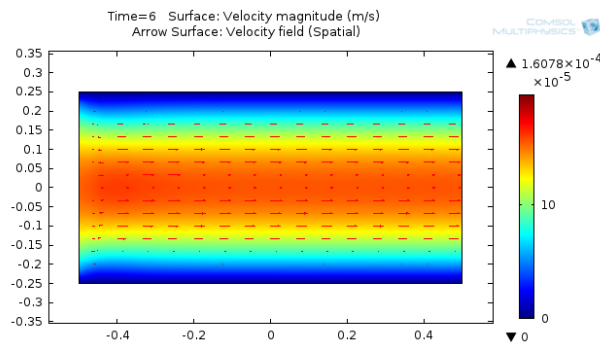


Figure 7.2: Model building: Step 1
The velocity field for simple channel flow.

2. Add a circularly-shaped cancer cell in the flow

Figure 7.3 gives the blood velocity field in the same channel with one deformable cell placed vertically in the middle of the channel. The flow field has been changed in the presence of the cancer cell.

3. Add a chemical thrombin field diffusing outwards from the surface of the cell

Figure 7.4 gives the concentration field of thrombin diffusing from the cells boundary and

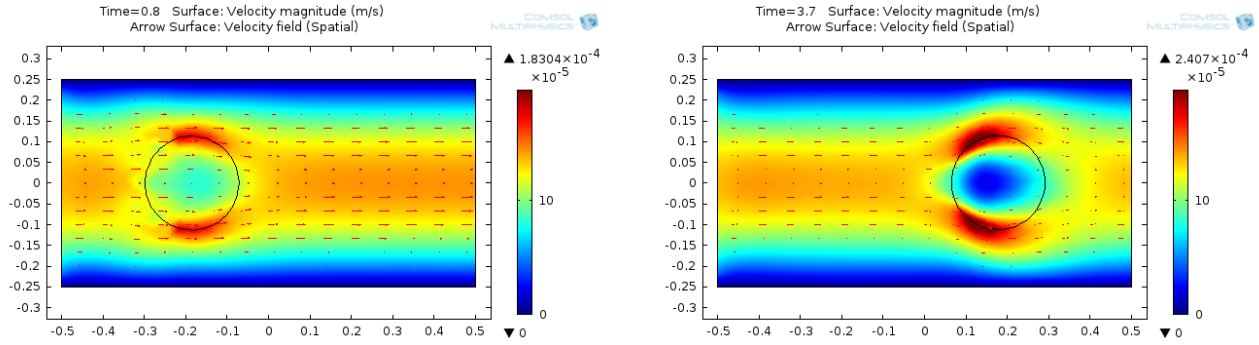


Figure 7.3: Model building: Step 2

The velocity field with one deformable circular cell. The two frames shown are at $T = 0.8$ and 3.7 s.

also advecting with the blood flow. The thrombin field leaves the channel at the outflow boundary, and we enforce the no penetration condition at the two vessel walls.

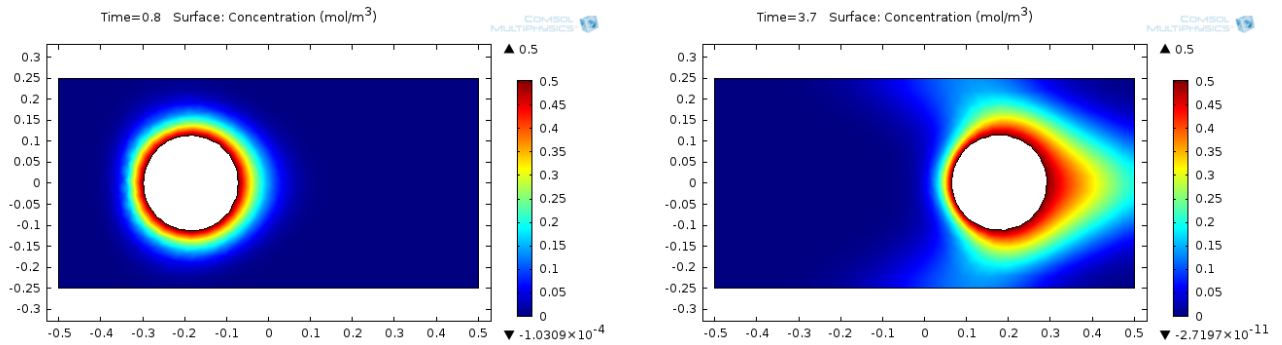


Figure 7.4: Model building: Step 3

The concentration field of thrombin for one deformable circular cell. The two frames shown are at $T = 0.8$ and 3.7 s.

4. Create a branching blood vessel geometry by adding two branches to the channel

Figure 7.5 shows the same simulations as above for a branching geometry. The cancer cell is placed higher in the vertical direction to allow it to travel down the upper branch.

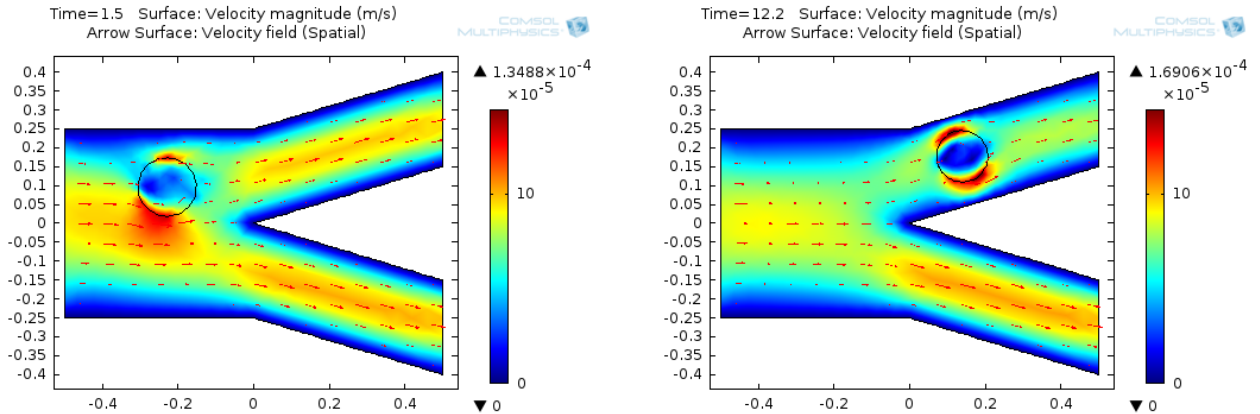


Figure 7.5: Model building: Step 4

The concentration field of thrombin for one deformable circular cell in a branching vessel. The two frames shown are at $T = 1.5$ and 12.2 s.

5. Add particle trackers that follow the velocity flow field

Figure 7.6 shows the passive trackers following the blood velocity field.

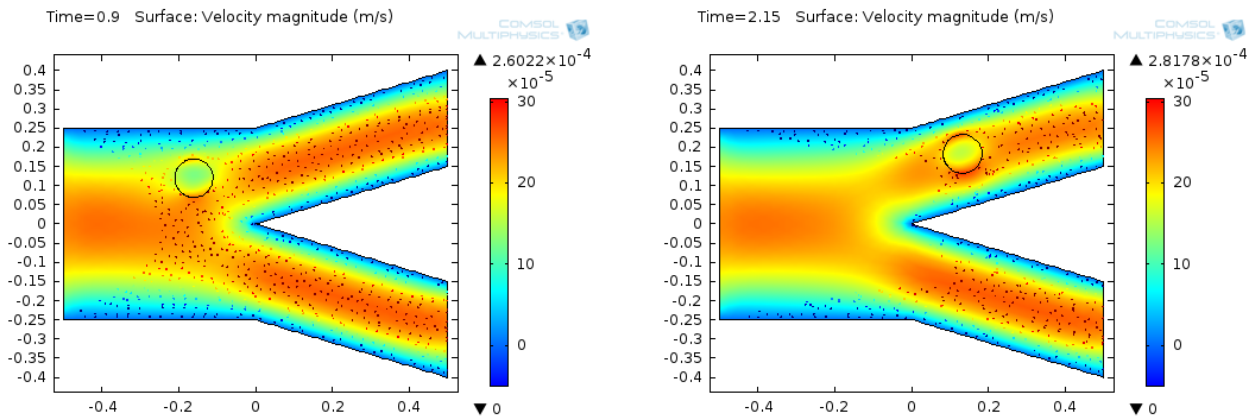


Figure 7.6: Model building: Step 5

Particle trackers following the blood velocity field for one deformable circular cell in a branching vessel. The two frames shown are at $T = 0.9$ and 2.15 s.

6. Add another cell and particle trackers that follow the chemical thrombin field

Figure 7.7 shows the gradient trackers following the thrombin field interaction between two

CTCs. The particles gather on ridges of high concentration between the two cells before the cells split off and travel into their respective branching vessels.

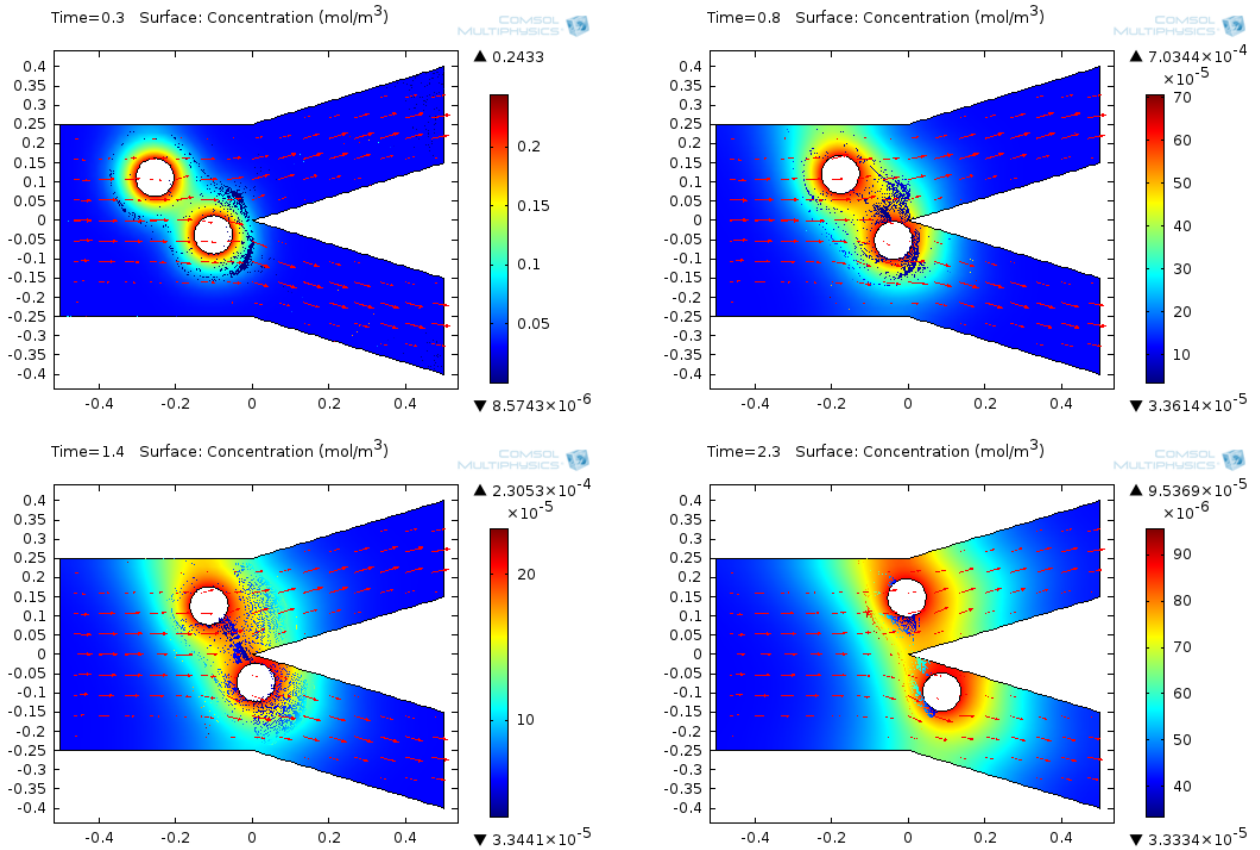


Figure 7.7: Model building: Step 6

Particle trackers following high concentration levels for thrombin field for two deformable circular cell in a branching vessel. The four frames shown are at $T = 0.3, 0.8, 1.4,$ and 2.3 s.

At each step in the model building process, we were confident that the simulation results were physically accurate before moving onto the next step in the development of the final model. We then added more cells, including clusters of cells, scaled the dimensions to match the physiologically relevant parameter space, and included blood and measured cell

properties for the density and dynamic viscosity values to obtain the final models that we describe in the next section.

7.4 Simulation results

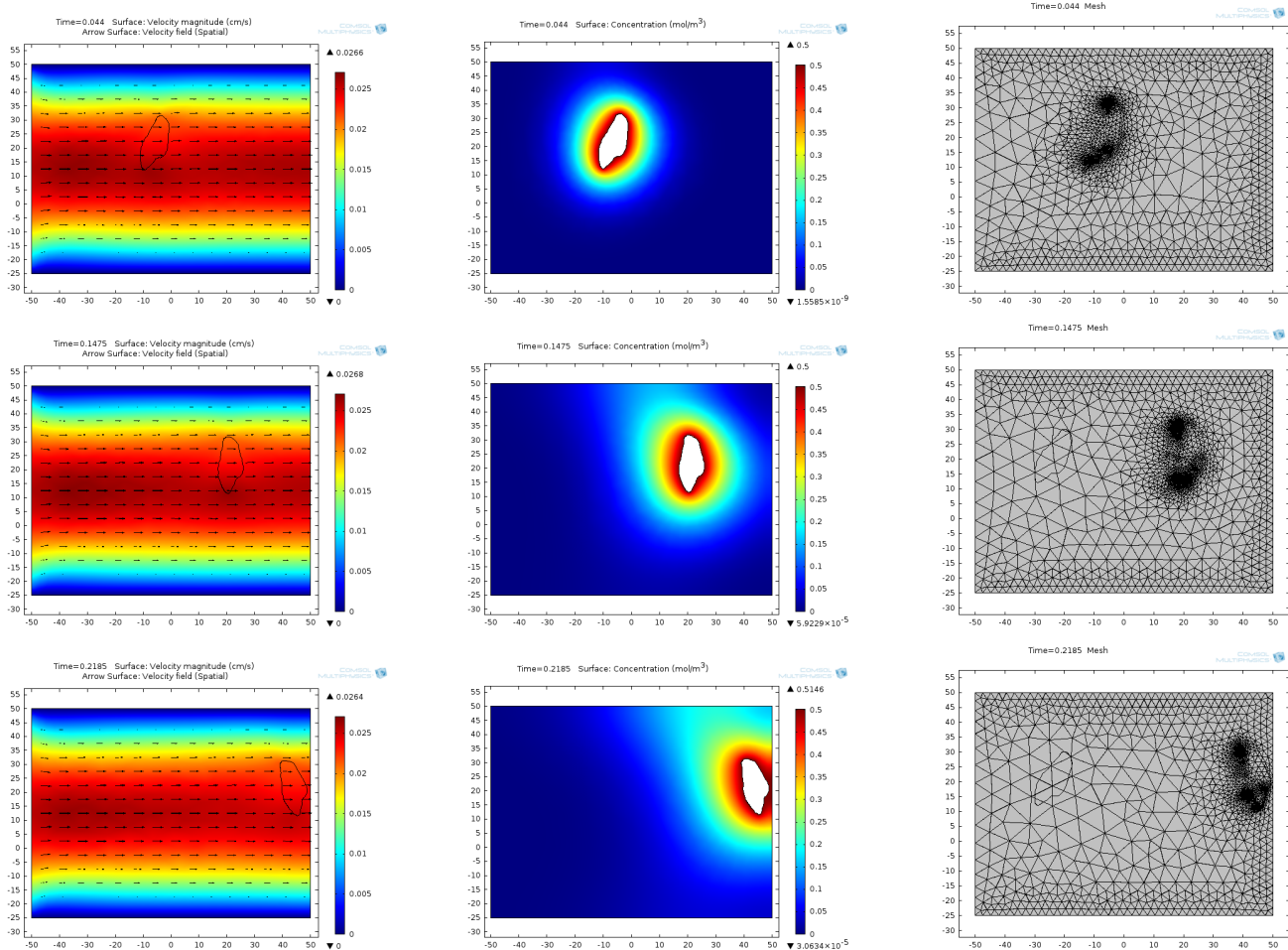
We describe below the models and simulation results for cancer cells of three different types: breast, colon, and lung. Various shapes of cells (both single cells and clusters of cells) and various blood vessel shapes are modeled.

7.4.1 Breast cancer single cell in a channel venule

The first model is based on a breast cancer cell, and the model was shown earlier in Figure 7.1, when we described how the computational model was built based on patient fluid biopsy samples. A single breast cancer cell is placed in a channel venule that is $100\ \mu\text{m}$ in length and $75\ \mu\text{m}$ in height. The size of the breast cell is approximately $10\ \mu\text{m}$ in length and $20\ \mu\text{m}$ in height. It is initially placed closer to the upper boundary layer region as opposed to in the middle of the channel. This initial location causes the cell to rotate in a counter-clockwise motion, due to the effects from the boundary layer region because the flow is slower closer to the venule wall and fastest in the middle of the venule.

Figure 7.8 shows the simulation results for the blood velocity field, the thrombin concentration field, and the adaptive mesh generation. According to Figure 7.8(a), the maximum velocity is $0.026\ \text{cm/s}$, created by a pressure difference of $0.1\ \text{Pa}$ between the inlet and the outlet. Figure 7.8(b) shows the concentration field diffusing outwards and advecting with

the blood flow. The diffusion coefficient in this simulation is $D = 1 \times 10^{-7} \text{ cm}^2/\text{s}$. The thrombin field persists at the upper vessel wall, and is highest near the boundary of the cell. Figure 7.8(c) shows how the adaptive mesh deforms and regenerates at the three time points. The initial complete mesh consists of 2552 domain elements and 183 boundary elements for this simulation. One can see that the mesh is very fine near the cell boundary, in order to accurately solve for the flow physics near the cell's relatively complicated shape, and the mesh is coarser in the channel away from the cell where the physics is simpler to solve.



(a) Blood velocity field (b) Thrombin concentration field (c) Adaptive mesh generation

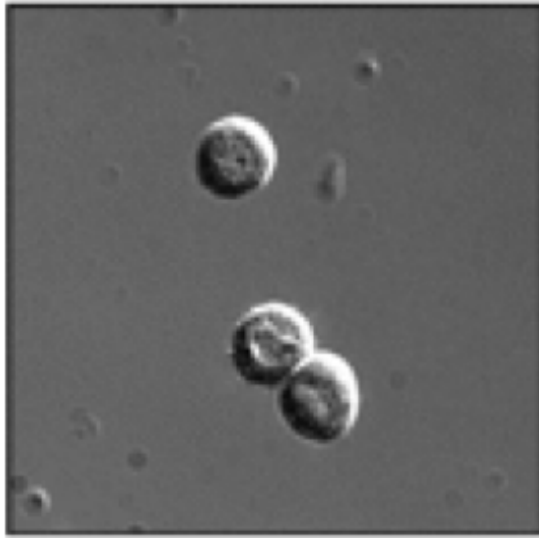
Figure 7.8: Simulation results for the breast cancer model

We show (a) the velocity field of the blood, (b) the concentration field of thrombin, and (c) the adaptive mesh generation, at three different time points in the simulation. The first row is at time $T = 0.044$ s, the second row is at time $T = 0.1475$ s, and the third row is at time $T = 0.2185$ s.

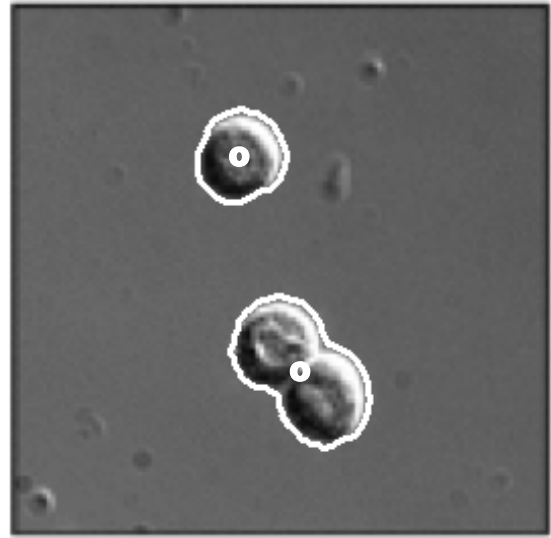
7.4.2 Colon cancer single cell and cluster of two cells in a branching venule

The second model is based on colon adenocarcinoma cancer cells, and the model development is shown in Figure 7.9. These cells are relatively circular in shape, as opposed to the non-circular shape of the breast cancer cell. A single colon cancer cell and a cluster of two cells are placed in a branching venule that is $100\ \mu\text{m}$ in length and $50\ \mu\text{m}$ in height before it branches off into two branches that are each $25\ \mu\text{m}$ in height, with an angle of 30° between them. The single cell and the cluster are placed such that the single cell will travel into the upper branch, and the cluster will travel into the lower branch. Vertically, the cells are placed so that the cluster is very close to the lower boundary layer region. This results in the cluster rotating in a clockwise motion, due to the boundary layer effects.

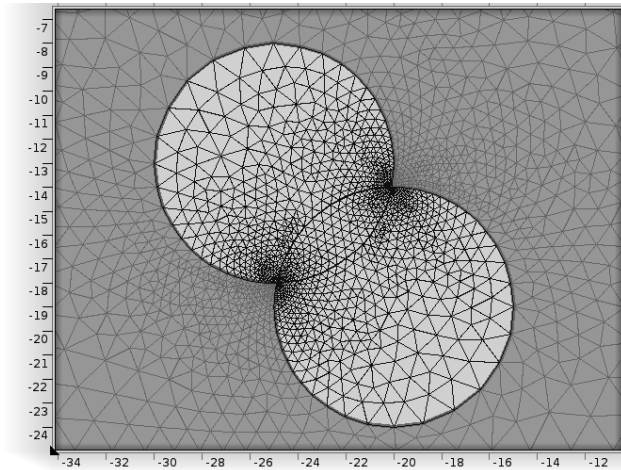
Figure 7.10 shows the simulation results for the blood velocity field, the thrombin concentration field, and the adaptive mesh generation. According to Figure 7.10(a), the maximum velocity is $0.08\ \text{cm/s}$, created by a pressure difference of $1.5\ \text{Pa}$ between the inlet and the outlet. Figure 7.10(b) shows the concentration field diffusing outwards and advecting with the blood flow into the two branching venules. The diffusion coefficient in this simulation is $D = 3 \times 10^{-7}\ \text{cm}^2/\text{s}$. The thrombin field collects in the region between the single cell and the cluster before they travel down their respective branches, and then the thrombin fields persist at the vessel walls. Note that the upper branch shows that the thrombin persists at a higher concentration level near the upper boundary of that branch. Figure 7.10(c) shows how the adaptive mesh deforms and regenerates at the three time points. The initial complete



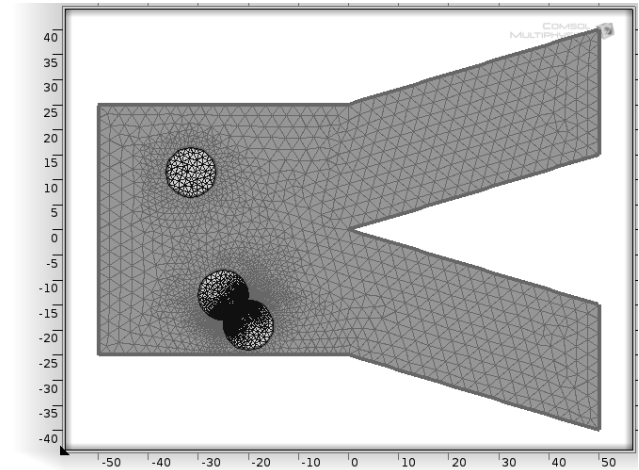
(a) DIC image of cancer cells



(b) Outline of cells from Cell Profiler



(c) Shape of cluster generated in mesh



(d) Cells placed in a branching venule

Figure 7.9: Colon cancer model development from image to mesh

The fluid biopsy is sampled from a colon cancer patient and then (a) imaged using DIC microscopy. CellProfiler (b) outlines the shape of the cells, which is (c) generated as a mesh using COMSOL. Lastly, (d) the single cell and cluster is placed in the computational domain, which in this simulation, is a branching venule.

mesh consists of 5696 domain elements and 334 boundary elements for this simulation. One

can see that the mesh for this model is finer than for the breast cancer model, and again, the mesh is discretized extremely finely near the cell boundary, especially in the cluster.

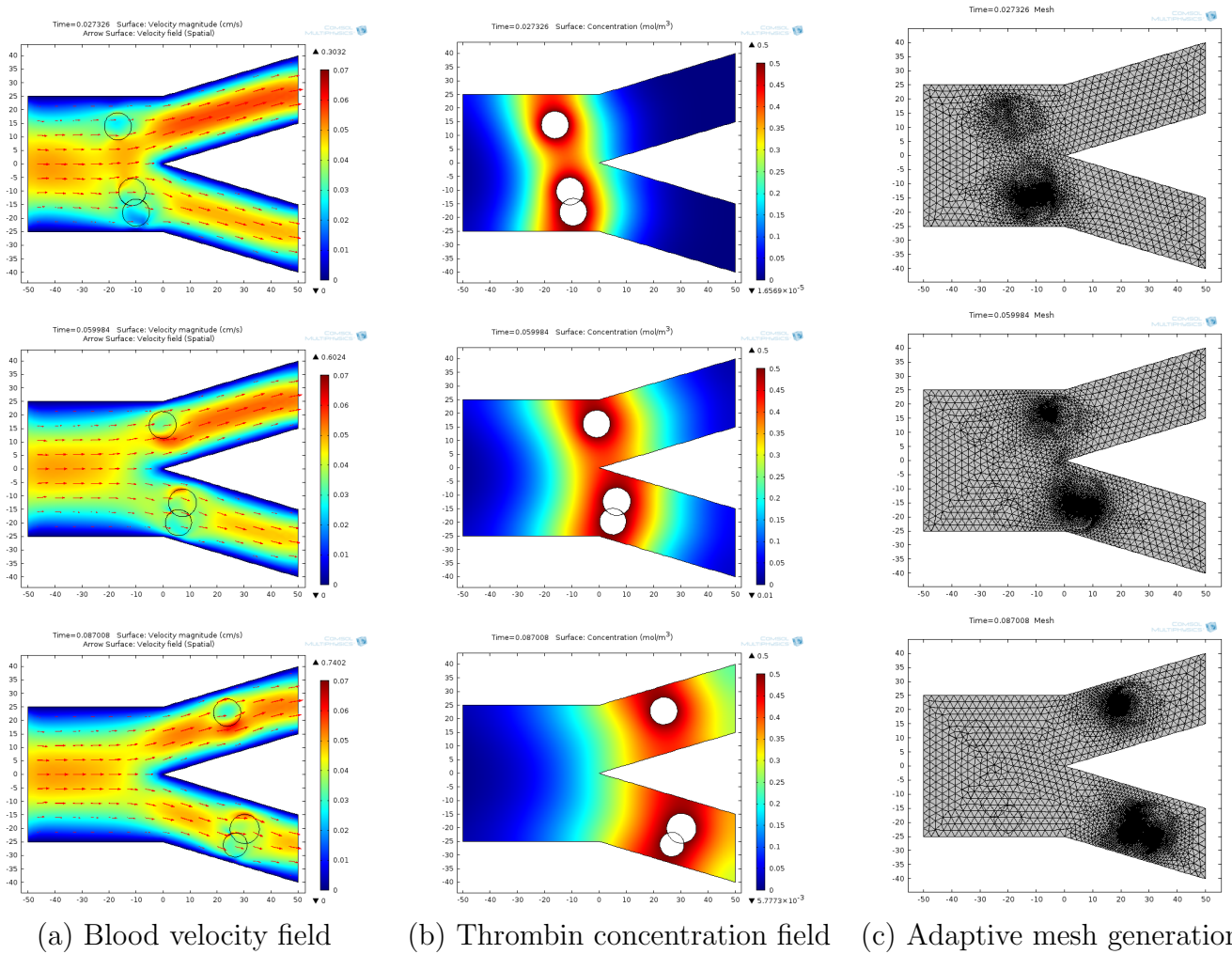


Figure 7.10: Simulation results for the colon cancer model

We show (a) the velocity field of the blood, (b) the concentration field of thrombin, and (c) the adaptive mesh generation, at three different time points in the simulation. The first row is at time $T = 0.027$ s, the second row is at time $T = 0.060$ s, and the third row is at time $T = 0.087$ s.

Particle trackers, or passive particles in the flow, are placed in the simulation to track the increasing gradient in the thrombin concentration field, shown in Figure 7.11. The

particles are released three times at $T = 0, 0.01,$ and 0.02 s, with 5,000 particles released each time. One can see in Figure 7.11(a) that there is a front of particles traveling towards the cells (in the region where the concentration field is colored yellow), and there is also a line created by the particles between the single cell and the cluster (in the region where the concentration field is orange). This line of particles represents the highest concentration zone at this time point, and effectively demonstrates where a fibrinogen bridge may occur in these circumstances. Figure 7.11(b) shows the line and the front moving behind the cells as the cells flow past the particle trackers, and Figure 7.11(c) shows that the front has now become another line of particles in between the single cell and the cluster, right as they flow into their respective branching venules.

Lastly, we performed one more simulation with the colon cancer model that shows the wake structure of the thrombin concentration field, as shown in Figure 7.12. In this simulation, we changed two parameters: the pressure gradient and the diffusion coefficient, while all the other parameters are held the same. The pressure gradient was changed from 1.5 to 0.15 Pa, which is one order of magnitude smaller, and the diffusion coefficient changed from $D = 3 \times 10^{-7}$ cm²/s to $D = 5 \times 10^{-9}$ cm²/s, which is two orders of magnitude smaller than in all of our other models. These two parameter changes result in two distinct differences from the previous simulation. The first is that the cluster travels much faster than the single cell, as it flows farther in the lower branch than the single cell has traveled in the upper branch. This is because at this flow rate, the single cell seems to travel closer to the upper boundary layer region before it reaches the branching point, which results in smaller velocity

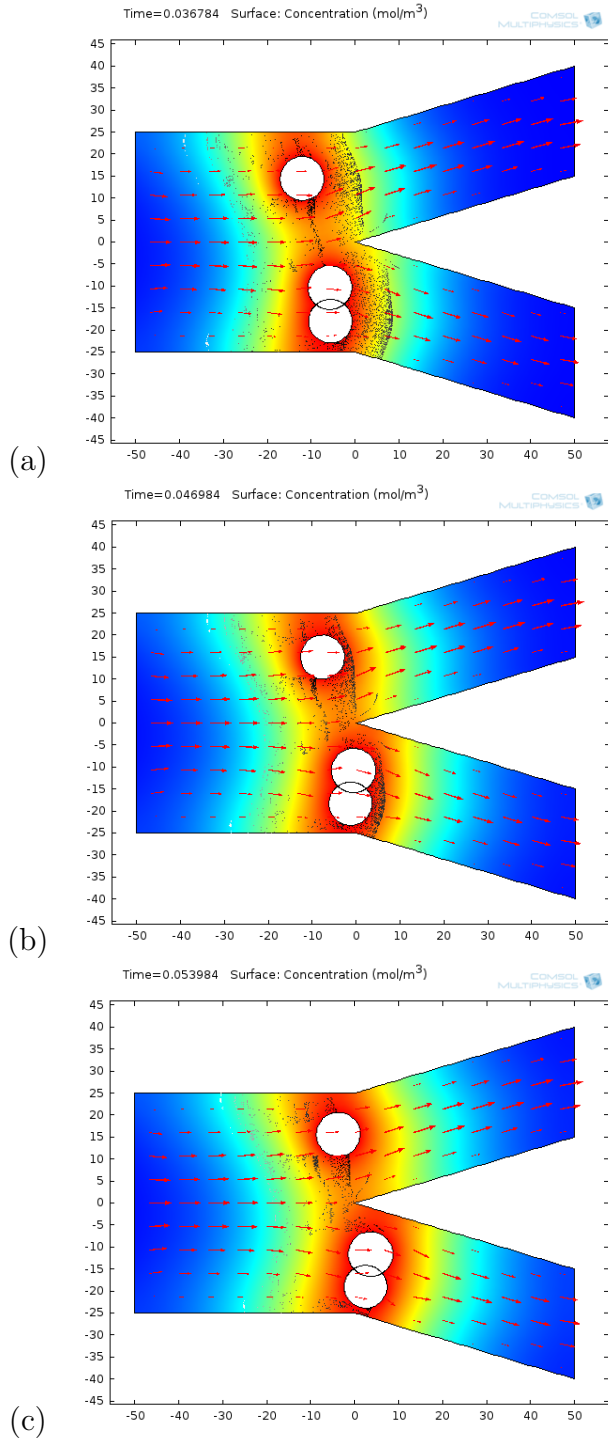


Figure 7.11: Particle tracking simulation for the colon cancer model
 The three time points shown in the figure are at time $T = 0.037$, 0.047 , and 0.054 s.

closer to the vessel wall. The cluster, although initially placed close to the lower boundary layer region, is positioned in the center of the branching venule as it enters the lower branch. The second difference between this simulation and the previous one is that the concentration field clearly shows an interesting wake structure. Although this diffusion coefficient is not physically relevant, it is still useful in determining how the circularly shaped cells rotate as they flow in the blood vessel. The single cell seems to rotate in a counter-clockwise motion, and combined with the tendency of the thrombin to persist at the walls, results in a wake structure of the chemical thrombin field, as shown in Figure 7.12(b) and (c). For the cluster, it seems to rotate in a clockwise motion, resulting in a wake structure in which the concentration field is trailing the cluster at the upper boundary layer and leading the cluster in the lower boundary layer in the branch, as shown in Figure 7.12(b) and (c).

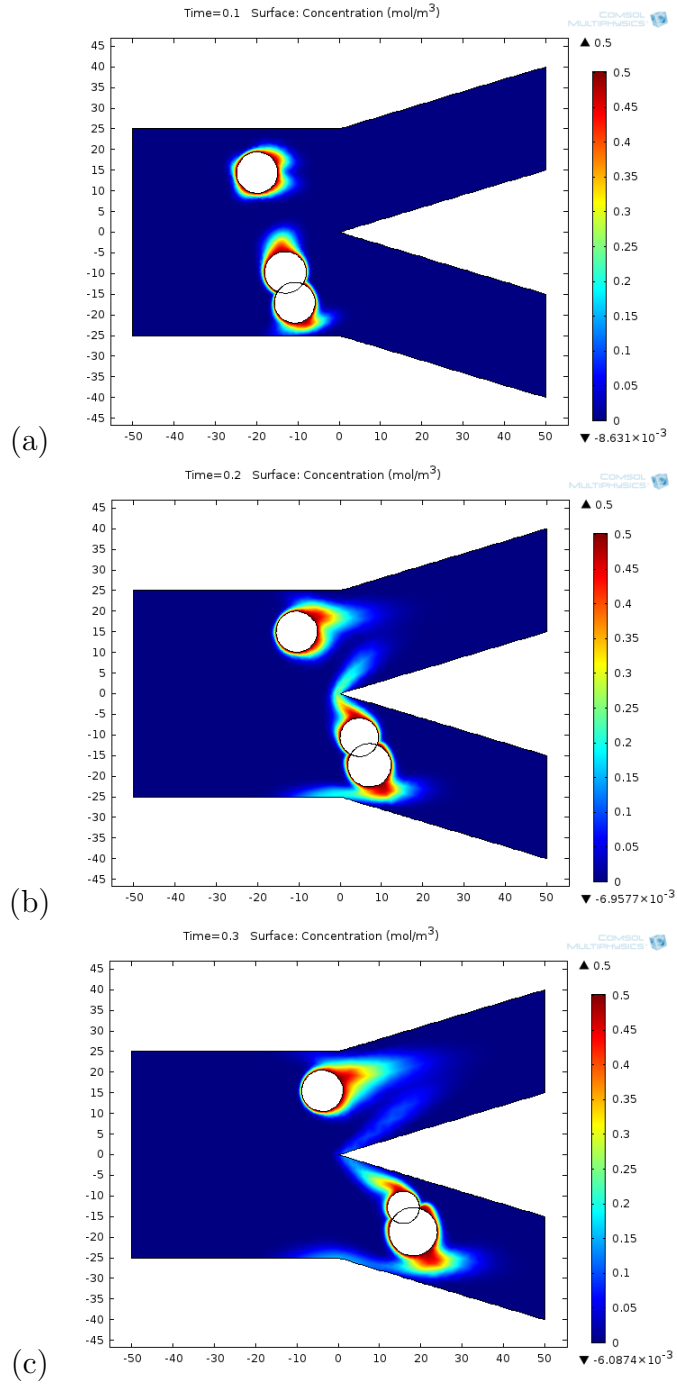


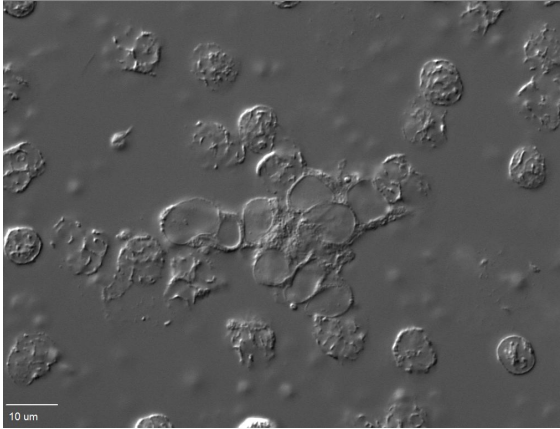
Figure 7.12: Wake structure formation of the chemical thrombin field in the colon cancer model

The three time points shown in the figure are at time $T = 0.100, 0.200,$ and 0.300 s.

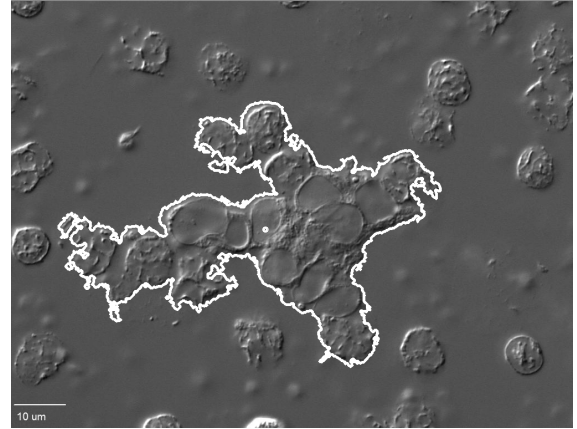
7.4.3 Lung cancer cluster in a branching venule

The third model is based on lung cancer cells, and the model development is shown in Figure 7.13. Here we have a cluster of many cells, specifically 17 cells. Some of these cells may be white blood cells that were captured in the cluster outline in Cell Profiler. Nevertheless, the cluster is a highly non-uniform shape that is approximately $65 \mu\text{m}$ in length and $45 \mu\text{m}$ in height. The blood vessel is another branching venule, as in the colon cancer model. However, since the cluster is relatively larger than in the previous model, the size dimensions of the venule are also larger, with the length being $125 \mu\text{m}$ and the height being $80 \mu\text{m}$. The two branches are now each $40 \mu\text{m}$ in height, with an angle of 30° between them. One can see that the angle between the branches, which previously formed a sharp point, has been smoothed to have a radius of $1.5 \mu\text{m}$. This smoothing was done in order to prevent the simulation from breaking down when the cluster reaches the branching point. The initial position of the center of mass of the lung cluster is placed vertically in the middle of the venule. The center of mass is determined in Cell Profiler and shown in Figure 7.13(b).

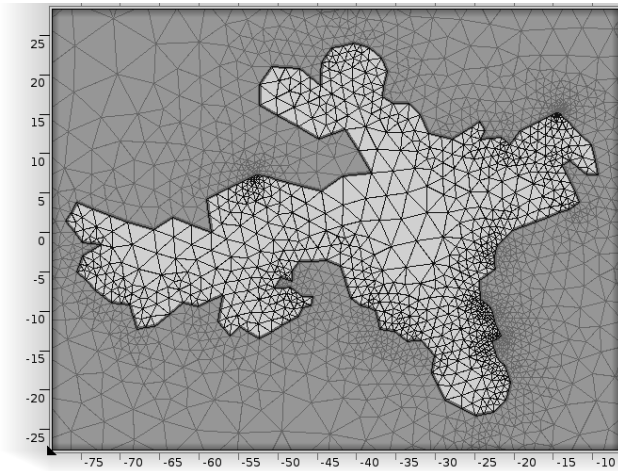
Figure 7.14 shows the simulation results for the blood velocity field, the thrombin concentration field, and the adaptive mesh generation. According to Figure 7.14(a), the maximum velocity is 0.088 cm/s , created by a pressure difference of 0.1 Pa between the inlet and the outlet. Upon reaching the branching point, the cluster significantly obstructs the blood flow in the computational domain. The flow into the upper branch is much slower than in the lower branch. The cluster also begins to deform, with the upper part of the cluster deforming slightly in a clockwise motion and the lower part of the cluster deforming slightly in a



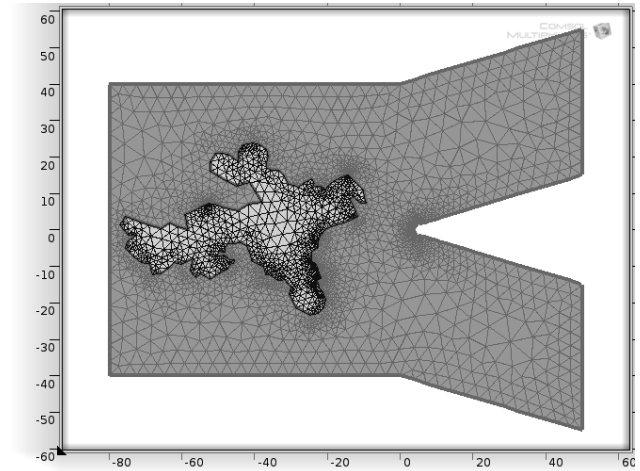
(a) DIC image of cancer cells



(b) Outline of cluster from Cell Profiler



(c) Shape of cluster generated in mesh



(d) Cluster placed in a branching venule

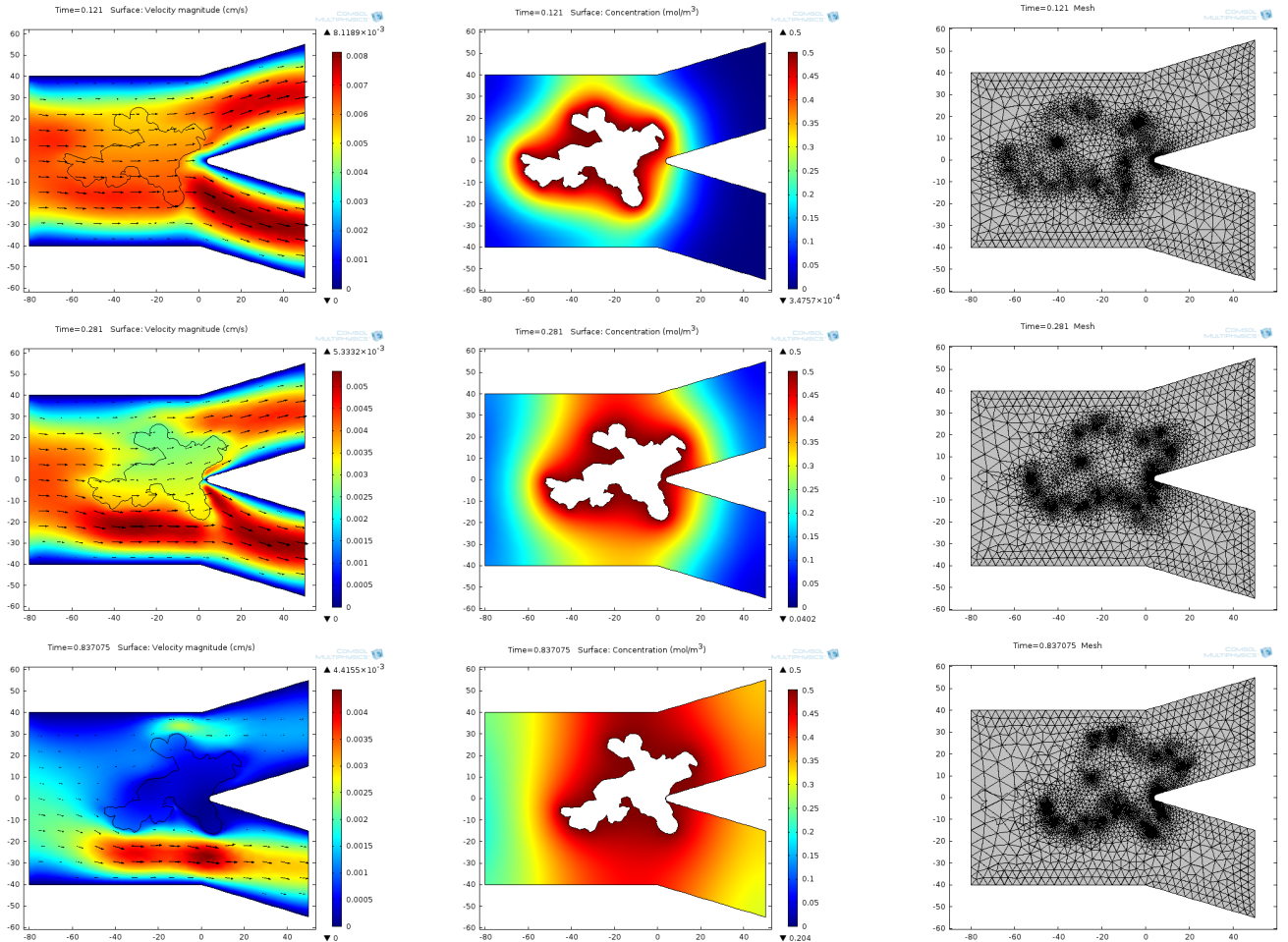
Figure 7.13: Lung cancer model development from image to mesh

The fluid biopsy is sampled from a lung cancer patient and then (a) imaged using DIC microscopy. CellProfiler (b) outlines the shape of the cluster, which is (c) generated as a mesh using COMSOL. Lastly, (d) the cluster is placed in the computational domain, which in this simulation, is a branching venule.

counter-clockwise motion. Figure 7.14(b) shows the concentration field diffusing outwards and advecting with the blood flow into the two branching venules. The diffusion coefficient in this simulation is $D = 1 \times 10^{-7} \text{ cm}^2/\text{s}$. The thrombin field persists at the vessel walls, and one can note that the thrombin concentration field is greater in the upper branch than

in the lower branch because the flow being greater in the lower branch causes more of the thrombin to travel away from the cluster at a higher velocity. Figure 7.14(c) shows how the adaptive mesh deforms and regenerates at the three time points. The initial complete mesh consists of 4872 domain elements and 346 boundary elements for this simulation. One can see that the mesh for this model is finely discretized near the cluster boundary, as well as in the smoothed branching point.

Particle trackers are placed in this simulation as well to track the increasing gradient in the thrombin concentration field, shown in Figure 7.15. The particles are released four times at $T = 0, 0.15, 0.3,$ and 0.45 s, with 5,000 particles released each time. Since there is one cluster in the simulation, there is no fibrinogen bridge formation as shown in the previous colon cancer model, but the front of particles is exhibited again. The particles show that early in the simulation, the thrombin field closely resembles the shape of the cluster as shown in Figure 7.15(a) and (b), whereas later in the simulation, the thrombin field is dictated by the blood vessel geometry as shown in Figure 7.15(c) and (d).



(a) Blood velocity field (b) Thrombin concentration field (c) Adaptive mesh generation

Figure 7.14: Simulation results for the lung cancer model

We show (a) the velocity field of the blood, (b) the concentration field of thrombin, and (c) the adaptive mesh generation, at three different time points in the simulation. The first row is at time $T = 0.121$ s, the second row is at time $T = 0.281$ s, and the third row is at time $T = 0.837$ s.

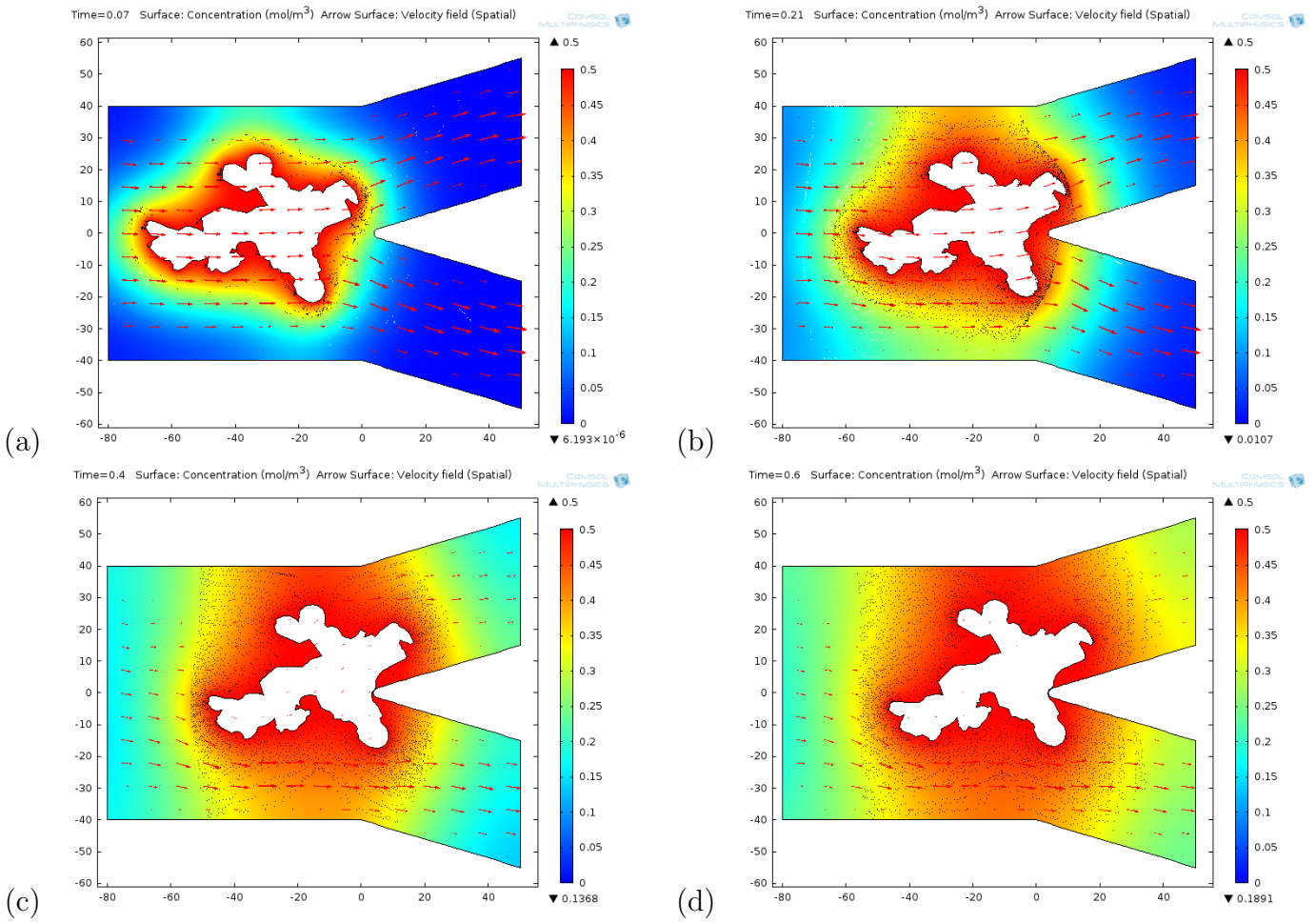


Figure 7.15: Particle tracking simulation for the lung cancer model
 The four time points shown in the figure are at time $T = 0.070, 0.210, 0.400,$ and 0.600 s.

Discussion and future directions

8.1 Future work for deformation of cancer cells in flow (Part I)

The cell deformation model we developed, in which the cell surface is allowed to deform parametrically as a family of Gaussian surfaces, does a reasonably good job of capturing the principal deformations of a cell under realistic flow conditions when the parameters in the empirical constitutive equations are chosen to match the experiment. The Active Shape Model was used to extract deformation parameters from the experiment and tune the corresponding parameters in an empirical constitutive equation for the cell surface response to the flow, and it provided the necessary link between our experiment and a numerical simulation. For this particular experiment, a linear constitutive assumption sufficed due to the relatively mild deformations of the cell, but one could easily imagine extending the technique to situations requiring nonlinear constitutive assumptions in which case higher order terms in (3.5), (3.6) would be retained and more complicated assumptions, which include

cross-flow terms $f_x f_y$, would need to be used. In that case, a series of different experiments with flow coming from different directions would be used to estimate the parameters. Figure 8.1 shows a flow diagram of the steps we used in our model to obtain flow simulations using our trained force-response law. An important future step that closes the loop is indicated by the red dashed arrow, which is to re-run experiments under different flow conditions in order to get better and better information about the constitutive equations.

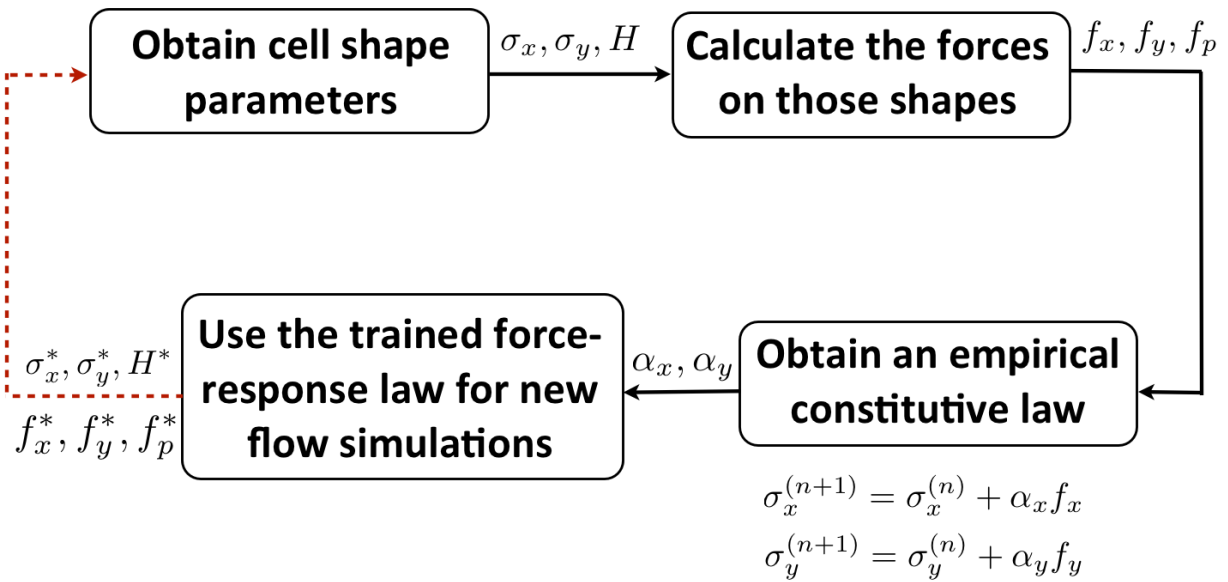


Figure 8.1: Flow diagram of modeling procedure for cell deformation model
 Schematic flow diagram of the steps we used to develop the cell deformation model in Part I. Note that the red dashed arrow, which closes the loop, has not been completed yet, but it is an important future step to strengthen the model’s constitutive equations.

In this thesis, the full capability of the ASM algorithm is yet not being realized in the sense that once a model is trained by a series of experiments, the algorithm can then be used to simulate the ways in which the trained model acts under a much wider set of conditions than those from which it was originally trained. In principle, for example, one

can use it to generate computer animations of a deformable cell which deforms in ways that are consistent with the training sets, but do not necessarily identically match any of the individual experimental runs. As a potentially useful way the algorithm could be used to understand cancer cell deformation, one could imagine setting up two separate flow experiments for training models, one using a normal white blood cell, the other using a circulating tumor cell. The ASM algorithm could be used in this setting to (i) uncover the differences in the modes of deformation of these two kinds of cells, and (ii) run these two differently trained cell models through new environments, such as simulated capillary beds, to quantify differences in their respective responses. We believe ASM and related algorithms, such as the Active Appearance Models [18] and Active Contour Models [43], are ripe for further exploitation in these cellular level biological settings.

8.2 Future work for procoagulant circulating tumor cells in flow (Part II)

In this thesis, we develop novel computational tools to model and characterize the movement of diffusing thrombin fields emitted from CTCs in flow, with the aim of scaling up the techniques to more complex arterial environments and more complex, time-dependent flow assumptions [66]. A main finding from our model is the build-up and persistence of thrombin concentrations near vessel walls and in complex time-dependent overlap regions of the flow. The build-up near walls occurs on a relatively long timescale compared to the timescale in

which the concentration fields diffuse (regulated by the diffusion constants α_i). We expect this main finding to persist under more complex and realistic flow geometries, as locally, near a vessel wall, the boundary curvature should not play a big role. Furthermore, very near the vessel wall where viscous flow boundary conditions dominate, blood velocity magnitudes are small, so should have minimal effects on disturbing the concentration fields that build-up there, therefore we do not expect the inviscid fluid boundary conditions used in this study to qualitatively alter this main finding.

In complex capillary beds where branching of the flow into several different regions is the reality, we do expect the tracking of the diffusive overlap regions of many CTCs to be more computationally challenging, yet the main finding that concentration levels are relatively high in overlap regions should remain valid. Thrombin has several well characterized effects on endothelial cells and platelets which are also located at blood vessel walls under flow. In addition, the proximity of CTCs to each other determined the persistence of thrombin concentrations in the flow, which may help explain the effect of cell count on coagulation kinetics [74], suggesting that CTC counts may hold significance to understanding the role for CTCs in activating blood coagulation. The gradient tracking capability described here holds strong potential to aid in the understanding of the fate of CTC-generated thrombin in more complex settings that arise within the circulation.

We build models for diffusing CTCs in flow with vessel wall boundaries, and exact analytical formulations allow us to clearly see the concentration buildup near walls, diffusing particles, and complex overlap flow regions. We also develop finite element computational

models that are used under a wider range of boundary conditions and flow conditions. In order to best simulate the flow of circulating tumor cells and their developing chemical concentration gradients, we model the blood flow as a parabolic Poiseuille flow profile and use initial configurations of actual patient fluid biopsy samples in channel and branching vessel geometries.

The future work we propose would more closely model the physiological conditions in the human body, by further developing our COMSOL models to include more realistic blood vessel geometries of the venous system, where blood clots are most susceptible to occur. As our COMSOL models are currently in 2D, further developing 3D computational models (and COMSOL does have the capability to build 3D models) and performing high resolution simulations would also enable us to better understand and interpret the flow physics and concentration gradient field evolution in our models. In order to more accurately develop these complex models in 3D, we propose to further develop the DIC imaging tools used in the McCarty group at OHSU to obtain 3D spatial information about circulating tumor cells identified in patient fluid biopsy samples. Perhaps individualized data about each patient's vasculature and circulatory system can be obtained using non-invasive imaging techniques, as in [4] using MR and CT angiography. If we can even characterize specific areas in the venous system where blood clotting may be more at risk for thrombosis, specific cancer clotting models can be developed, enabling physicians to practice improved therapeutic care using a quantitative risk analysis tool that is tailored to individual patients.

With these tools in place, we can begin to develop diffusing particle simulations to include more complex and realistic geometries and flow conditions. We can also include chemical enzyme reactions to model the coagulation cascade, as in the previous models presented by Fogelson and Gregg [51, 12]. The overall goal is to develop a spatial-temporal mathematical model of blood clotting from circulating tumor cells in flow, which couples the physical process of chemical concentration gradients under blood flow with the biochemical enzyme reactions that regulate the hemostatic system in the body. Capturing the delicate and complex interplay between these physical and chemical processes is the key to understanding blood coagulation in metastatic cancer.

We have developed models and simulations in COMSOL Multiphysics, giving us the tools to create computational and mathematical models for new and other potentially useful applications. One such new application is the experimental setup created by Parag Mallick and his group at Stanford University [14], with whom we have had extensive conversations on their experiments investigating the deformability and surface friction of cancer cells. They characterize cancer cells passing through a constriction at the end of a suspended microfluidic channel (Figure 8.2), and we are interested in modeling how the cell deforms as a result of the surface friction and internal mechanics of the cell as it flows through the constriction. This is one example of many potential collaborations that may result from our development of computational tools using COMSOL Multiphysics. We believe that the research areas of mathematical and computational modeling and simulation of various biophysical phenomena

surrounding metastatic cancer cells are currently ripe with opportunities for growth and progress.

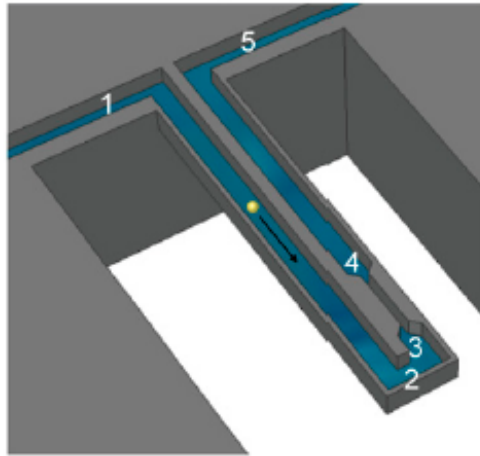


Figure 8.2: Experimental setup of cancer cell passing through microfluidic channel
Schematic diagram of the suspended microchannel resonator (SMR) with a constriction located between Points 3 and 4. Numbers 1-5 indicate the different positions in the microchannel that signify the flow trajectory of a cell.

Bibliography

- [1] Ainley, J., et al., *The method of images for regularized stokeslets*. J. Comp. Phys, 2008. **227**: p. 4600-4616.
- [2] Amirkhosravi, A., et al., *Tissue factor pathway inhibitor reduces experimental lung metastasis of B16 melanoma*. Thromb. Haemost., 2002. **8**: p. 930-936.
- [3] Anand, M., et al., *A model incorporating some of the mechanical and biochemical factors underlying clot formation and dissolution in flowing blood*. J. Theoret. Med., 2003. **5**: p. 183-218.
- [4] Antiga, L., et al., *Computational geometry for patient-specific reconstruction and meshing of blood vessels from MR and CT angiography*. IEEE T. Med. Imaging, 2003. **22**(5): p. 674-684.
- [5] Ataullakhanov, F. I., et al., *Spatiotemporal dynamics of clotting and pattern formation in human blood*. Biochim. Biophys. Acta, 1998. **1425**: p. 453-468.
- [6] Ataullakhanov, F. I., et al., *Spatio-temporal dynamics of blood coagulation and pattern formation. A theoretical approach*. Int. J. Bifurcat. Chaos, 2002. **12**(9): p. 1985-2002.
- [7] Bakker, D.P., et al., *Comparison of velocity fields for different flow chamber designs used in studies of microbial adhesion to surfaces*. Applied Environ. Microbio., 2003. **69**(10): p. 6280-6287.
- [8] Berny-Lang, M.A., et al., *Promotion of experimental thrombus formation by the procoagulant activity of breast cancer cells*. Phys. Biol., 2011. **8**: p. 015014.
- [9] Blom, J. W., et al., *Malignancies, prothrombotic mutations, and the risk of venous thrombosis*. JAMA, 2005. **293**: 715-722.
- [10] Boal, D., **Mechanics of the Cell**. Cambridge: Cambridge University Press, 2002.
- [11] Bodnar, T. and A. Sequeira, *Numerical simulation of the coagulation dynamics of blood*. Comp. and Math. Meth. in Medicine, 2008. **9**: p. 83-104.

- [12] Brummel-Ziedins, K. E., et al., *Modeling thrombin generation: plasma composition based approach*. J. Thromb. Thrombolysis, 2013. **0929**: p. 5305.
- [13] Butler, T.P. and P.M. Gullino, *Quantitative cell shedding into efferent blood of mammary adenocarcinoma*. Cancer Res., 1975. **35**: p. 512-516.
- [14] Byun, S., et al., *Characterizing deformability and surface friction of cancer cells*. PNAS, 2013. **100**(19): p. 7580-7585.
- [15] Chatterjee, M.S., et al., *Systems biology of coagulation initiation: kinetics of thrombin generation in resting and activated human blood*. PLoS Comput. Biol., 2010. **6**: e1000950.
- [16] Che, S., et al., *Role of tissue factor and tissue factor pathway inhibitor complex in cancer cell adhesion*. Third Annual NCI Physical Sciences-Oncology Centers (PS-OCs) Network Investigators Meeting, poster session, 2012.
- [17] Cho, E. H., *Circulating tumor cells as emerging tumor biomarkers in lung cancer*. J. Thorac. Dis., 2012. **4**(5): p. 444-445.
- [18] Cootes, T.F., et al., *Active appearance models*. IEEE TPAMI, 2001. **23**(6): p. 681-685.
- [19] Cootes, T.F., et al., *Active shape models — their training and application*. Comput. Vision Image Understanding, 1995. **61**(1) p. 38-59.
- [20] Cootes, T. F., et al., *The use of active shape models for locating structures in medical images*. Image Vision Comput., 1994. **12**(6): p. 355-366.
- [21] Cortez, R., *The method of regularized stokeslets*. SIAM J. Sci. Comp, 2001. **23**(4): p. 1204-1225.
- [22] Couzin, C., et al., *Critical stresses for cancer cell detachment in microchannels*. Eur. Biophysics J., 2009. **38**: p. 1035-1047.
- [23] Dashkevich, N. M., et al., *Thrombin activity propagates in space during blood coagulation as an excitation wave*. Biophys. J., 2012. **103**: p. 2233-2240.
- [24] Duffy, D.G., **Green's Functions with Applications**. Boca Raton: Chapman & Hall/CRC, 2001.
- [25] Dzwinel, W., et al., *A discrete-particle model of blood dynamics in capillary vessels*. J. Colloid Interface Sci., 2003. **258**: p. 163-173.
- [26] Fogelson, A.L., *Cell-based models of blood clotting*. **Mathematics and Biosciences in Interaction**, Basel: Birkhauser Verlag, 2007. p. 243-269.
- [27] Fogelson, A.L. and N. Tania, *Coagulation under flow: the influence of flow-mediated transport on the initiation and inhibition of coagulation*. Pathophysiol. Haemost. Throm., 2005. **34**: p. 91-108.

- [28] Forman, S.D. and Y. Nemerson, *Membrane-dependent coagulation reaction is independent of the concentration of phospholipid-bound substrate: fluid phase factor X regulates the extrinsic system*. Proc. Natl. Acad. Sci., 1986. **83**: p. 4675-4679.
- [29] Gaver III, D.P. and S.M. Kute, *A theoretical model study of the influence of fluid stress on a cell adhering to a microchannel wall*. Biophys. J., 1998. **75**: p. 721-733.
- [30] Gay, F.J. and B. Felding-Habermann, *Contribution of platelets to tumour metastasis*. Nat. Rev. Cancer, 2011. **11**: p. 123-134.
- [31] Gemmell, C. H., et al., *Flow as a regulator of the activation of factor X by tissue factor*. Blood, 1988. **72**: p. 1404-1406.
- [32] Giesen, P.L.A., et al. *Production of thrombin by the prothrombinase complex is regulated by membrane-mediated transport of prothrombin*. J. Biol. Chem., 1991. **266**: p. 1379-1382.
- [33] Gregg, K.L., *A mathematical model of blood coagulation and platelet deposition under flow*. 2010.
- [34] Gomez, K. and J.H. McVey, *Tissue factor initiated blood coagulation*. Front. Biosci., 2006. **11**: p. 1349-1359.
- [35] Hall, C. L., et al., *Factor Xa generation at the surface of cultured rat vascular smooth muscle cells in an in vitro flow system*. J. Biomech. Eng., 1998. **120**: p. 484-490.
- [36] Hasimoto, H. and O. Sano, *Stokeslets and eddies in creeping flow*. Ann. Rev. Fluid Mech., 1980. **12**: p. 335-363.
- [37] Haynes, L.M., et al., *Dilutional control of prothrombin activation at physiologically relevant shear rates*. Biophys. J., 2011. **100**: p. 765-773.
- [38] Hazel, A.L. and T.J. Pedley, *Vascular endothelial cells minimize the total force on their nuclei*. Biophys. J., 2008. **78**: p. 47-54.
- [39] Hockin M.F., et al., *A model for the stoichiometric regulation of blood coagulation*. J. Biol. Chem., 2002. **277**: p. 18322-18333.
- [40] Hundsdorfer, W. and J.G. Verwer, **Numerical Solution of Time-Dependent Advection-Diffusion Reaction Equations**. Berlin: Springer-Verlag, 2003.
- [41] Hunter, K.K., et al., *Mechanisms of metastasis*. Breast Cancer Res., 2008. **10**(1): S2.
- [42] Jadhav, S., et al., *A 3-D computational model predicts that cell deformation affects selectin-mediated leukocyte rolling*. Biophys. J., 2005. **88**: p. 96-104.
- [43] Kass, M., et al., *Snakes: Active Contour Models*. Int. J. of Computer Vision, 1988. p. 321-333.

- [44] Kevorkian, J., **Partial Differential Equations: Analytical Solution Techniques**. Pacific Grove, CA: Wadsworth & Brooks/Cole Mathematics Series, 1989.
- [45] Khorana, A.A., et al., *Thromboembolism is a leading cause of death in cancer patients receiving outpatient chemotherapy*. J. Thromb. Haemost., 2007. **5(3)**: p. 632-4.
- [46] Kim, S. and S.J. Karrila, **Microhydrodynamics: Principles and Selected Applications**. Mineola: Dover Pubs, 2005.
- [47] Kuhn, P. and K. Bethel, *A fluid biopsy as investigating technology for the fluid phase of solid tumors*. Phys. Biol., 2012. **9**: p. 010301.
- [48] Ledford, H., *Cancer theory faces doubts*. Nature, 2011. **472**: p. 273.
- [49] Lee, J.S.H., et al., *Cdc42 mediates nucleus movement and MTOC polarization in Swiss 3T3 fibroblasts under mechanical shear stress*. Molecular Bio. of the Cell, 2005. **16**: p. 871-880.
- [50] Lee, J.S.H., et al., *Ballistic intracellular nanorheology reveals ROCK-hard cytoplasmic stiffening response to fluid flow*. J. Cell Sci., 2006. **119**: p. 1760-1768.
- [51] Leiderman, K. and A.L. Fogelson *Grow with the flow: a spatial-temporal model of platelet deposition and blood coagulation under flow*. Math. Med. Biol., 2011. **28**: p. 47-84.
- [52] Levchenko, A. and P. A. Iglesias, *Models of eukaryotic gradient sensing: application to chemotaxis of amoebae and neutrophils*. Biophys. J., 2002. **82**: p. 50-63.
- [53] Marchetti, M., et al., *All transretinoic acid modulates the procoagulant activity of human breast cancer cells*. Thomb. Res., 2011. **128**: p. 368-374.
- [54] Marchetti, M., et al., *Characterization of thrombin generation potential of leukemic and solid tumor cells by the calibrated automated thrombography*. Haematologica, 2012. **97**: p. 1173-1180.
- [55] Marrinucci, D., et al., *Fluid biopsy in patients with metastatic prostate, pancreatic, and breast cancers*. Phys. Biol., 2012. **9(1)**: p. 016003.
- [56] McGee, M.P., et al., *Diffusion control in blood coagulation*. J. Biol. Chem., 1992. **267**: p. 24333-24339.
- [57] Molnar, B., et al., *Circulating tumor cell clusters in the peripheral blood of colorectal cancer patients*. Clin. Cancer Res., 2001. **7**: p. 4080-4085.
- [58] Mueller, B. M., et al., *Expression of tissue factor by melanoma cells promotes efficient hematogenous metastasis*. Proc. Natl. Acad. Sci. U.S.A., 1992. **89**: p. 11832-11836.
- [59] Mueller, B. M. and W. Ruf, *Requirement for binding of catalytically active factor VIIa in tissue factor dependent experimental metastasis*. J. Clin. Invest., 1998. **101**: p. 1372-1378.

- [60] Nemerson, Y., *The phospholipid requirement of tissue factor in blood coagulation*. J. Clin. Invest., 1968. **47**: p. 72-80.
- [61] Okorie, U. M., et al., *Determination of surface tissue factor thresholds that trigger coagulation at venous and arterial shear rates: amplification of 100 fM circulating tissue factor requires flow*. Blood, 2008. **111**: p. 3507-3513.
- [62] Otero, L.L., et al., *Tissue factor as a novel marker for detection of circulating cancer cells*. Biomarkers, 2011. **16**: p. 58-64.
- [63] Panteleev, M. A., et al., *Spatial propagation and localization of blood coagulation are regulated by intrinsic and protein C pathways, respectively*. Biophys. J., 2006. **90**: p. 1489-1500.
- [64] Panteleev, M. A., et al., *Task-oriented modular decomposition of biological networks: trigger mechanism in blood coagulation*. Biophys. J., 2010. **99**: p. 1751-1761.
- [65] Pawar, P., et al., *Roles of cell and microvillus deformation and receptor-ligand binding kinetics in cell rolling*. Am. J. Physiol. Heart Circ. Physiol., 2008. **295**: p. H1439-H1450.
- [66] Pedley, T. J., **The Fluid Mechanics of Large Blood Vessels. Cambridge Monographs on Mechanics and Applied Mathematics**. Cambridge: Cambridge University Press, 1980.
- [67] Roberts, M.G., et al., *Automatic segmentation of lumbar vertebrae on digitized radiographs using linked active appearance models*. Proc. Medical Image Understanding and Analysis, 2006. **2**: p. 120-124.
- [68] Roussos, E.T., et al., *Chemotaxis in cancer*. Nat. Rev. Cancer, 2011. **11**: p. 573-587.
- [69] Sahai, E., *Mechanisms of cancer cell invasion*. Curr. Opin. Genetics and Development, 2005. **15**: p. 87-96.
- [70] Saito, Y., et al., *The inhibition of pancreatic cancer invasion-metastasis cascade in both cellular signal and blood coagulation cascade of tissue factor by its neutralization antibody*. Eur. J. Cancer, 2011. **47**: p. 2230-2239.
- [71] Stern, M. D., *Coagulation makes waves*. Biophys. J., 2012. **103**: p. 2049.
- [72] Stockie, J.M., *The mathematics of atmospheric dispersion modeling*. SIAM Rev., 2011. **53**: p. 349-372.
- [73] Suresh, S., *Biomechanics and biophysics of cancer cells*. Acta Materialia, 2007. **55**: p. 3989-4014.
- [74] Tormoen, G.W., et al., *The role of carrier number on the procoagulant activity of tissue factor in blood and plasma*. Phys. Biol., 2011. **8**: p. 066005.

- [75] Tosenberger, A., et al., *Modelling of thrombus growth in flow with a DPD-PDE method*. J. Theor. Biol., 2013. **337C**: p. 30-41.
- [76] Versteeg, H.H., et al., *Tissue factor and cancer metastasis: the role of intracellular and extracellular signaling pathways*. Mol. Med., 2004. **10**: p. 6-11.
- [77] Wajima, T., et al., *A comprehensive model for the humoral coagulation network in humans*. Nature, 2009. **86**(3): p. 290-298.
- [78] Wang, Y. and P. Dimitrakopoulos, *Nature of the hemodynamic forces exerted on vascular endothelial cells or leukocytes adhering to the surface of blood vessels*. Phys. Fluids, 2006. **18**: p. 087107.
- [79] Weinberg, R.A., **The Biology of Cancer**. New York: Garland Science, 2006.
- [80] Welsh, J., et al., *Tissue factor expression determines tumor cell coagulation kinetics*. Int. J. Lab. Hematol., 2012. **34**: p. 396-402.
- [81] Yamaguchi, T., et al., *Computational mechanical model studies on the spontaneous emergent morphogenesis of the cultured endothelial cells*. J. Biomech., 2000. **33**: p. 115-126.
- [82] Yanenko, N.N., **The Method of Fractional Steps**. Berlin: Springer-Verlag, 1971.
- [83] Yates, K. R., et al., *Pancreatic cancer cell and microparticle procoagulant surface characterization: involvement of membrane-expressed tissue factor, phosphatidylserine and phosphatidylethanolamine*. Blood Coagul. Fibrinolysis, 2011. **8**: p. 680-687.
- [84] Yu, A., et al., *Spatiotemporal dynamics of contact activation factors of blood coagulation*. Biochim. Biophys. Acta, 2002. **1569**: p. 86-104.
- [85] Zarnitsina, V. I., et al., *A mathematical model for the spatio-temporal dynamics of intrinsic pathway of blood coagulation. The model description*. Thromb. Res., 1996. **84**(4): p. 225-236.
- [86] Zarnitsina, V. I., et al., *A mathematical model for the spatio-temporal dynamics of intrinsic pathway of blood coagulation. Results*. Thromb. Res., 1996. **84**(5): p. 333-344.